Effects of disorder on electrical and optical properties of doped ZnO thin films grown by pulsed laser deposition

By

AMIT KUMAR DAS

PHYS03200904002

Raja Ramanna Centre for Advanced Technology, Indore

A thesis submitted to the

Board of Studies in Physical Sciences

In partial fulfillment of requirements

For the Degree of

DOCTOR OF PHILOSOPHY

of

HOMI BHABHA NATIONAL INSTITUTE

August, 2015

Homi Bhabha National Institute

Recommendations of the Viva Voce Board

As members of the Viva Voce Board, we certify that we have read the dissertation prepared by Amit Kumar Das entitled "Effects of disorder on electrical and optical properties of doped ZnO thin films grown by pulsed laser deposition" and recommend that it maybe accepted as fulfilling the dissertation requirement for the Degree of Doctor of Philosophy.

Chair - Date:

Guide/Convener - Date:

Member 1 - Date:

Member 2 - Date:

External Examiner - Date:

Final approval and acceptance of this dissertation is contingent upon the candidate's submission of the final copies of the dissertation to HBNI.

I hereby certify that I have read this dissertation prepared under my direction and recommend that it may be accepted as fulfilling the dissertation requirement.

Date:

Place: Guide

STATEMENT BY AUTHOR

This dissertation has been submitted in partial fulfillment of requirements for an advanced degree at Homi Bhabha National Institute (HBNI) and is deposited in the Library to be made available to borrowers under rules of the HBNI.

Brief quotations from this dissertation are allowable without special permission, provided that accurate acknowledgement of source is made. Requests for permission for extended quotation from or reproduction of this manuscript in whole or in part may be granted by the Competent Authority of HBNI when in his or her judgment the proposed use of the material is in the interests of scholarship. In all other instances, however, permission must be obtained from the author.

(Amit Kumar Das)

DECLARATION

I, hereby declare that the investigation presented in the thesis has been carried out by me. The work is original and has not been submitted earlier as a whole or in part for a degree / diploma at this or any other Institution / University.

(Amit Kumar Das)

List of Publications arising from the thesis

Journal

1. "Effect of Si doping on electrical and optical properties of ZnO thin films grown by sequential pulsed laser deposition", **Amit K Das**, P. Misra and L. M. Kukreja, *J. Phys. D: Appl. Phys.* **2009**, *42*, 165405.

2. "Quantum corrections to temperature dependent electrical conductivity of ZnO thin films degenerately doped with Si", **Amit K Das**, R. S. Ajimsha and L. M. Kukreja, *Appl. Phys. Lett.* **2014**, *104*, 042112.

3. "Effect of Mg diffusion on photoluminescence spectra of MgZnO/ZnO bilayers annealed at different temperatures", **Amit K Das**, P. Misra, R. S. Ajimsha, A. Bose, S. C. Joshi, S. Porwal, T. K. Sharma, S. M. Oak and L. M. Kukreja, *J. Appl. Phys.* **2013** *114*, 183103.

4. "Thickness dependent metal-insulator transition and dimensional crossover for weak localization in $Si_{0.02}Zn_{0.98}O$ thin films grown by pulsed laser deposition", **Amit K Das**, R. S. Ajimsha and L. M. Kukreja., *J. Appl. Phys.* **2014**, *115*, 193705.

5. "Effect of electron interference on temperature dependent transport properties of two dimensional electron gas at MgZnO/ZnO interfaces", **Amit K Das**, P. Misra, R. S. Ajimsha, M. P. Joshi and L. M. Kukreja, *Appl. Phys. Lett.* **2015**, *107*, 102104.

Conference

1. "Electrical and optical properties of $Mg_xZn_{1-x}O$/ZnO heterostructures", **Amit K Das**, R. S. Ajimsha and L. M. Kukreja, *DAE-BRNS 7th National Symposium on Pulsed Laser Deposition of Thin Films and Nanostructured Materials*, **November, 2013**, IIT Kharagpur.

(Amit Kumar Das)

ACKNOWLEDGEMENTS

Foremost, I express my sincere gratitude to my advisor Prof. L. M. Kukreja for his continuous support to my Ph.D study and related research, for his patience, motivation and enthusiasm. His guidance helped me in all the time of research and writing of this thesis.

Besides my advisor, I thank the rest of my Doctoral committee: Prof. P. K. Gupta, Prof. G. S. Lodha and Prof. D. K. Aswal, not only for their insightful comments and encouragement, but also for the hard questions which incented me to widen my research from various perspectives.

I sincerely thank Dr. Arup Banerjee for his support and encouragement. My sincere thanks also goes to Dr. Pankaj Misra for teaching me the methods of pulsed laser deposition and guiding me on many aspects of my Ph.D study. I thank Dr. R. Rawat, Shri S. Kumar, Shri A. Wadekar, Dr. D. M. Phase of DAE-CSR, Indore and Dr. Mukesh Joshi, Dr. S. Rajmohan, Shri R. Kumar, Dr. T. Ganguli, and Dr. T. Sharma of RRCAT, Indore for their help in different experiments.

I thank my fellow labmates, Dr. R. S. Ajimsha, Shri Vikas K. Sahu and Shri D. Saha for the stimulating discussions, for the long hours we were working together before deadlines, and for all the fun we have had together. Also, I thank Shri Arupratan Jana, Shri Krishnakanta Mondal, Shri Arijit Chakraborty and Shri Dipankar Jana for the numerous discussions we had over tea sessions.

Last but not the least, I would like to thank my family - my parents, wife and centenarian grandfather for supporting me throughout writing this thesis and my life in general.

Contents

Synopsis

ZnO is a well known semiconductor which has been used for a long time in paints, sunscreen lotions, tooth paste, phosphor, varistor etc. However in recent past it has drawn the attention of semiconductor research community because it is a wide bandgap semiconductor with a bandgap of $\approx$ 3.38 eV at room temperature. By nature of its wide bandgap, ZnO is transparent in the entire visible spectral region. As a consequence, it is a suitable candidate for transparent conducting electrode applications and also as an active ingredient for novel and futuristic transparent electronic devices. Moreover being a direct bandgap semiconductor with its bandgap falling in the UV spectral region, it is also an efficient UV emitter. The large excitonic binding energy of $\approx$60 meV ensures that excitons can be present in ZnO even at room temperature that further enhances the UV emission efficiency. The excitonic nature of the near band edge emission makes ZnO a very good material for UV laser device applications. It can also be used in solar blind photo-detectors. Further ZnO has a very rugged wurtzite crystalline structure with a high cohesive energy which renders it radiation hard and high temperature stable. Therefore the ZnO based devices can be used in space and nuclear reactors and in applications that demand high temperature and high power handling. ZnO films and nanostructures have been grown by a variety of methods such as sol-gel, sputtering, MBE, MOCVD, electron beam evaporation, pulsed laser deposition (PLD), atomic layer deposition (ALD) etc. Among these PLD is a very simple and versatile technique that offers multiple advantages for growth of ZnO thin films and nanostructures. This technique uses high power pulsed laser at optimized fluence for ablating the target material to produce a luminous plume that subsequently gets condensed on the suitable substrates placed in the path of the plume. No matter what growth method is used, the grown ZnO films will almost always have some degree of defects and disorders in it. These may be intrinsic point defects like zinc and oxygen interstitials and vacancies, unintentional impurities like H, Al, Ga etc. and structural disorders. Another important source of defects and disorder is the intentional doping of ZnO, required to tailor the electrical and optical properties. For example ZnO is doped with group III dopants such as Al, Ga, In, B, Si etc. to increase its electron concentration for applications in transparent conducting electrodes. Mg and Cd are introduced in ZnO for bandgap engineering. N, P, As, Sb, Li etc. are used as dopant for p-type conversion. The above mentioned defects and disorders in the doped/undoped ZnO films are randomly positioned throughout the film volume. The random potential fluctuations associated with disorder cause band tailing and bandgap narrowing. The free carriers released by the defects may bring about semiconductor to metal transition as well. The disorder in semiconductor lattice is also a source of carrier scattering that reduces their transport mean free path and mobility. If due to multiple scatterings from these randomly positioned defects the mean free path of the carriers becomes comparable to the Fermi wavelength, the carriers can no longer be considered as classical particles under effective mass approximations. In such cases quantum interference effects come into picture resulting in quantum corrections to the Boltzmann conductivity. Under these circumstances the low temperature transport properties of doped ZnO films get modified significantly. If the strength of disorder is very high, it may even cause strong localization of the carriers leading to metal to insulator transition and highly resistive ZnO films. Moreover the intentional or unintentional defects introduce trapping or luminescent levels in the ZnO bandgap resulting in defect related optical transitions which modify the photoluminescence and photoabsorption spectra. There exist numerous reports on the growth and characteristics of undoped and doped ZnO films. However systematic studies on the effects of disorder on the electrical and optical properties of doped ZnO thin films are needed for its practical applications. In the present thesis we have grown doped ZnO thin films using optimized pulsed laser deposition. Their structural, electrical and optical properties have been characterized by high resolution X-ray diffraction (HRXRD), atomic force microscopy (AFM), photoluminescence (PL) and photoabsoprtion (UV-Vis) spectroscopy, Hall, resistivity and magnetoresistance measurements, X-ray photo electron spectroscopy (XPES) and secondary ion mass spectrometry (SIMS) to understand the effects of defects and disorder on the electrical and optical properties of doped ZnO thin films.

Chapter I gives brief introduction on ZnO and its physical properties, different methodologies of depositing ZnO thin films and the effects of defects and disorder on the electrical and optical properties of semiconductor thin films. Following these, a brief review of the existing literature on the effects of disorder on ZnO thin films is presented. The motivation of the present thesis is also discussed in this chapter.

Chapter II describes the method of preparing ablation targets and the growth of ZnO thin films by PLD. The growth process including the ablation of target material and condensation of the ablated species on the substrate surface to form continuous thin film is discussed. A brief discussion about sequential PLD scheme which was used for deposition of doped ZnO films is also provided. In addition to these, basic principles of the characterization techniques such as HRXRD, SIMS, PL, UV-Vis, AFM, XPES, Hall, resistivity and magnetoresistance measurements are also presented. A brief discussion about error analysis is also given in this chapter.

In **chapter III** the effects of disorder on the room temperature electrical and optical properties of c-axis oriented Si doped ZnO (SZO) thin films of typical thickness $\approx$ 150 nm grown by sequential Pulsed Laser Deposition have been discussed. The concentration of Si was varied in the range from 0.5 to 6.5%. As a result of doping, the resistivity of the SZO thin films decreased to $\approx 6.2\times10^{-4}$ ohm-cm which is two orders of magnitude lower than that of the undoped ZnO films grown under same conditions. The electron density in the Si doped ZnO films was more than the Mott critical density (5×10^{19}cm^{-3}), signifying semiconductor to metal transition. The room temperature electron mobility decreased with increasing Si doping due to enhanced scattering from the statistically distributed impurities and defects. The band gap of the Si doped ZnO thin films was found to increase due to the collective effects of high carrier concentration induced Burstein-Moss blue shift and doping related disorder induced bandgap narrowing. UV photoluminescence (PL) was also observed at room temperature from these Si doped ZnO films. The intensity of PL spectra was found to decrease while their FWHM increased with increasing Si doping concentration due to the potential fluctuation caused by random distribution of the impurity ions.

The low temperature transport properties of Si doped ZnO thin films showed elegantly the effects of defects and disorder. These are discussed in detail in **chapter IV**. Multiple scattering of electrons from the defects and disorder brings about the quantum corrections to conductivity. To study these effects two sets of Si doped ZnO thin films were grown by sequential PLD on alumina substrates. In one set the film thickness was kept at 230 nm and Si doping concentration was varied in the range from ≈0.5 to 5.8 %. In the other set the Si concentration was kept at 2%, but the thickness was varied in the range from 15 to 40 nm. The electron concentrations in the films belonging to the first set were in the range from 1.7×10^{20} to 4.8×10^{20} cm^{-3} showing their degenerate nature. However, temperature dependent resistivity measurements in the range from 300 to 4.2 K revealed negative temperature coefficient of resistivity (TCR) for all the films at low temperature. The observed negative magnetoresistance and temperature independent nature of electron density in the films at low temperature pointed to disorder induced weak localization as the dominant contributor towards the negative TCR. In the second set of films (with fixed silicon concentration of ≈ 2%) while the film with thickness of ≈ 40 nm showed typical metallic behavior in the temperature dependent sheet resistance measurements, the film with thickness ≈15 nm showed a strongly localized behavior wherein the dominant mechanism of conduction at low temperature was variable range hopping (VRH). This implied a thickness driven metal to insulator transition in SZO films. On the other hand, the film with thickness of ≈ 20 nm showed a temperature dependent dimensional crossover from

3D to 2D weak localization with decreasing temperature. This was due to the decrease of the inelastic scattering length with increasing temperature.

Chapter V deals with effects of disorder on the electrical and optical properties of MgZnO/ZnO heterostructures which are important for different practical applications of ZnO. Diffusion of Mg across the interface in these heterostructures reduces the electron mean free path and increases the bandgap on the ZnO side of the heterointerface which significantly effects the electrical and optical properties of the MgZnO/ZnO heterostructures. To begin with, the thermal stability of the interface in MgZnO/ZnO heterostructures with a fixed Mg concentration of $\approx$30% was studied by annealing the heterostructures at temperatures ranging from 600 to 900^0C to optimize the growth conditions for sharp interface. It was found that the bilayers were quite stable upto the temperature of $\approx 700^0$C. Beyond that diffusion of Mg across the interface severely deteriorated the interface quality and modified the PL spectra from the heterostructures. The experimental PL spectra matched quite well with the theoretically calculated PL spectra which was simulated from the measured SIMS data. To study the electron transport in MgZnO/ZnO heterostructures, a set of bilayers with Mg concentration varying in the range of 16 to 40% were grown at temperature of $\approx 400^0$C. The thickness of ZnO layer was $\approx$ 80 nm and that of the MgZnO was $\approx$50 nm. It was found that on increasing Mg concentration in MgZnO layer of the heterostructures, the sheet electron concentration monotonically increased and the sheet resistance decreased. In addition the electron concentration and mobility in the heterostructures were almost temperature independent in the temperature range from 300 to 4.2 K, indicating the formation of 2-dimensional electron gas (2DEG) at the heterointerface. The 2DEG can form as a result of accumulation of a large quantity of electrons at the MgZnO/ZnO interface due to macroscopic polarization mismatch between MgZnO and ZnO layers. The temperature dependent resistivity measurements of the heterostructures showed a negative temperature coefficient of resistivity at low temperatures together with negative low field magnetoresistance which were attributed to disorder induced electron interference effects.

The thesis is finally concluded in **chapter VI**. In this chapter brief summary of the effects of defects and disorder on the electrical and optical properties of doped ZnO thin films and heterostructures as understood from our studies are discussed. It was found that disorder in doped ZnO thin films and heterostructures causes bandgap narrowing, semiconductor to metal transition and quantum corrections to conductivity. The degenerately doped ZnO thin films can even undergo metal to insulator transition if the degree of disorder is increased. Moreover it emerged from the present research work that Si can be used as an effective dopant in ZnO for cost effective transparent conducting electrode applications. Scope of future work in the field is also presented briefly in this chapter.

List of Figures

List of Tables

Chapter 1

Introduction and overview

ZnO as a semiconductor has some unique properties that make it suitable for various applications [1]. It has an wide bandgap of about 3.3 eV at room temperature which makes it transparent in the visible spectral region. The excitonic binding energy in ZnO is 60 meV implying that excitons can be stable even at room temperature. ZnO has a rugged wurtzite structure with high cohesive energy that enables it to be used in environments with high temperature and radiation hazards [2]. It is non-toxic and environment friendly. Moreover it is pyroelectric, piezoelectric, piezooptic, phosphorescent and a good thermal conductor [1]. It can be doped easily with n-type dopants such as Al, B, In, Ga and Si [2–6]. It can also be alloyed with Mg and Cd for the purpose of bandgap engineering [7, 8]. The growth of ZnO in single crystal as well as thin films and nanostructures are quite well established [1, 2]. Doping with other elements such as transition and rare-earth elements for tailoring the electrical and optical properties of ZnO can also be carried out using a variety of methodologies quite easily [9, 10].

ZnO has been used for different purposes since prehistoric times. In ancient India Zinc Oxide was used in medicine and is mentioned in Charaka Samhita [11]. It was also used by ancient Greek physicians for treating a variety of skin diseases. In recent times ZnO is used in various industries such as rubber, pigment, ceramic industries. It is also used in pharmaceutical industry as a sunscreen, calamine lotion etc. However its unique electrical and optical properties soon caught the attentions of material science and semiconductor research communities. Because of wide bandgap and high exciton binding energy, ZnO is an efficient UV emitter at room temperature and hence a suitable candidate for LED applications [1]. It has also been used as solar blind UV detector [12]. It is considered suitable material for electrically pumped random laser and polaritonic laser applications as well [13, 14]. Al, B, Ga and Si doped ZnO thin films are found to be highly conducting as well as transparent in the visible region. Therefore they can be a low cost alternative to ITO as transparent conducting electrodes [4–6, 15]. Researchers have also shown the utility of ZnO as piezoelectric, gas and bio-sensing applications [16, 17]. Radiation resistance property of ZnO due to its high cohesive energy makes it suitable for space and nuclear reactor applications [2].

ZnO films and nanostructures have been grown by a variety of methods such as sol-gel, RF-sputtering, MBE, MOVPE, electron beam evaporation, pulsed laser deposition (PLD), atomic layer deposition (ALD) etc [17–24]. Irrespective of the growth method, the grown ZnO films almost always have some degree of defects and disorders in it. These may be intrinsic or extrinsic defects and disorders [4–6, 25–28]. These defects and disorders in the doped/undoped ZnO films, be it intrinsic, extrinsic or structural, are randomly positioned. The random potential fluctuations associated with disorder causes band tailing and bandgap narrowing [29, 30]. The free carriers released by the defects may bring about semiconductor to metal transition as well [31, 32]. The disorder in semiconductor lattice is also a source of carrier scatterings that reduce their transport mean free path and mobility [32]. If due to multiple scatterings from these randomly positioned defects the mean free path of the carriers becomes comparable to the Fermi wavelength, the carriers can no longer be considered as classical particles under effective mass approximations. In such cases quantum interference effect is important and we have to treat the wave nature of the charge carriers. This results in weak localization of the carriers and quantum corrections to the Boltzmann conductivity [32–34]. If the strength of disorder is very high, it may even cause strong localization of the carriers leading to metal to insulator transition [32] [35, p. 225]. Moreover the intentional or unintentional defects introduce trapping or luminescent levels in the ZnO bandgap resulting in defect related optical transitions which modify the photoluminescence and photoabsorption spectra [36].

In the first section of this chapter we give an overview of the structural, electrical and optical properties of ZnO briefly. We then proceed to provide a brief review of the different phenomena brought about by defects and disorder in semiconductors thin films in the second section of this chapter. In the third section we give an overview of the different methods that has been used to grow epitaxial ZnO thin films. Brief literature review on the effects of disorder in ZnO thin films is provided in the fourth section and in the fifth section we discuss the motivation of the present thesis.

1.1 Properties of ZnO as a semiconductor

As already mentioned ZnO is an wide bandgap semiconductor with bandgap of ≈ 3.3 eV at room temperature. It has a rugged crystal structure with cohesive energy of ≈ 1.89 eV. As a result it is a radiation hard semiconductor. It's melting and boiling points are ≈ 1785 and 1980^0C, enabling it to withstand without degradation the high temperature required for alloying and various device formation [1,2]. We discuss some of the physical properties of ZnO from the perspective of semiconductor applications in following subsections.

1.1.1 Crystal structure

The crystal structure of ZnO at normal temperature and pressure is hexagonal wurtzite. It consists of two interpenetrating hexagonal sub-lattices of Zn and oxygen atoms displaced with respect to each other along the c axis by $u \approx (3/8)$ of the c-axis length. In this structure each oxygen atoms are tetrahedrally surrounded by four Zn atoms and vice versa, which is typical of the sp^3 covalent bonding [2]. However because of the difference in electronegativity of the constituent atoms the bonds have also a partially ionic character which is about 0.616 in Philips ionicity scale. ZnO wurtzite unit cell is shown in the figure 1.1.

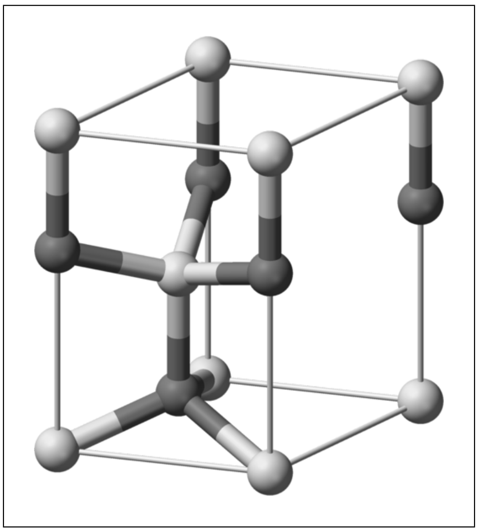

Figure 1.1: ZnO wurtzite unit cell. Light and Dark structures respectively represent oxygen and zinc atoms.

The lattice parameters of ZnO wurtzite lattice, namely c and a, are related by $\frac{c}{a} = \sqrt{8/3} = 1.633$. The reported values of these lattice parameters as found in the literatures ranges from 3.2475 to 3.2501 Å for the a parameter and from 5.2042 to 5.2075 Å for the c parameter. Correspondingly the u parameter and c/a ratio deviates from the ideal for wurtzite ZnO and has been found to be in the range from ≈ 0.3817 to 0.3856 and ≈ 1.593 to 1.603 respectively. This variation is thought to be caused by ionicity and presence of points and extended defects [1,2].

Due to the absence of inversion symmetry, ZnO crystals exhibit crystallographic polarity. The closed pack (0001) basal planes differ from $(000\bar{1})$ planes. Therefore there will be a net dipole moment and spontaneous polarization along the c-axis in wurtzite ZnO. According to the convention, (0001) axis pointing from the face of the O plane to the Zn plane is taken as the positive z direction. Therefore when the bonds along the c direction are from Zn to O, the polarity is referred to as Zn polarity. Similarly, when the bonds along the c direction are from O to Zn, the polarity is called O polarity [2]. Many properties of ZnO depend on its polarity, for example, growth and etching rate, defect generation and plasticity, luminescence efficiency, spontaneous polarization and piezoelectricity. In wurtzite ZnO, other than the primary polar plane (0001) and the corresponding direction, which are the most commonly used surface and direction for growth, many other secondary planes and directions exist. For example two other common surfaces are (1120) and (1010) faces of ZnO, both of which contain an equal number of O and Zn atoms and hence non-polar [1].

A variety of substrates has been used for the growth of ZnO thin films and the structural, electrical and optical properties of ZnO thin films depends significantly on the substrates used [1]. The most commonly used substrate is (0001) alumina substrates. The epitaxial relationship between alumina substrates and the grown ZnO films generally depends on the growth temperature. The two most common epitaxial relationships are ZnO (0001) || Al_2O_3 (0001) and ZnO (10$\bar{1}$0) || Al_2O_3 (10$\bar{1}$0) or ZnO (0001) || Al_2O_3 (0001) and ZnO (10$\bar{1}$0) || Al_2O_3 (11$\bar{2}$0) [37]. The former happens at lower temperature and the lattice mismatch in that case is about 32% while the later occurs at higher growth temperature with an in-plane lattice mismatch of about 18% due to 30^0 in-plane rotated growth of ZnO on sapphire. In the former case growth happens on the Al sub-lattice of the sapphire while in the later case it happens on the O sub-lattice. Moreover in the later case due to domain epitaxy the overall lattice mismatch is reduced to $\approx 0.9\%$, facilitating epitaxy [38]. Although the growth of ZnO on alumina generally proceeds along the c-axis due to its polarity, resulting in preferentially c-axis oriented films, the films usually contains a large number of grains packed together in mosaic structure and separated by grain boundaries [2]. The lattice parameters of ZnO films grown on sapphire deviates from the ideal value due to lattice mismatch induced strain and various kinds of points and structural defects arising due to high lattice mismatch. However there are some reports in the literature of growth of high quality ZnO films growth on sapphire using a specially prepared buffer layers [39]. Moreover the crystalline quality of ZnO thin film could be improved manifold by using lattice matched substrates like $ScAlMgO_4$ (SCAM) which resulted in almost single crystal ZnO thin films [40].

ZnO also crystallizes in rock salt and zinc blend structures at under different conditions. The rock salt phase only materializes at high pressure and zinc blend phase could be grown only on cubic substrates [2].

1.1.2 Optical properties

The optical property of ZnO is related to both intrinsic and extrinsic effects. Intrinsic optical transitions take place between electrons in the conduction band and holes in the valence band, including Coulomb interaction mediated excitonic effects. ZnO is a direct bandgap semiconductor with both the conduction band minima and valence band maxima at the Γ point in the Brillouin zone [1]. Its conduction band is primarily made of empty $4s$ states of Zn^{2+} ions and the valence band is primarily composed of filled $2p$ sates of O^{2-}. The valence band splits into three bands due to spin-orbit and crystal field splitting. The near band edge emissions or absorptions in ZnO are due to transitions involving one of these bands. Accordingly the corresponding excitonic transitions involving these bands are referred as A, B and C (crystal field spitted band) as shown in figure 1.2. The A-B splitting is $\approx$ 6 meV and B-C is $\approx$ 38 meV [2]. The electron effective mass (m_e^*) in the conduction band is $\approx 0.28m_0$ and is almost isotropic. The hole effective masses (m_h^*) in the A and B valence bands are also isotropic having the value of $\approx 0.59m_0$ [40]. On the contrary the hole effective masses on the C band are about $0.31m_0$ for parallel to c axis and $0.55m_0$ for direction perpendicular to c axis [2].

Electrons and holes generated in ZnO by the absorption of a photon of suitable energy can form a hydrogen like bound state due to the attractive Coulomb interaction. It is known as free exciton [29]. Free excitons are generally seen in pure and doped ZnO with low impurity concentration. The energy of an exciton is calculated with respect to the conduction band and is given by,

$$E_{ex} = -\frac{\mu^* e^4}{2\hbar^2 \epsilon^2 n^2} = -\frac{E_B}{n^2} \tag{1.1}$$

Here n is the usual principle quantum number denoting the energy levels of the exciton and E_B is called the excitonic binding energy, *i.e.* the energy required to break an exciton in the $n = 1$ state into a free electron-hole pair. e is the dielectric permittivity of ZnO and μ^* is the effective reduced mass given by,

$$\frac{1}{\mu^*} = \frac{1}{m_e^*} + \frac{1}{m_h^*} \tag{1.2}$$

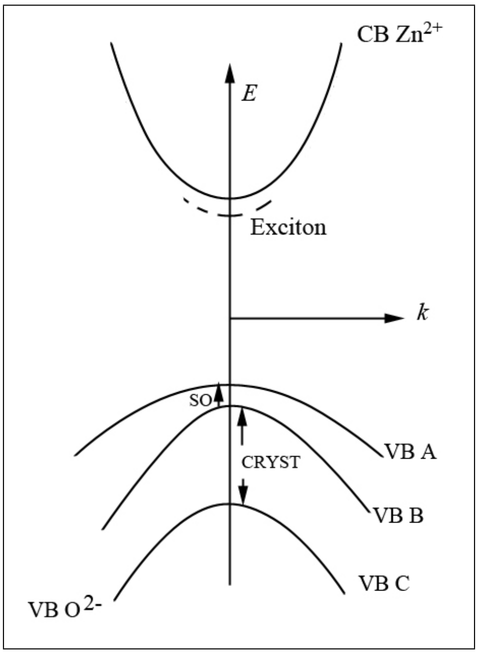

Figure 1.2: Schematic E-k diagram of ZnO.

A schematic representation of the excitonic level is also shown in figure 1.2. Due to negative energy of the excitons with respect to the conduction band, the excitonic features in the optical absorption and emission spectra are seen (in the form of narrow peaks) at energies slightly less than the bandgap energy (Eg), given by [29]

$$h\nu = E_g - E_{ex} \tag{1.3}$$

In ZnO the excitonic binding energy is about 60 meV [1], implying that the excitonic peaks corresponding to the $n = 1$ exciton will appear for photon energies 60 meV lower than the bandgap. Moreover, from this binding energy value it is also evident that excitons can exist in ZnO at temperatures far higher than the room temperature. As the excitons can only be formed at or near the $\Gamma(k = 0)$ point, their transition linewidth is very narrow which broadens only slightly with increasing temperature [35, p. 241]. Owing to their delta function like density of states and narrow emission linewidth, excitons are of particular importance for laser diode applications [29]. As a result ZnO is considered a suitable material for UV laser diode applications [41]. In very pure ZnO and at low temperature excitonic features corresponding to $n > 1$ levels could be seen in the optical absorption or emission spectra [41]. However the intensity of the higher order peaks sharply decreases with increasing n.

Due to partly ionic bonding in ZnO the vibration of the cations and anions against each other give rise to long range polarization field which can be considered as a superposition of LO phonons [35]. The scattering of excitons with these LO phonons can give rise to LO phonon mediated excitonic recombination (emitting one or more LO phonon) whose peak positions are given by [29],

$$h\nu = E_g - E_{ex} - n\hbar\omega_{LO} \tag{1.4}$$

Here $\hbar\omega_{LO}$ is the LO phonon energy and n is the numbers of LO phonons emitted. Therefore depending on n a number of replicas of excitonic recombination can be seen in the emission spectra of ZnO [2].

The excitons can bound themselves to various defects and impurities to give rise to bound excitons [41]. Most of the times these defects are neutral or ionized donors and acceptors and the corresponding excitons are called donor or acceptor bound excitons. Because of the additional binding energy of the bound excitons, their transition peak is found to be slightly red shifted with respect to the free excitons [2]. Moreover these bound excitons are generally seen only at low temperature due to their low binding energy. At higher temperature they decay to free exciton states. Since the bound excitons are localized to their binding centers, their kinetic energy spread is very small and hence bound excitons peaks are found to be narrower as compared to their free exciton counterparts. LO phonon replicas of these bound exciton peaks can also be seen in the photoluminescence spectra of ZnO at low temperature [2]. Binding energies of the bound excitons to the donor or acceptor species depend on the nature of the binding centers and typically vary in the range from about 3 to 27 meV [41]. The excitons bound to neutral donor bound excitons can sometimes recombine leaving the donor in an excited state, thereby leading to transition energy slightly less than normal donor bound exciton transition energy. This is called a two electron satellite line (TES) [2].

Another feature that is seen in the emission spectrum of ZnO is the donor-acceptor pair transitions (DAP). This involves transition between a shallow donor and acceptor species. DAP transition generally show blue shift with increasing temperature, as with increasing temperature the transition may involve conduction or valence band [29]. Apart from these near band edge transitions (NBE), other intrinsic or extrinsic defect related transitions in the visible spectral region are also observed in ZnO. For example the famous green emission from ZnO is known to be caused by defects like Zn vacancy, O vacancy, Cu impurities etc. The orange luminescence is contributed to the presence of additional oxygen in the ZnO lattice [25, 42–47].

The optical properties are gauzed by either temperature dependent photoabsorption or photoluminescence measurements. Using these techniques different exciton complexes in ZnO and their binding energies have been calculated [41]. For ZnO films grown on alumina, strain induced due to large lattice parameter mismatch prevented the observation of well resolved peaks corresponding to the ground state and excited states of A, B and C excitons. Using lattice matched substrates to grow ZnO thin films, transition corresponding to all these excitons could be resolved [2]. Moreover strain also shifts the excitonic resonance energy. Temperature dependent PL measurements revealed that the temperature dependence of different excitonic transition energies was in agreement with the well known laws of variation of semiconductors bandgap with temperature [48]. Stimulated emission and lasing actions have also been observed in ZnO thin films and bulk. Electrically pumped random laser have also been realized in ZnO [14].

1.1.3 Electrical properties

The bulk electrical property of ZnO is often decided by the defects present in it. It is mostly found to be n-type conducting due to presence of native donor type defects such as oxygen vacancy and zinc interstitials and zinc antisites [1]. The presence of extraneous impurities like H, Al, Ga etc may also be responsible for the n-type conductivity of ZnO [27]. The electrical properties of ZnO are measured by temperature dependent Hall coefficient (R_H) and resistivity (ρ) measurements. From these data the carrier density (n) and Hall mobility (μ_H) can be deduced using the formula $R_H = r_H/ne$ and $\mu_H = R_H/\rho$, where r_H is the scattering mechanism dependent Hall scattering factor and e is the electronic charge. The drift mobility (μ) is calculated from the Hall mobility using the fact that $\mu_H = r_H\mu$. Mobility depends on the scattering mechanism of the charge carrier and the parameter that decides the mobility for a given semiconductor is scattering time τ and it is related to the mobility by,

$$\mu = \frac{e\tau}{m^*} \tag{1.5}$$

In a semiconductor at the same time multiple scattering mechanisms are usually active and the effective scattering time combining all the dominant scattering mechanism is given by

Matthiessen's rule,

$$\frac{1}{\tau} = \sum_i \frac{1}{\tau_i} \tag{1.6}$$

where τ_i is the mean scattering time for i'th scattering mechanism.

The different dominant scattering mechanisms active in bulk ZnO are as follows [2].

(i) Ionized impurity scattering due to deflection of free carriers by the long range electric field of the ionized defects.

(ii) Being a polar semiconductor a long range polarization field is created in ZnO due to vibration of cations against anions. The charge carries may get scattered from this polarization field causing what is known as polar LO-phonon scattering.

(iii) Acoustic phonon scattering via deformation potential created due to the strain associated with acoustic phonons.

(iv) ZnO being a non-centrosymmetric material, the strain caused by phonons can generate a piezoelectric field which can scatter the charge carriers. This is known as piezoelectric scattering.

(v) If the dislocation density is high, then they can also significantly scatter the electrons. Basically acceptors centers are produced along the dislocation line which traps the electrons, creating a space charge region around them. The charge carriers get scattered from this space charge.

Using Monte-Carlo simulation and considering the above mentioned scattering mechanisms, Albrecht *et al.* predicted the room temperature electron mobility to be $\approx$ 300 cm^2/V-s in ZnO [49]. The highest room temperature electron mobility for ZnO single crystal grown by vapor phase transport method was reported to be about 205 cm^2/V-s with an electron concentration of $\approx 6 \times 10^{16}$ cm^{-3} by Look *et al* [50]. They also studied the temperature dependence of mobility of bulk ZnO and argued that below 8 K, the mechanism of conduction was hopping, whereas for temperatures higher than 40 K, band conduction dominated. In the intermediate temperature range mixed band and hopping conduction was active. The band conduction was via the scattering mechanism mentioned earlier.

On the contrary the electron mobility in ZnO thin films grown on alumina substrates are rather poor (< 100 cm^2/V-s) compared to that of the bulk ZnO [2]. The background electron density is such films are also quite high, ranging from 10^{16} to 10^{19} cm^{-3}. The poor electron mobility in ZnO thin films grown on alumina is primarily thought to be due to scattering from grain boundaries arising because of the mosaic structure of ZnO thin films grown on alumina substrates. The grain boundaries acts as trapping centers for electrons, thereby producing a space charge region and potential barrier for electron transport. In spite of these there has been some success in growing ZnO thin films with quite high electron mobility. Kaidashev *et al.* reported room temperature electron mobilities in the range from ≈ 115 to 155 cm^2/V-s with electron densities of about 10^{16} cm^{-3}, for undoped ZnO thin films grown on alumina [39]. They used a multistep PLD process. An electron mobility of ≈ 130 cm^2/V-s with electron concentration of $\approx 1.2 \times 10^{17}$ cm^{-3} was reported by Kato et al for their MBE grown ZnO thin films on sapphire substrates [51]. Iwata et al. using a ZnO/MgO double buffer layer could obtain an electron mobility of about 145 cm^2/V-s for ZnO films on sapphire substrates [52]. Using lattice matched substrate $ScAlMg0_4$, Tsukazaki *et al.* have shown impressive room temperature electron mobility of about 440 cm^2/V-s in ZnO/MgZnO heterostructure [53]. It was attributed to the formation of 2DEG at the interface. Subhnikov-de Haas oscillation and quantum Hall effect was also reported in such structures.

Using various dopants like Al, Ga, B, In, Si etc from group III and IV, the electron density and conductivity of ZnO thin films can be enhanced [3–6]. Such films being transparent in the visible spectral region can be utilized as transparent conducting electrodes. These dopants can enhance the electron density in ZnO films to ≈ 10^{21} cm^{-3} and bring down the resistivity to a value as low as 8.1×10^{-5} ohm-cm [54]. In such transparent conducting oxide (TCO) films the dominant scattering mechanism are ionized impurity scattering and grain boundary scattering. Although n-type doping in ZnO is easy to achieve, stable p-type doping is very difficult yet. There are numerous reports of p-type conversion using group-I dopants like Li, Na, K, Ag substituting for Zn and group - V dopants like N, P, As substituting for O. However stability of the p-type ZnO is an issue as with time the electrical properties of these doped ZnO films deteriorates [2]. Large background electron concentration is also an hindrance in obtaining stable p-type conversion. Difficulty in achieving stable p-type conversion is major problem for commercial application of ZnO based electronic and optoelectronic devices.

Impurities act as scattering centers for electrons. As a result the electron mean free path for elastic scattering decreases [33]. If the impurity concentration is so high that the electron mean free path is lower than or comparable to the Fermi wavelength, quantum effects will be prominent which significantly changes the transport properties of ZnO thin films. These phenomena are known as the quantum correction to conductivity, which will be discussed in detail in the next section.

1.2 Effects of defects and disorder on properties of semiconductors

Defects and disorder are always produced in semiconductor bulk or thin films during growth or other processing methods. For example randomly placed dopants or alloy atoms disturbs the periodicity of the lattice, thereby producing disorder. The same thing happens in case of intrinsic defects like vacancies and interstitials. Other sources of disorder are structural defects, interface and surface roughness etc. [35, p. 225]. These have profound effects on the optical and electrical properties of semiconductor. Some of these effects, which are important for ZnO thin films are discussed below.

1.2.1 Band tailing and bandgap narrowing

Band tailing and bandgap narrowing is quite common in semiconductors at high impurity concentrations. Ionized impurities interact with the electrons in conduction band and holes in valence band via Coulomb interaction. For example an ionized donor will provide an attractive potential for the conduction band electron and repulsive potential for the valence band holes. This interaction will locally lower the energy of the electrons and enhance the energy of the holes. The reverse will happen for the ionized acceptors. Since the impurities are distributed at random in the host lattice, the local fluctuation in energy positions of the conduction and valence bands will also be random in position as well as magnitude. Although the bandgap *i.e.* the energy separation between the bottom of the conduction band and the top of the valence band of the semiconductor is maintained constant locally as shown in figure 1.3a, but the density of states distribution with energy that integrates all the states at each energy for the whole volume of the semiconductor will have conduction band states at relatively low energy and valence band states at relatively high energy as shown in figure 1.3b. This gives rise to the phenomenon of band tailing as can be seen in figure 1.3b. These tail states also reduce the effective bandgap giving rise to bandgap narrowing [29, 30].

Another phenomenon associated with impurities that can give rise to band tailing and bandgap narrowing is random deformation potential. Since the impurities have different size than the lattice atoms, they give rise to randomly varying local tensile or compressional strain and associated deformation potential. Impurities at interstitial sites induce deformation potential corresponding to compression and likewise lattice vacancies induce deformation potential corresponding to tensile strain. The deformation potential perturbs the positions of conduction and valence band throughout the lattice. Dislocation can also contribute to band tailing via deformation potential [29].

Apart form these effects, another phenomenon that occurs at high impurity concentration is impurity band formation. As the concentration of impurities is increased the impurity

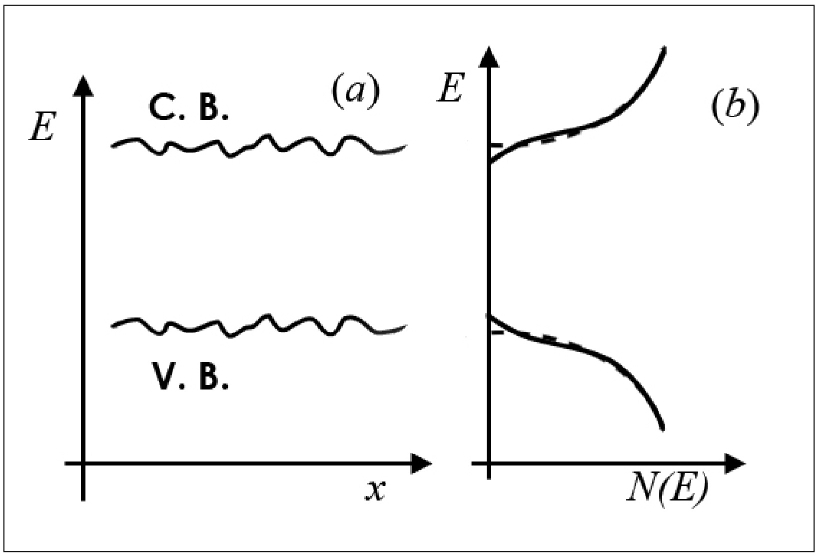

Figure 1.3: (a) Perturbation of band edges due to Coulomb interaction of randomly distributed impurities and (b) associated band tailing. Dashed curves in (b) show unperturbed density of states.

levels broaden and merge together to form a band near the conduction and valence band edges making tail states. If the impurity concentration becomes larger than the Mott critical density, the impurity band can merge with the conduction band, thereby effectively lowering the bandgap of the semiconductor [29, 31, 32]. Moreover, the local fluctuations in the bandgap due to carrier - impurity interaction or via deformation potential would change the energy positions of the impurity levels with respect to the band extrema. This would result in tailing of the impurity bands as well which contributes to formation of an impurity band [29]. The electron-electron or hole-hole exchange interaction is also capable of reducing the bandgap due to their energy lowering effects [30]. The bandgap narrowing and band tailing has been reported in some heavily doped ZnO films [55].

1.2.2 Semiconductor to metal transition

At high donor or acceptor concentration, the free carriers screen the Coulomb potential of the donor or acceptor ions. The screening radius (r_s) is given by [32]

$$r_s = \left(\frac{4m^* e^2 n^{1/3}}{\epsilon \hbar^2}\right)^{-1/2} = \frac{1}{2}\left(a_B n^{-1/3}\right)^{1/2} \tag{1.7}$$

In this equation m^* is the effective mass of the carrier, n is the carrier concentration, ϵ is dielectric permittivity and a_B is the Bohr radius of the ions. If the Bohr radius is less than the screening radius then the carriers are attached to their respective donor or acceptor atoms and the material acts as semiconductor or insulator. However if it so happens that for certain impurity concentration, the screening length is less than the Bohr radius, the state of the insulator becomes unstable. If the electrons (holes) leave their respective donor (acceptor) atoms, they won't be able to return as they would not be able to find their respective donor atoms due to strong screening. The material in such condition would function as a metal and the impurity concentration required for this to happen can be readily obtained form equation 1.7 assuming $r_s = a_B$. This critical doping concentration is known as the Mott critical concentration for semiconductor to metal transition and is given by [31, 32],

$$n_c = \left(\frac{0.25}{a_B}\right)^3 \tag{1.8}$$

For ZnO the value of Mott critical concentration is $\approx 5 \times 10^{19}$ cm^{-3}. However, the experimental value may vary within one order of magnitudes of this value [56]. This kind of semiconductor to metal transition is known as Mott transition and can be seen in ZnO films doped with donor type impurity like Al, Ga, B, Si etc. [4, 7, 56].

1.2.3 Quantum corrections to conductivity and weak localization

Doped semiconductors with donor (acceptors) concentration exceeding Mott critical concentration are called degenerate semiconductors since in such cases the Fermi level would be deep inside the conduction (valence) band. In respect of electrical properties, the degenerate semiconductors essentially behave like metals and the transport mechanism active in them is band transport [2]. So as per the Drude's model, their conductivity should be of the form

$$\sigma = \frac{ne^2\tau}{m^*} \tag{1.9}$$

Here n is the carrier density, m^* is the conductivity effective mass and τ is the average scattering time. The randomly positioned impurities and other defects act as disorder in semiconductor and scatters the carriers at random. If the impurity and defect density in the semiconductor is high, the value of τ and as a consequence, the mean free path (l) decreases. In the event that the mean free path is comparable to or less in magnitude than the Fermi wavelength (λ_F), the charge carriers can no longer be treated as classical particles as per Drude's model [32,57]. Their wave nature and the corresponding interference phenomenon have to be taken into account while calculating the conductivity. This quantum interference phenomenon puts additional terms in the expression for conductivity which are known as the quantum corrections to conductivity. The effects of quantum corrections are negligible in the case that $k_F l >> 1$, where k_F is the Fermi momentum. Quantum corrections are most significant when $k_F l \leq 1$, which is known as the Ioffe-Regel criterion [57].

In disordered semiconductors because of multiple scattering from the randomly positioned scattering centers like impurities, the electrons diffuse through the lattice under the action of applied electric field. Suppose in the semiconductor one electron reaches from the point $\mathbf{r}$ to point $\mathbf{r}'$ in time t. Figure 1.4a shows two possible trajectories for the electron to traverse from $\mathbf{r}$ to $\mathbf{r}'$ via multiple elastic scattering (*i.e.* the scattering themselves do not alter the phase of the electron waves).

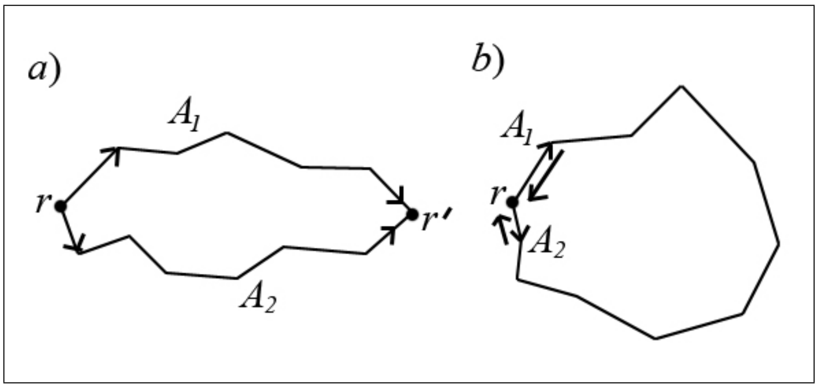

Figure 1.4: (a) Two possible electron trajectory due to multiple elastic scatterings and (b) closed loop trajectory.

If the probability amplitudes of reaching via the two alternative paths are A_1 and A_2 respectively, then the total probability of reaching from the point **r** to **r′** would be [31],

$$P(r, r', t) = |A_1|^2 + |A_2|^2 + 2|A_1||A_2| \cos\theta \tag{1.10}$$

where θ is the phase difference between the electron wave reaching point **r′** via the two alternate paths. Since the electrons suffer collision at random, the phase difference θ between any pair of paths will also be random. So if all possible pairs of such paths are considered, then on average the electron waves will be as likely to interfere constructively as to destructively. Therefore the interference term of equation 1.10 will be washed out and total probability will be simply the classical probability given by (considering there are i pairs of paths) [32],

$$P(r, r', t) = \sum_i \left(|A_1^i|^2 + |A_2^i|^2\right) \tag{1.11}$$

On the other hand if the initial and final points of carrier's paths are same *i.e.* it traverse a closed loop path as shown in figure 1.4b. In this case due to time reversal symmetry the two alternate closed paths - one clockwise and one anticlockwise - will have the same probability and they would have the same phase at the origin of the carrier. So the total probability for this to happen is [32]

$$P(r,r,t) = |A_1|^2 + |A_2|^2 + 2|A_1||A_2| = (|A_1| + |A_2|)^2 \tag{1.12}$$

For i pairs of closed path, the total probability,

$$P(r,r,t) = \sum_i \left(|A_1^i| + |A_2^i|\right)^2 \tag{1.13}$$

Therefore the charge carriers will have an enhanced probability of coming back to the origin forming closed loop paths. This is known as coherent back scattering [31,32]. The higher probability of finding the carrier at its origin implies that it will spend more time at the origin. This essentially means that the carrier is weakly localized at its origin and the phenomenon is given the name weak localization. Because of weak localization a correction term ($\Delta\sigma$) appears in the expression for conductivity.

So far we have only considered the elastic scatterings. However at a finite temperature there will always be inelastic collisions like carrier-carrier or carrier-phonon scatterings as well, which will change the phases of the electrons randomly (or in other words, destroy the phase coherence in closed loops). Therefore in presence of these inelastic dephasing collisions, the back-scattering probability will be reduced and hence the correction to conductivity due to weak localization will also decrease. Considering these inelastic scattering mechanisms, the corrections due to weak localization in 3D semiconductor is given by [31,32],

$$\sigma = \sigma_0 - \frac{e^2}{\hbar\pi^3}\left(\frac{1}{l} - \frac{1}{L_{in}}\right) \tag{1.14}$$

where σ_0 is the Drude conductivity and L_{in} is the phase breaking length or simply the inelastic scattering length. In general the inelastic scattering length increases with decreasing temperature ($L_{in} \propto T^{-p/2}$, p depends on the scattering mechanism and system dimensionality) and hence the conductivity at low temperature also increases according to formula 1.14. This gives rise to the well known negative temperature coefficient of resistivity in degenerate semiconductors (and metals) at low temperature [7,32]. In 2D system the corrections due to weak localization varies linearly with logarithm of temperature as given by,

$$\sigma = \sigma_0 + p\frac{e^2}{\pi h}\ln(T/T'_0) \tag{1.15}$$

Another important phenomenon that can also give rise to quantum correction is inter-electron interference in n-type semiconductors. In presence of random scattering or diffusion the probability of two electrons that were close to each other at $t = 0$ to meet again in same phase increases. As a result the density of states in the vicinity of Fermi level depends on temperature bringing about the following correction in conductivity (in 3D) [31],

$$\Delta\sigma \approx \left(\frac{e^2}{\hbar}\right)\frac{1}{L_{ee}} - \text{const} \tag{1.16}$$

L_{ee} is the phase correlation time for the conduction electrons having energy spread equivalent to kT, T being the temperature.

In presence of a magnetic field, the electrons acquire an extra phase in traversing a closed loop, the magnitude of which is proportional to the area of the loop. Since the area would be different for different closed loops, the additional phase acquired would also be random. Therefore the phase coherence at the origin will be broken in presence of a magnetic field and the weak localization phenomenon will be suppressed. Therefore semiconductors having weak localization as the dominant contributor to quantum corrections are expected to show negative magnetoresistance [32, 58]. On the contrary in the cases where inter-electron interference is dominant, the resistance is rather insensitive to magnetic field. These facts can be used to distinguish between the two types of quantum corrections in low temperature transport properties of semiconductors [58]. The quantum corrections can be further analyzed by studying the variation of magnetoresistance as a function of applied magnetic field. The inelastic scattering length or the dephasing length can be estimated by fitting the magnetoresistance data with appropriate theoretical model.

1.2.4 Strong localization or Anderson localization

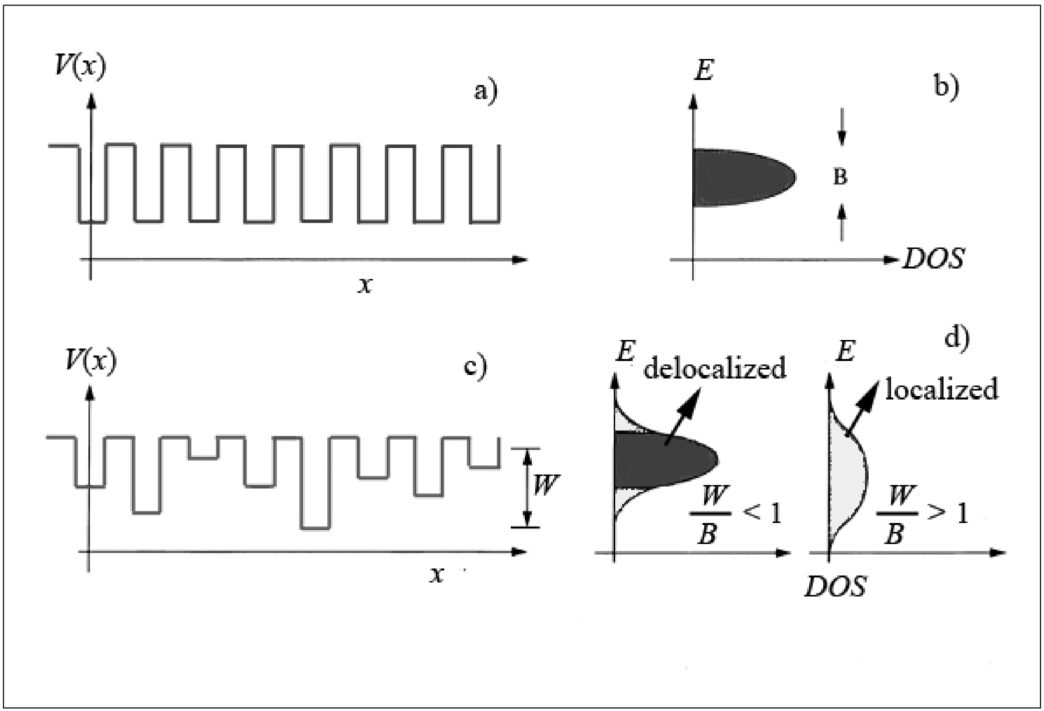

Figure 1.5: (a) Periodic potential and (b) corresponding density of states. (c) Disordered system and (d) corresponding density of states with localized and delocalized states [35, p. 226].

In a perfect periodic system, as shown in figure 1.5, because of the resonant overlap of wave functions from neighboring wells, the density of states consists of a band of Bloch states with certain width B. The edges of such bands are sharp. Disorder can be introduced in the system by excessive doping where either the identical dopant atoms are randomly placed (Lifshitz model) or by varying the potential depths of uniformly placed impurities (Anderson model) [35, p. 226]. In general both types of disorder are present in the system together. Figure 1.5c shows an Anderson type disorder where the potential depths of uniformly placed wells vary randomly within the energy range W. In such cases two things can happen - the sharp edges of the density of states get smeared into exponential tails and localized states appear at the band edges. If $W/B < 1$, the localized states remain at the band edges and band center is filled with extended states. However for $W/B > 1$, there are only localized states in the band [32]. The difference between Bloch states, extended states and localized states can be understood from their wave functions. For Bloch states, which is a superposition of atomic orbitals ϕ_n placed at every lattice points $\mathbf{R_i}$ with a proper long-range phase correlation, the wave function is [35, p. 226]

$$\begin{aligned}
\phi_k^{\mathrm{Bloch}}(\mathbf{r}) &= \textstyle\sum_i \exp(i\mathbf{k}.\mathbf{R_i})\phi_n(\mathbf{r}-\mathbf{R_i}) \\
&= \exp(i\mathbf{k}.\mathbf{r}) \textstyle\sum_i \exp[-i\mathbf{k}.(\mathbf{r}-\mathbf{R_i})]\phi_n(\mathbf{r}-\mathbf{R_i}) \\
&= \exp(i\mathbf{k}.\mathbf{r})u_{\mathbf{k}}(\mathbf{r})
\end{aligned} \tag{1.17}$$

where $u_{\mathbf{k}}(\mathbf{r})$ is a function having the periodicity of the lattice. In case of an extended state in a disordered system the long range phase correlation is missing. Therefore the wave function for extended state is [32, 35],

$$\phi_k^{\mathrm{ext}}(\mathbf{r}) = \sum_i c_i \phi_n(\mathbf{r}-\mathbf{R_i}) \tag{1.18}$$

For the localized states the wave function is localized around a point, say $\mathbf{r_0}$, and decays exponentially around it as given below [32, 35],

$$\phi_k^{\mathrm{loc}}(\mathbf{r}) = \sum_i c_i' \phi_n(\mathbf{r}-\mathbf{R_i}) \exp(-|\mathbf{r}-\mathbf{r_0}|/\xi) \tag{1.19}$$

ξ is called the localization length. The three different types of wave functions are illustrated in figure 1.6.

As already mentioned, if the disorder is such that $W/B < 1$, there will be extended states at the band center and localized states at the band edges. The energy which separates the localized states from the extended states is called the mobility edge. Usually the mobility edge is not sharp; it is actually a transition region of finite width. If by varying the disorder or the electron density, the Fermi level can be moved across the mobility edge, a metal to insulator transition will occur [31]. Conduction in the localized states can occur via carrier hopping from one localized state to another. Depending on the temperature and disorder density, hopping can be between nearest neighbors or between states separated

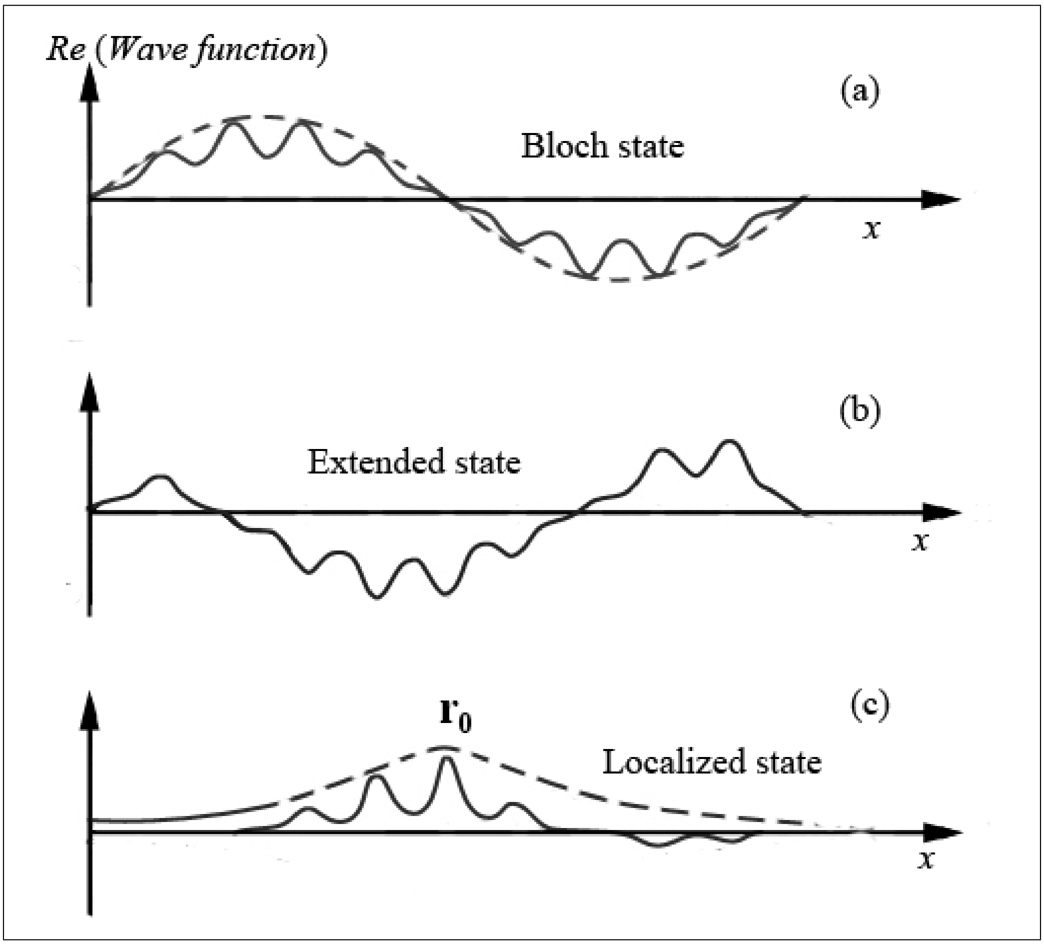

Figure 1.6: Illustration of (a) Bloch state in periodic potential, (b) extended state and (c) localized states in a disordered system [35, p. 227].

in energy as well as space. In case of nearest neighbor hopping (NNH) the conductivity as a function of temperature is given by [32],

$$\sigma = \sigma_0 \exp(-E_a/kT) \tag{1.20}$$

E_a is the activation energy for hopping. And in variable range hopping (VRH), neglecting the electron-electron interaction, the conductivity is [31]

$$\sigma = \sigma_0 \exp(-T_M/T)^{1/(d+1)} \tag{1.21}$$

Here, T_M is known as the Mott hopping temperature which depends on the density of states at the Fermi level and the Bohr radius of the localization centers. The conductivity in case of VRH depends on the dimensionality d of the system. Generally at low temperatures when sufficient number of empty states is not available near the filled states, the variable range hopping is the dominant phenomenon [31, 32]. With increasing temperature, the NNH probability increases. If the electron-electron interaction is taken into account for variable range hopping, the conduction mechanism is called Efros-Shlovskii hopping (ESH). In this case the conductivity in 3D systems is given by [32],

$$\sigma = \sigma_0 \exp(-T_{ES}/T)^{1/2} \tag{1.22}$$

T_{ES} is the ES hopping temperature that depends on the Bohr radius and the dielectric constant of the medium. EHS is generally seen in insulating systems at very low temperature. As the temperature is increased the hopping mechanism changes from ESH to VRH and then to NNH at higher temperature. At higher temperatures, a parallel mechanism of conduction in insulators could be activation of carriers from the localized states across the Fermi level to an extended state in the band center. It is called thermal delocalization of carriers. This will lead to band transport the nature of which is determined by different carrier scattering mechanisms [35], as already discussed in relation with the electrical properties of ZnO.

A strongly disordered system has no translation invariance, therefore momentum is not conserved and hence it is not a good quantum number. So the $E - k$ dispersion relation has no meaning. Instead a disordered system is characterized by its density of states. The phenomenon of localization depends on the dimensionality of the system. It has been shown by scaling theory that even the slightest amount of disorder can localize carriers in 2D and 1D systems [58]. However often in such cases the localization length is much larger than the sample size, thereby manifesting extended wave function and diffusive or weakly localized transport.

1.2.5 Effect of defects and disorder on photoluminescence

Some of the defects and disorder responsible for weak and strong localization of carriers in ZnO give rise to defect related luminescence as well. In fact this luminescence can sometimes be used to identify the defects present. In ZnO the two most prominent defect related luminescence bands are the green band centered around $\approx$ 2.4 eV and the orange red band centered around 1.9 eV. The origins of these two bands are often debated in literature. However it is certain that they involve some defect related transitions. The green band has been attributed by various authors to oxygen vacancy (V_O), Zinc vacancy (V_{Zn}) and to Cu substitutional impurity at Zn site (Cu_{Zn}). Van Heusden *et al.* attributed the green luminescence to transition from singly ionized oxygen vacancy [42]. However, recent theoretical calculations by Janotti and Van de Walle [25] and experiments by Reynolds *et al.*, Kohan *et al.* and Sekiguchi *et al.* [44–47] showed that the transition from conduction band or a shallow donor to a Zn vacancy (V_{Zn}) acceptor level is possible and has transition energy of about 2.5 eV. The origin of orange red luminescence is related to the presence of extra oxygen in the lattice. It may originate due to a transition from a shallow donor to a deep acceptor level, which may be related to the presence of additional oxygen in ZnO.

Apart from these native defects various extrinsic impurities present in the lattice may also give rise to defect related luminescence. For example Cu substitutional impurities give rise to strong green luminescence [43], Eu and Dy impurities give luminescence in red and yellow region [59, 60] respectively. These dopants are sometime intentionally introduced into ZnO lattice for the purpose of visible luminescence applications. As already discussed in connection with optical properties of ZnO, the excitons can bind with these defects to form bound excitons at low temperatures, the feature of which can be seen in low temperature photoluminescence spectra. The structural defects may also be responsible for luminescence in ZnO. One example is basal plane stacking fault in c-axis oriented ZnO films. The excitons confined in the quantum wells formed by the stacking faults are responsible for this emission at ≈ 3.321 eV [61].

The random potential fluctuations associated with the presence of disorder in the lattice broaden the near band edge (NBE) emission and absorption peaks. The reason is quite similar to the cause of bandgap narrowing. The electron-hole pairs and excitons will experience different potential at different point in the lattice due to the random distribution of defects. As a result their transition energies vary accordingly, broadening the emission as well as absorption peaks. By considering the standard deviation of a Gaussian potential fluctuation, the FWHM of the NBE transition peak has been calculated to be [62],

$$\Delta E_{\mathrm{FWHM}} = \frac{4e^2}{3\pi\epsilon}\sqrt{(N_D + N_A)\frac{\pi r_s}{3}}\,\exp(-3/4) \times \sqrt{2\ln 2} \tag{1.23}$$

Here ϵ is the dielectric constant, N_D and N_A are respectively donor and acceptor concentrations and r_s is the screening length.

1.3 Methodologies for growth of ZnO thin films

ZnO thin films have been grown by a variety of methods including sol-gel, chemical vapor deposition (CVD), metal-organic CVD (MOCVD), atomic layer deposition (ALD), pulsed laser deposition (PLD), RF and DC-sputtering, molecular beam epitaxy (MBE) etc. In this section we will give a brief overview of some of the important methods to grow epitaxial ZnO thin films.

1.3.1 Pulsed laser deposition (PLD)

PLD is a physical vapor deposition where a ceramic target of the material to be deposited is ablated by a high intensity pulsed laser beam and the ablated species are condensed on the substrate surface to grow the epitaxial film. PLD is highly suited for the growth of thin films of various oxides under non-equilibrium condition [63]. For PLD, generally a fast UV laser like KrF excimer or 3rd harmonic of a pulsed Nd:YAG laser is used. However as the PLD plume is highly forward directed, it is difficult to grow uniform thin films on large substrates. Another problem of PLD is particulate generation. Yet, PLD is a very popular method of growth for thin films of complex oxides including ZnO due to its inherent simplicity, congruent evaporation and ease of handling reactive oxygen, greater adhesion of the film to the surface and better film quality due to energetic plume species. The first report of the growth of ZnO thin films by PLD appeared in 1983 [64]. Since then there has been numerous reports on the growth of undoped and doped ZnO thin films on different substrates by PLD. Often during the growth of ZnO thin films by PLD, the deposition chamber is first evacuated and then filled with high purity oxygen to a pressure of about 10^{-6} to 10^{-2} mbar [2], depending on the sought characteristics of the films. The growth temperature used for ZnO thin films varies in the range from 400 to 850^0C. The PLD grown ZnO thin films are often found to have large grain size of $\approx$ 250 nm with very good crystalline quality [2]. The carrier density can also be varied by tuning the deposition condition and dopants in the range from $\approx 10^{16}$ to 10^{20} cm^{-3} [2]. PLD grown ZnO thin films grown under optimized conditions and appropriate substrates had very high electron mobility of about 400 cm^2/V-s [53]. Non-equilibrium nature of PLD facilitates growth of metastable alloys of ZnO such as MgZnO and CdZnO with Mg and CD contents far more than allowed by thermodynamic solubility limit [7,65]. p-type doping of ZnO by PLD has also been successfully achieved using N, P, As, Na, Li, Ag etc as dopant [2]. Moreover PLD have been used to grow quantum wells and quantum dots of ZnO as well [66].

1.3.2 Metal-organic chemical vapor deposition (MOCVD)

It is a type of chemical vapor deposition for the growth of single or polycrystalline thin films, especially of compound semiconductors using metal-organic precursors. The chemical reactions responsible for the growth typically take place in gas phase in moderate pressure. The gaseous mixture containing precursors of required composition for a particular semiconductor is passed over a heated substrate wherein the precursor molecules break up and form layers of the semiconductor on the substrate surface. MOCVD has been traditionally utilized for the growth of III-V semiconductors. However it has also been shown to be a suitable method for the growth of ZnO thin films. The organometallic precursors of Zn used for the growth of ZnO by MOCVD are diethyl zinc (DEZ) and dimethyl zinc (DMZ) [64]. Water, oxygen, nitrus oxide, ozone etc. along with a carrier gas such as dry nitrogen, has been used as the precursor of oxygen [67]. DEZ and DMZ are highly reactive with O_2, H_2O and ozone, resulting in severe premature reaction in gas phase which produce unwanted particulates in the grown films. This has motivated research to find alternative less reactive precursors like zinc propionate, zinc acetate etc. as source of Zn and CO_2, NO_2, N_2O etc. as source for O [67]. Separate inlets for the introduction of precursors of Zn and O have been used to reduce the problem of premature reaction. Growth of ZnO thin films with very good structural, optical, and electrical properties have been reported by various authors [65, 66]. The typical electron mobility of MOCVD grown ZnO thin films on alumina substrates have been found to be about 20 to 100 cm^2/V-s [68]. The FWHM of rocking curve of ZnO thin films on sapphire grown by MOCVD was found to as low as $\approx$ 100 to 255 arcsec [68]. Nitrogen doping for p-type doping of ZnO could also be achieved by MOCVD using NH_3 or N_2 plasma as precursors [69]. Phosphorous doped p-type ZnO has also been grown using P_2O_5 as the precursor of P [70]. Ternary alloy films of MgZnO and CdZnO have also been successfully grown using MOCVD [71, 72].

1.3.3 Atomic layer deposition (ALD)

Atomic layer deposition is a self limiting, surface controlled chemical vapor deposition method for the growth of thin films and nanostructures with atomic level control on the thickness and composition [73]. Like MOCVD, gas or vapor phase precursors are used in

ALD as well. However, unlike MOCVD, the precursors are fed onto the heated substrates sequentially. ALD reactions occur on the substrate surface in a self limiting manner, leading to the possibility of controlling the thickness and composition of the growing film down to the monolayer level. A simple ALD cycle consists of at least two different precursor pulses separated by a purging pulse of inert gas being fed into the reaction chamber containing the substrate. There are numerous reports in the literature about the growth of ZnO thin films by ALD. In most of these reports the precursors for Zn and O are DEZ and water respectively [74]. Other precursors like zinc acetate, DMZ, $ZnCl_2$ for Zn and ozone, N_2O, H_2O_2 for O have also been used [75]. However the growth of high quality ZnO in terms of structural, electrical and optical properties is a challenging task. The ALD grown ZnO films on alumina and glass substrates, especially those grown at lower temperature, are often found to be polycrystalline with no preferred orientation. At lower growth temperature there is the possibility of incomplete reaction and at higher temperature the growth is hindered due to precursor decomposition. It is only in a narrow range of temperature between 150 to 200^0C, that the growth of ZnO thin films on sapphire substrates using DEZ and water as precursors is found to be (0002) oriented [74]. The electron concentration in ALD grown ZnO thin films could be varied in the range from 10^{16} to 10^{20} cm^{-3} by changing the growth temperature and precursor pulsing and purging times. However the electron mobility in these films still remains low at $\approx$ 10 - 50 cm^2/V-s [74].

1.3.4 Molecular beam epitaxy (MBE)

In this method effusion cells containing the precursors are used to send molecular beams onto the substrate where they react and form the film under ultra high vacuum in non-equilibrium conditions [76]. Since the molecular beams can be switched off in less than the time to grow a monolayer, MBE provides high degree of control over the thickness and composition of the grown films. MBE is a well established growth technique for compound semiconductors. It has also been used to grow ZnO thin films as well [77]. High purity Zn metal evaporated from the effusion cell serves as the source of Zn and O_2 gas as the source of oxygen. Often oxygen plasma produced by electron cyclotron resonance and radio frequency ion sources are also utilized to produce atomic oxygen which enhance reaction with Zn. H_2O_2 and NO_2 vapor were also utilized as an alternative to oxygen plasma [78, 79]. MBE grown ZnO films on different substrates such as alumina and ZnO has been shown to be of high quality with FWHM of the rocking curve as low as .0050 with electron mobility as high as 260 cm^2/V-s [80]. The electron density in these ZnO filmed were in the range from 10^{17} to 10^{19} cm^{-3} [80, 81].

1.3.5 Sputtering

DC and RF field is used to sputter Ar ions onto a ceramic target containing the material to be deposited. The sputtered material then condenses on the substrate surface, growing the film [82]. Sputtering has been used to grow a variety of materials including metals, oxides, nitrides etc. An important advantage of sputtering is that even the materials with very high melting points can be easily sputter deposited. Compared to evaporated films, sputtered deposited films have greater adhesion to the surface. Since the sputtering system contains no hot parts, it is compatible with reactive oxygen. As a result there are multiple reports on the growth of ZnO thin films by sputtering. By varying the oxygen partial pressure during the growth, the resistivity of the ZnO thin films grown by sputtering could be tailored in a broad range [1, 2].

1.4 Literature review on effects of disorder on properties of ZnO thin films

In the existing literature there are some reports that show how the electrical and optical properties of the ZnO thin films grown by a host of methods gets affected by the presence of disorder. Disorder induced bandgap narrowing in ZnO thin films was first reported in 1982 by Roth *et al.* They found that the narrowing appeared suddenly at the electron concentration of $\approx 2 \times 10^{19}$ cm^{-3}, which is the about the density required for semiconductor to metal transition in ZnO [83, 84]. Lu *et al.*. and Sernelius *et al.* reported that the overall bandgap increase of Al doped ZnO thin films follows a combination of heavy doping induced Burstein-Moss shift and bandgap narrowing caused by carrier- carrier and carrier impurity interaction at high densities [55, 85]. There are few other reports as well on the heavy doping induced bandgap renormalization in doped ZnO thin films. Ye *et al.* reported bandgap renormalization in Ga doped ZnO thin films [86]. Kim and Park discussed variation of bandgap of In doped ZnO thin films as a function of In concentration. They found that at the electron concentration of $\approx 5 \times 10^{19} cm^{-3}$, the bandgap suddenly decreased due to merging of donor and conduction bands. Beyond this electron density the bandgap showed linear variation with further increase in the In concentration due to bandgap narrowing caused by impurity induced potential fluctuation or disorder [87].

The effect of random potential fluctuation on the photoluminescence properties of Ga doped ZnO was reported by Makino *et al.* [62]. They found that this random potential fluctuation actually caused a broadening of the near band edge photoluminescence peak. Apart from these, various defects and disorder give rise to defect related luminescence in the visible spectral region. Most prominent among them are the famous ZnO green and orange-red emissions. Vanhuesden *et al.* attributed the green luminescence to singly ionized oxygen vacancies [42]. However subsequent theoretical studies by Janotti and Van de Walle [25] and experimental data from Sekiguchi *et al.*, Reynolds *et al.* and Kohan *et* *al.* pointed that the green luminescence actually was related to Zn vacancy [44–47]. The green luminescence has also been known to originate due to unintentional Cu impurities in ZnO [43]. The orange-red luminescence is thought to be related to the presence of extra oxygen in the ZnO lattice [88].

The effects of disorder on the electrical properties undoped ZnO thin films have been studied by Nistor *et al.* [33]. They found that the presence of disorder brings about a transition from negative to positive temperature coefficient of resistivity (TCR) in the temperature dependent resistivity of ZnO thin films grown by MOCVD [33]. It was attributed to disorder induced weak localization. The effects of disorder induced weak localization and quantum corrections to conductivity was also studied by Bhosle *et al.* in Ga doped ZnO thin films [92] grown by PLD. They observed that with increasing Ga concentration the semiconducting ZnO films turned metallic. On further increasing the Ga concentration the films showed a transition from negative to positive TCR because of disorder induced weak localization. Liu *et al.* also found transition from negative to positive TCR at low temperature in case of boron doped ZnO thin films grown by MOCVD [89]. From the occurrence of negative magnetoresistance, they attributed the transition to disorder induced weak localization. The effects of weak localization and electron-electron interaction on the electrical properties In doped ZnO nanowires was studied by Thompson *et al.* [90].

1.5 Motivation for present thesis

In our discussion earlier in this chapter we have mentioned that ZnO is wide bandgap semiconductor with potential for applications in UV photonics, transparent conductors and electronic devices, solar cells, high temperature and radiation stable electronics etc. Many of these applications require ZnO thin films doped or alloyed with different elements such as Si, Al, In, Ga, N, P, Mg, Cd etc. These doped ZnO thin films are grown by a variety of methods. But irrespective of the growth method used, there would always be some degree of defects and disorder present in the doped ZnO films. We have discussed in this chapter that defects and disorders can significantly alter the electrical and optical properties of semiconductor thin films. Although in literature there are reports discussing disorder related effects in ZnO thin films, a systematic study on the effects of disorder on electrical and optical properties of doped ZnO thin films is essential. Such a systematic study on these issues would be beneficial for successful application of ZnO in photonic and electronics devices. In the present thesis we have carried out detailed studies on doped ZnO thin films deposited by pulsed laser deposition. Si and Mg have been chosen as the intentional impurities. The structural, electrical and optical properties of these doped ZnO thin films have been characterized by high resolution X-ray diffraction (HRXRD), photoluminescence (PL), photoabsorption (UV-Vis), Hall, resistivity, magnetoresistance measurements, X-ray photo electron spectroscopy (XPES) and secondary ion mass spectrometry (SIMS) to understand the effects of disorder on the electrical and optical properties of ZnO thin films.

Chapter 2

Growth of ZnO thin films by pulsed laser deposition and different characterization methods

Pulsed laser deposition (PLD) is a physical vapor deposition (PVD) method used for thin film deposition of a variety of materials [63]. In PLD a high-power pulsed laser beam is focused inside a vacuum chamber, called the PLD chamber, to strike a target of the material that is to be deposited. This material is vaporized or ablated from the target in the form of a plasma plume which gets deposited as a thin film on a suitable substrate such as a sapphire, glass, silicon wafer etc. which are positioned facing the target inside the PLD chamber [63]. This process can occur in ultra high vacuum or in the presence of a reactive background gas, such as oxygen or nitrogen. PLD is particularly suited for the growth of oxides wherein oxygen is commonly used as the background gas to fully oxygenate the deposited films. Apart from thin films, quantum dots, wells, nanostructures of different materials including oxides, nitrides, metals etc. have also been successfully grown using by PLD [66, 91–94]. Even carbon nanotubes, C_{60}, diamond, graphite and graphene could be grown by PLD [95–99].

Soon after the technical realization of the first laser in 1960 by Maiman, Smith and Turner utilized a ruby laser to deposit the first thin films in 1965 [100]. However, the deposited films were still of inferior quality to those obtained by techniques such as CVD and MBE. The breakthrough in thin film growth by PLD came in 1987 when D. Dijkkamp, Xindi Wu and Venkatesan *et al.* were able to laser deposit a thin film of the high temperature superconducting material $YBa_2Cu_3O_7$ which was of superior quality to that of films deposited with alternative techniques [101]. Since then, Pulsed Laser Deposition has been utilized to fabricate high quality crystalline films of different material [66, 91–99]. The development of new laser technology in the 1990s, such as lasers with high repetition rate and short pulse durations, made PLD a very competitive and widely used tool for the growth of thin films and nanostructures with complex stoichiometry. Although the basic PLD setup is simple compared to many other deposition techniques, the physical phenomena of laser-target interaction and film growth are quite complex as discussed in the following paragraphs [63].

2.1 PLD Process

PLD process consists of the ablation of the target material by the laser pulse, the development of a plasma plume with high energetic species, and the crystalline growth of the film on the heated substrate. The process of PLD can broadly be divided into four stages:

2.1.1 Laser ablation of target and creation of plasma

The laser-mater interactions responsible for the ablation of target material and the plasma formation are very complex processes. PLD process is a non-equilibrium process where the removal of atoms from the bulk material is done by melting and vaporization of the target material at the surface region [102]. The incident laser pulse penetrates into the surface of the material within the penetration depth which is dependent on the laser wavelength and the target material and is typically of the order of few nm for most materials [63]. The strong electric field of the laser pulse is sufficient to remove the electrons from the bulk material of the penetrated volume. This process occurs within the first 10 ps of a nanosecond laser pulse and is caused by non-linear processes such as multiphoton ionization [102]. The free electrons oscillate due to the oscillating electromagnetic field of the laser light and can interact with the atoms of the target material, thus transferring a part of their energy to the lattice of the target material within the surface region. The timescale for electron-phonon coupling is of the order of picoseconds. As a result of these interactions between the oscillating electrons and the target atoms, the surface of the target is heated up and the material is melted and vaporized [102]. The electronic excitation upon irradiation by laser pulse is enhanced by the presence of microscopic cracks at the surface, voids, and nodules which increase the electric field. The vaporized material cloud shields the target surface from further irradiation and can absorb energy from the remaining of the laser pulse through inverse Bremsstrahlung [103]. As a consequence the ablated material gets more and more ionized and the temperature of the plume increases to as high as 20000 K. The energy of the plume species can be as high as 100 eV and their velocity (u) distribution follows a drifted Maxwellian function with a center of mass velocity normal to the surface as given by $P(u) \approx u^3 \exp\left[-m(u-\bar{u})^2/2kT\right]$, where m is the mass of the particles, T temperature and $\bar{u}$ is the velocity of the center of mass of the plume [102]. The high pressure resulting from the high temperature propels the materials forward with very high velocity in the form of PLD plume [104, 105]. As a result of expansion the plume cools to about 3000 to 5000 K [106].

2.1.2 Plume dynamics

In the second stage, the material expands in the form of plasma normal to the target surface towards the substrate due to Coulomb and recoil forces from the target surface [63]. The spatial distribution of the plume around the normal vector to the target surface is dependent on the background gas pressure inside the PLD chamber. The PLD plume is highly forward directed and the density of the plume can be described by a $\cos^n \theta$ law, where θ is the angle with respect to the target normal [63, 102, 107]. The value of n typically ranges from 2 to 20, depending on the laser fluence and background gas pressure [102]. Presences of a background gas enhance the scope of multiple scatterings of the plume species, leading to a lower value of n and hence plume broadening. In the initial stage after material ejection from the surface, the plume is very narrow and forward directed and there is almost no scattering with the background gases [102]. In the intermediate stage splitting of the high energetic ions from the low energetic ones occurs. Finally the plume suffers a diffusion-like expansion of the species contained in it. In this stage the scattering of the ablated species is dependent on the mass of the background gas and it can influence the stoichiometry of the grown film. If the background gas pressure is increased, the high energetic species of the plume will slow down. The rationale of using background gas is either to thermalize the plasma species through multiple collisions, or to compensate for the loss of an elemental component of the target through incongruent ablation [108]. Background gas has also been used to enable gas phase condensation for the growth of nanoparticles [109]. Studies have shown that particles with kinetic energies more than 50 eV can resputter the film already deposited on the substrate resulting in a lower deposition rate, a change in the stoichiometry of the film and poor surface morphology [110]. The narrow and highly forward directed plume is responsible for one of the major disadvantage of PLD. It limits the maximum substrate size where uniform film can be grown to only few cm^2 [111].

2.1.3 Deposition of ablated material on substrate

This is an important stage of PLD process which determines the quality of the deposited films. The high energetic species ablated from the target constantly bombard the substrate surface and may damage the surface by sputtering off atoms from the surface [110]. The incoming plume species may also cause defects formation in the deposited film due to sputtering. The sputtered species from the substrate and the incoming plume particles from the target together form a collision region. This collision cloud serves as a source for condensation of particles on the substrate [112]. If the condensation rate is sufficient, equilibrium can be reached and the film grows on the substrate surface at the expense of the direct flow of ablation particles. The advantages of pulsed laser deposition over other deposition technique is its pulsed nature leading to precise thickness control, possibility of carrying out surface chemistry far from thermal equilibrium, and under appropriate condition the possibility to obtain thin film with the same chemical composition as the target even for highly complex cases. Another advantage offered by PLD for the growth of crystalline thin films is the high energy of the incident plume particles, which help in better quality crystal growth [102].

2.1.4 Nucleation and growth of film

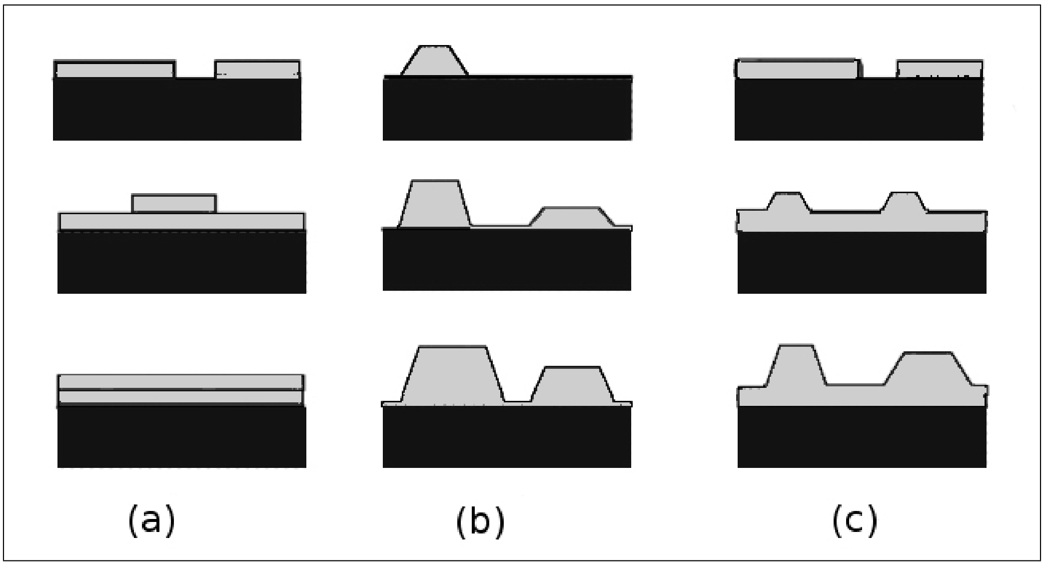

Figure 2.1: (a) layer-by-layer growth, (b) island growth and (c) Stranski-Kastronav growth modes.

The nucleation and growth of the film deposited by PLD depend on several growth parameters. Laser parameters such as the laser fluence, wavelength, pulse duration and degree of ionization of the plume affect the film quality, stoichiometry and the deposition flux [63, 113]. The nucleation density is found to generally increase with increasing deposition flux which can be attained by increasing the laser fluence. The laser pulse duration dictates the nature of laser-target interaction [63]. For example in case of pico and nanosecond lasers there can be melting of the target material, but in case of femtosecond laser, the target material is ejected without melting [102]. The penetration depth of the laser energy in the bulk of the target is determined partly by the laser wavelength. The penetration depth in turns decides particulates formation in the grown films due to either splashing or exfoliation [102]. Another important parameter is the substrate temperature. The nucleation density generally increases as the substrate temperature is increased. The condition of the substrate surface also determines nucleation and growth. The substrate surface condition can be modified by chemical etching, pre-deposition annealing, miscut and roughness of the substrate etc [113]. Lattice mismatch between the substrate and the grown film can also control the growth mechanism. Often during the growth of oxides reactive oxygen background gas is used to maintain stoichiometry of the grown film. However precise tuning of the background gas pressure is needed. For example if the background gas pressure is too low, the film may be off stoichiometric and if the gas pressure is too high the growth rate will decrease and gas phase condensation can happen resulting in poor quality thin films [102]. Moreover extra oxygen may get incorporated in the film, undesirably modifying the film properties [114]. A large supersaturation occurs on the substrate during the pulse duration of the plume in PLD. The plume pulse lasts around 10 to 40 microseconds depending on the laser parameters. This high supersaturation causes a very large nucleation density on the surface increasing the smoothness of the deposited film [63]. Depending of the growth parameters and the substrate conditions, three different growth modes are possible. Those are as follows [63, 113]:

(a) Layer-by-layer or Frank-van der Merwe growth - In this growth mode, adatoms attach preferentially to surface sites resulting in many 2D islands on the substrate surface until a critical island density is reached. As more material is added, the islands continue to grow sideways until the islands begin to run into each other. This is known as coalescence. Even after coalescence the surface generally will have a large number of pits which are filled by subsequent of addition of materials from the condensation cloud till the 2D layer is complete. This process is repeated for each subsequent layer. It is shown pictorially in figure 2.1a. It is called layer by layer or 2D growth because a complete layer is first formed before the growth of the subsequent layers [63, 115]. This kind growth will be promoted by strong film-substrate bonding, low film surface energy and high substrate surface energy. In this growth mode there is no free energy barrier.

(b) 3D or island or Volmer-Weber growth mode - In this growth mode the adatom-adatom cohesive force is stronger than the adatom-substrate adhesive force. As a result the nucleation centers grow in a three dimensional way leading to the formation of 3D islands or clusters. The growth of these islands or clusters will results in rough multilayer film to grow on the substrate surface [116]. It is shown in figure 2.1b.

(c) Stranski-Kastranov growth or mixed growth mode - It is an intermediary process characterized by both 2D layer and 3D island growth. The film initially grows in 2D layer by layer fashion. However after about 1 to 5 monolayers the 2D growth may change to three-dimensional island growth due to a change in the energy situation with the addition of successive monolayers. This might be an increase in stress with increasing layer thickness due to mismatched lattice spacing. Transition from the layer-by-layer to island-based growth occurs at a critical layer thickness which is highly dependent on the chemical and physical properties, such as surface energies and lattice parameters, of the substrate and film [63, 113, 117]. It is schematically shown in figure 2.1c.

2.2 Pulsed laser deposition of pure and doped ZnO thin films

First report of the growth of ZnO thin films by PLD appeared in 1983 [118]. Thereafter hundreds of reports were published in scientific literature detailing the growth of high quality ZnO thin films by PLD and the characteristics of the ensuing ZnO films. The lasers that are most commonly used for the PLD growth of ZnO are either KrF excimer at 248 nm or 3rd harmonic of pulsed Nd:YAG at 355 nm [1,2]. Almost always during the growth, oxygen ambient at different partial pressure is used. In the following subsections we outline the deposition conditions and growth parameters that we used in our experiments.

2.2.1 Target Preparation

A high quality, high density target is very important to grow good quality thin films by PLD. For PLD of ZnO a variety of targets including ceramic ZnO pellet, single crystal ZnO, Zn metal have been used. However for best result a high density and uniform ceramic pellets is the most preferred one among these [63]. The ZnO ceramic target used during our experiments were made in-house using ceramic processing root. High purity ZnO powder (99.9995% from Alfa Aesar) obtained from commercial sources was used for this purpose. Using a suitable die-press the powder was made into pellets of $\approx$ 1.5 cm diameter and 2 to 3 mm thickness. These pellets were subsequently sintered at 1200^0C for two hours to obtain the high density ceramic targets. The heating and cooling of the target was carried out at $\approx$ 50^0C per min. The density of the ZnO target was determined to be about 95%. For making the $Mg_xZn_{1-x}O$ pellets required for bandgap engineering, MgO and ZnO powders were properly mixed in suitable concentration in a agate mortar. The mixed powder was then calcined at 1000^0C for 4 hours to ensure uniform reaction. The calcined powder was again grinded in a mortar pestle and palletized the same way as done for ZnO pellet. Finally the pellets were sintered at 1400^0C for two hours to obtain the ceramic targets. The surface of the as prepared targets were polished before each deposition and pre-ablated prior to the growth. The target was rotated as well rasterized during growth to get uniform target erosion and uniform rate of deposition and also to reduce the chance of target surface deterioration which would otherwise result in lot of particulate in the grown film.

2.2.2 Substrates

For the growth of ZnO thin films a variety of substrates have been used. These include alumina, glass, GaP, Si, Ge, GaP, GaN, $ScAlMgO_4$, CaF_2, ZnO, SiC and even plastics and clothes [1]. Among these the single crystal alumina is perhaps the most popular substrates for the growth of epitaxial thin films of ZnO because of its similar crystalline structure, small difference in lattice parameters, high thermal and structural stability, high thermal conductivity, availability of high quality and large size single crystals, affordability and high transparency in UV-visible spectral range [2]. We have used c-axis oriented (0001) single crystal alumina substrates (Impex HighTech Ltd., Germany) for the deposition of ZnO thin films and bilayers by PLD. These substrates were epipolished on both sides with surface roughness smaller than 0.5 nm. The FWHM of ω-rocking curve of alumina (0006) peak was $\approx$ 16 arc sec. Before loading in to PLD chamber, the substrates were cleaned by ultrasonicating in tricholoroethylene (TCE), acetone and methanol followed by rinsing in de-ionized water. The alumina substrates were then dried using dry nitrogen gas flow and mounted on heater using either clamp or silver paste.

2.2.3 Growth conditions

We used KrF excimer laser for most of the depositions. The pulse duration of the laser was 20 ns. The laser fluence in our experiments was maintained in the range from 0.8 to 1.2 J/cm^2. The PLD chamber was evacuated before each deposition to a base pressure

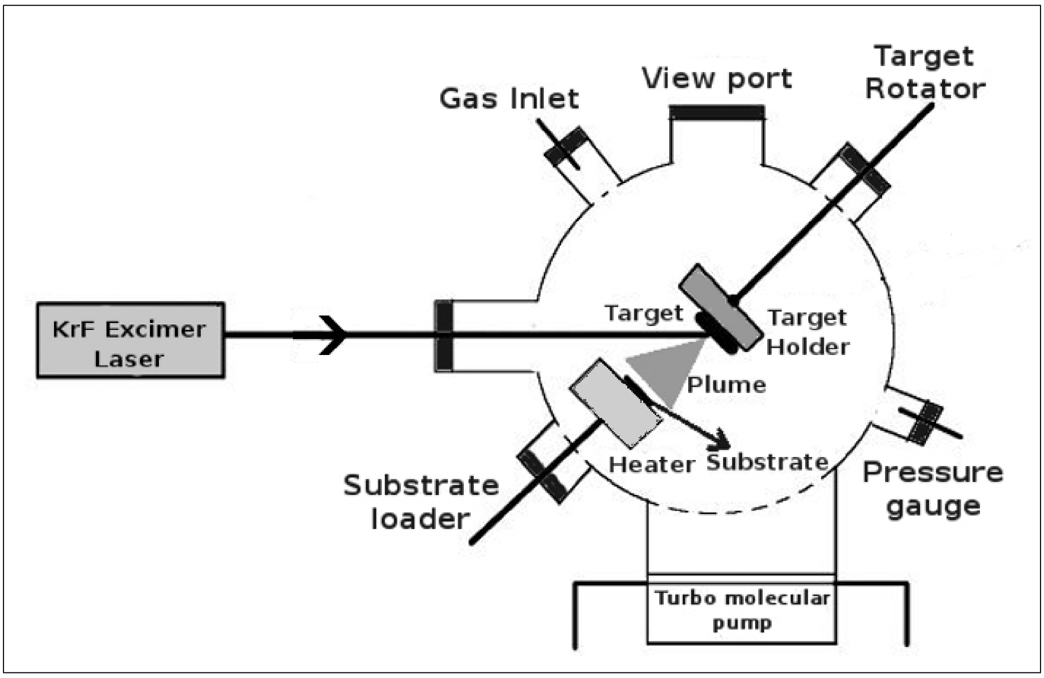

Figure 2.2: Schematic of a PLD system.

of ≈10^{-6} mbar and it was filled with high purity oxygen gas to a pressure of typically in the range from 1×10^{-5} to 1×10^{-2} mbar, depending on the growth requirements. The exact growth parameters for different studies have been mentioned in the corresponding chapters. In this section we briefly describe a modified PLD scheme, henceforth referred as sequential PLD, that we have used in some of our studies.

(a) Sequential PLD - This PLD scheme was introduced first to grow CdZnO alloy and Sn doped CdO thin films by PLD, as it was difficult to make the corresponding targets [38, 119]. We have used sequential PLD scheme to grow Si doped ZnO thin films. This method allowed us to achieve very low doping concentrations which are otherwise difficult to achieve using a single target. Traditional PLD uses a ceramic target of a suitable composition to deposit the films. In case of very lightly doped ZnO thin films it was difficult to make the corresponding pellets as that required mixing a tiny amount of dopant with comparatively large amount of ZnO powder and mix them properly. There was always the risk of inhomogeneous mixing. As a consequence, during ablation the grown films may have random composition. Moreover, since the dopant concentration is very small, the mixing process will increase the chance of significant contamination during handling. This problem can be circumvented by using two different targets - one of the ZnO and the other of the dopant material during deposition. These targets are ablated sequentially many number of times till the desired thickness is achieved keeping the ratio of durations of ablation of the two targets fixed for a particular film. For example for a specific doping concentration, the ZnO target was ablated for ten seconds and the dopant target for 1 second. This cycle was repeated a large number of times till the desired thickness of the films were achieved. Before starting each deposition both the target surfaces were polished and pre-ablated to reduce the risk of contamination and particulate formation due to exfoliation. The exact deposition conditions used for the growth of Si doped ZnO thin films by sequential PLD has been mentioned in the corresponding chapters 3 and 4.

2.3 Characterization methods of ZnO thin films

In this section we provide a brief discussion on the basic principles of the experimental methods used to characterize the PLD grown undoped and doped ZnO thin films.

2.3.1 Electrical characterization

Electrical properties of doped ZnO thin films were measured using four probe resistivity, Hall, and magnetoresistance measurement methods to study the effects of defects and disorder. These methods are described briefly in the following sections.

(a) Four probe van der Pauw resistivity measurement - The temperature dependent resistivity measurements of the ZnO thin films were carried out in van der Pauw four probe geometry [120, 121] using a standard lock-in amplifier. The typical size of the ZnO thin films were 5 mm × 5mm. Indium contacts were made on the four corners of

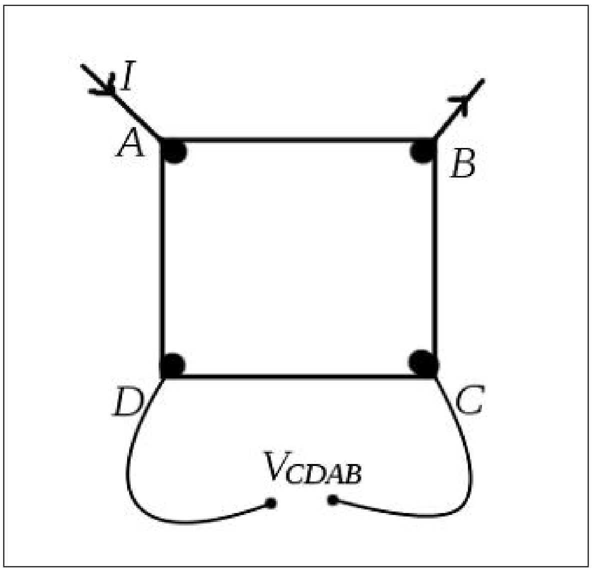

Figure 2.3: Sample geometry for van der Pauw four probe measurements.

the samples as shown in figure 2.3. The contacts were annealed at 400^0C in nitrogen atmosphere to ensure proper connection to the sample. The linearity of the contacts was confirmed by I-V measurement. 19 Hz ac signal from the output of the lock-in amplifier was applied to the sample through standard high resistor connected in series with the sample. The resistance of this standard resistor was chosen to be much higher than the sample resistance so that the resistor coupled with the output of the lock-in amplifier formed an ideal current source. A set of voltage measurements across the sample were made by sending a known current (I) through the sample. To explain the method, let us define the following voltages:

V_{ABDC} = Voltage between A and B while current is passing from D to C,
V_{DCAB} = Voltage between D and C while current is passing from A to B,
V_{BACD} = Voltage between B and A while current is passing from C to D,
V_{CDBA} = Voltage between C and D while current is passing from B to A,

$$R_H = \frac{V_{ABDC} + V_{DCAB} + V_{BACD} + V_{CDBA}}{4I} \tag{2.1}$$

V_{ADBC} = Voltage between A and D while current is passing from B to C,

V_{BCAD} = Voltage between B and C while current is passing from A to D,

V_{DACB} = Voltage between D and A while current is passing from C to B,

V_{CBDA} = Voltage between C and B while current is passing from D to A,

$$R_V = \frac{V_{ADBC} + V_{BCAD} + V_{DACB} + V_{CBDA}}{4I} \tag{2.2}$$

Then as shown by van der Pauw, the sheet resistance (R_S) of the sample will be given by [120, 121],

$$e^{-\pi R_V/R_S} + e^{-\pi R_H/R_S} = 1 \tag{2.3}$$

Since for a square sample $R_V = R_H = R$, therefore sheet resistance will be given by,

$$R_S = \frac{\pi R}{\ln 2} \tag{2.4}$$

In general R_V is not exactly equal to R_H and the formula for sheet resistance is modified to,

$$R_s = \frac{\pi}{\ln 2} \frac{R_H + R_V}{2} f(R_H, R_V) \tag{2.5}$$

where $f(R_H, R_V)$ is called the van der Pauw correction function and is given by,

$$\frac{1}{2} \exp\left(\frac{\ln 2}{f}\right) = \cosh\left(\frac{R_H - R_V}{R_H + R_V} \times \frac{\ln 2}{f}\right) \tag{2.6}$$

The resistivity (ρ) of the films can then be calculated from the measured sheet resistance if the thickness (t) of the film is known. The resistivity is given by [120, 121],

$$\rho = R_S t \tag{2.7}$$

The samples were mounted on the cold finger of a cryostat and by varying the sample temperature resistivity of the samples could be measured as a function of temperature.

(b) Hall measurement - The carrier concentration of the ZnO thin films were determined using Hall measurement [122]. It was also carried out in four probe van der Pauw geometry using lock-in amplifier. To measure the Hall voltage, a known current (I) was sent across two diagonal ends of the sample and the voltage was measured across the other diagonal in presence of a perpendicular magnetic field. The magnetic fields as well as the direction of current flow were reversed and the data were noted. In this case also let us define the following voltages (referring to figure 2.3):

V_{ACBD+} = Voltage across A and C with current flowing from B to D and +B magnetic field,

V_{CADB+} = Voltage across C and A with current flowing from D to B and +B magnetic field,

V_{ACBD-} = Voltage across A and C with current flowing from B to D and -B magnetic field,

V_{CADB-} = Voltage across C and A with current flowing from D to B and -B magnetic field,

$V_{AC} = V_{ACBD+} - V_{ACBD-}$

$V_{CA} = V_{CADB+} - V_{CADB-}$

V_{BDAC+} = Voltage across B and D with current flowing from A to C and +B magnetic field,

V_{DBCA+} = Voltage across D and B with current flowing from C to A and +B magnetic field,

V_{BDAC-} = Voltage across B and D with current flowing from A to C and -B magnetic field,

V_{DBCA-} = Voltage across D and B with current flowing from C to A and -B magnetic field,

$V_{BD} = V_{BDAC+} - V_{BDAC-}$

$V_{DB} = V_{DBCA+} - V_{DBCA-}$

Then the Hall voltage is given by,

$$V_H = \frac{V_{AC} + V_{CA} + V_{BD} + V_{DB}}{8} \tag{2.8}$$

The carrier concentration can be calculated from the Hall voltage using the fact that,

$$V_H = \frac{IB}{n_S e} \tag{2.9}$$

where e is the electronic charge and n_S is the sheet carrier concentration. If the thickness of the films are t, then the volume carrier density (n) is given by,

$$n = \frac{IB}{V_H e t} \tag{2.10}$$

From the sign of the Hall voltage the carrier type can also be determined. The quantity $1/ne$ is given the name of Hall coefficient (R_H). If the Hall factor (r_H) is taken into account, then Hall coefficient is given by [122],

$$R_H = \frac{r_H}{ne} \tag{2.11}$$

The Hall factor depends on the scattering mechanism and if with changing temperature the scattering mechanism changes, then Hall factor will vary as well. Typically the value of Hall factor is close to 1. Therefore, by measuring the Hall voltage as a function of temperature for a given sample the temperature dependence of the carrier concentration in that sample can be measured. If the resistivity (ρ) of the sample is also known from resistivity measurement, then the carrier mobility can be calculated by using,

$$\mu = \frac{1}{ne\rho} \tag{2.12}$$

A magnetic field of ≈ 0.5 T was used for most of the Hall measurements in our studies.

(c) Magnetoresistance measurements - It is basically resistivity measurement in presence of an applied magnetic field [122]. The change is resistivity when an external magnetic field is applied to the sample is called the magnetoresistance (MR). It is often expressed as percentage of zero field resistance and given by,

$$\%MR = \frac{R_{SF} - R_{S0}}{R_{S0}} \times 100 \tag{2.13}$$

Where R_{SF} is the sheet resistance in presence of a magnetic field and R_{S0} is the sheet resistance in zero field. The sheet resistances were measured in four probe van der Pauw geometry. Similar to Hall and resistivity measurements, the temperature dependence of magnetoresistance can be determined by mounting the samples in a suitable cryostat. Also by changing the magnitude of the magnetic field magnetoresistance as a function of field can be plotted.

(d) Cryostat - For temperature dependent electrical measurements the samples were mounted in a CCR cryostat, which could vary the sample temperature in the range from 4.2 to 310 K. Here CCR stands for closed cycle refrigerator. Closed-cycle cryostat consist of a chamber through which cold helium vapour is pumped. An external mechanical refrigerator extracts the warmer helium exhaust vapor. This extracted helium vapor is again cooled and recycled. CCR cryostat consume a relatively large amount of electrical power, but need not be refilled with helium. As a result these can run continuously for an indefinite period. Samples can be cooled by attaching them to a metallic coldplate (inside a vacuum chamber) in thermal contact with the helium vapor chamber. The temperature of the coldplate is measured accurately by using suitable resistance thermometers like Cernox (Zirconium oxy-nitride) and rhodium-iron RTDs or Si diodes based temperature sensors.

2.3.2 Optical characterization

To determine the effects of defects and disorder on the optical properties of doped and pure ZnO thin films photo-absorption and photoluminescence measurements were carried out on the grown films. The basic principles of these techniques are given below.

(a) Photo-absorption measurements - According to Beer-Lambert law the intensity of light passing through a sample of given thickness t suffers exponential reduction in intensity given by [29],

$$I = I_0 \exp\left[-\alpha(\nu)t\right] \tag{2.14}$$

Where I_0 is the initial intensity and I is the intensity after passing through the sample of thickness t and $\alpha(\nu)$ is called the absorption coefficient of the material which depends on the frequency (ν) or wavelength of light. In case of a semiconductor if the energy of the incident photons ($h\nu$) are less than the bandgap E_g, the absorption coefficient is very small in magnitude and light almost pass completely through the sample. However when the incident photon energy approaches the bandgap energy, the absorption coefficient start to increase and at $h\nu = E_g$, there is a sudden increase in the absorption. In fact under parabolic band approximation for a direct bandgap semiconductor, the absorption coefficient is related to the incident photon energy by the following formula [29],

$$\alpha\nu = A\left(h\nu - E_g\right)^{1/2} \tag{2.15}$$

where A is a material dependent constant. In figure 2.4 $\alpha(\nu)$ is plotted as a function of $h\nu$, which is known as the absorption spectrum. However this simple relationship gets modified if significant band tail states are present in the semiconductor due to various defects and disorders. The transitions between this band tail states can change the absorption spectrum near the band edge. In such cases there will be significant absorption below the absorption edge due to the band tail states and instead of a sharply rising band edge, an exponentially increasing band edge is found in the absorption spectrum [29]. This is known as Urbach's tail and the absorption coefficient for photon energies less than the bandgap is approximately given by [29, 123],

$$\alpha(\nu) = C\exp\left(\frac{h\nu - E_1}{E_0}\right) \tag{2.16}$$

where C, E_0 and E_1 are constants determined by fits to experiments. The constant E_0 is related to the impurity concentration and disorder.

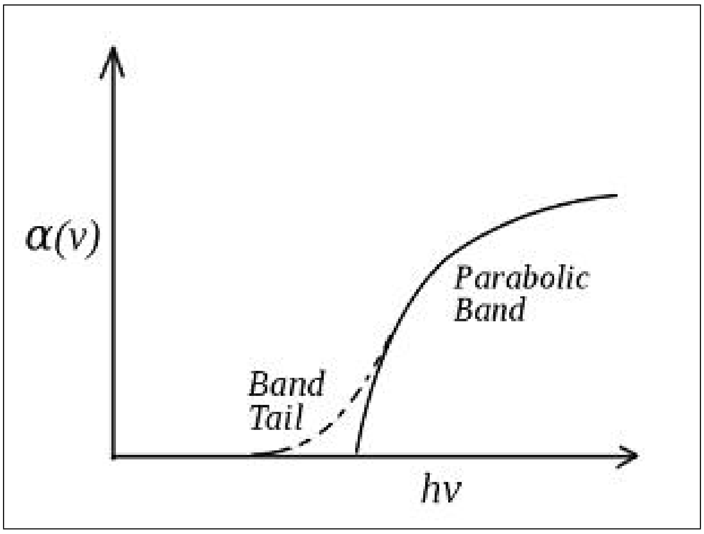

Figure 2.4: Continuous line shows variation of α with hv whereas dashed line represents Urbach's tail.

Moreover excitons can exist in the semiconductor under given conditions [29, 35]. In such cases for direct bandgap semiconductors at energies slightly lower than the bandgap energy, a series of sharp absorption peaks in the form of delta function corresponding to different exciton resonances can appear. With increasing temperature the exciton peaks generally broadens. Since the excitons can be created with some kinetic energy, higher energy photons can also create them thereby contributing a component to the absorption coefficient in the region of band to band transitions [29].

The instrument used to measure the photo-absorption spectrum is known as the spectrophotometer. For ZnO thin films generally an UV-VISIBLE spectrophotometer is used. It consists of a white light source light from which light is dispersed through a monochromator and selected using a slit. The selected monochromatic light is split into two components. One component of the split beam is used as the standard and other is passed through the sample. From the ratio of the two light beams the absorption coefficient can be determined using proper baseline correction. The schematic of a UV-VISIBLE spec-

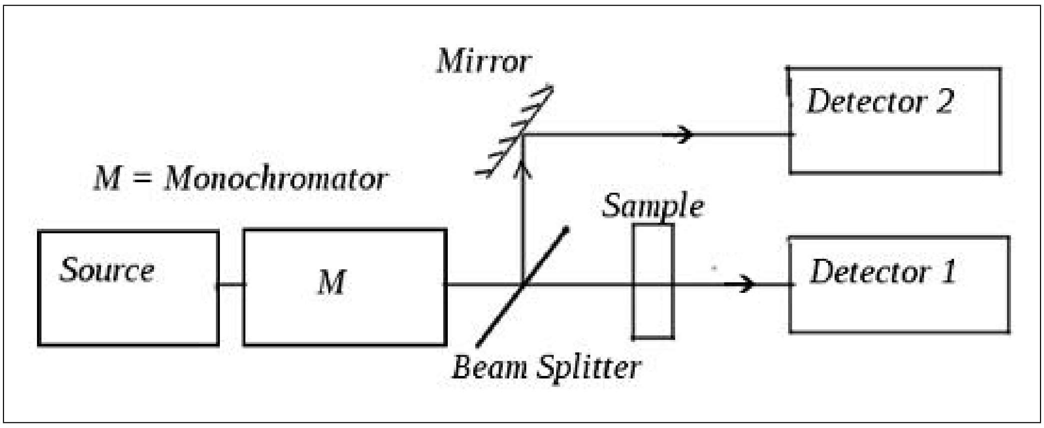

Figure 2.5: Schematic of a UV-VISIBLE spectrophotometer.

trophotometer is shown in figure 2.5.

(b) Photoluminescence (PL) measurements - The different radiative recombination processes occurring in the semiconductor give rise to the luminescence spectrum [29, 123]. For this to happen the semiconductor first have to be excited by using a suitable light source with photon energies higher than the bandgap energy of the semiconductor. This incident light will create electron-hole pairs, free excitons, excitonic complexes, bound excitons etc. depending on the semiconductor and its conditions. Some of the excited species subsequently can recombine radiatively giving rise to the phenomena of photoluminescence. The typical PL measurement system consist of a suitable excitation source, which is often a laser of appropriate wavelength, a spectrometer, a detector in the form of either CCD or photo multiplier tube (PMT) and necessary collecting optics. A schematic of a typical PL set-up is shown in figure 2.6. For PL measurements of ZnO thin films, we have used a He-Cd laser lasing at 325 nm as an excitation source. A CCD detector coupled to a 0.5 m spectrometer has been used to detect the PL spectrum. The sample is mounted in a cryostat so that the temperature of the sample can be varied in the range from 4.2 to 300 K. As ZnO is a direct bandgap semiconductor with high exciton binding energy, the near band edge PL spectra of ZnO is dominated by excitonic recombination. At lower temperature the bound excitons are dominant whereas at higher temperature the free excitons. The photoluminescence spectra of ZnO may give valuable information about the quality of the films and the various defects and disorder present in it [2].

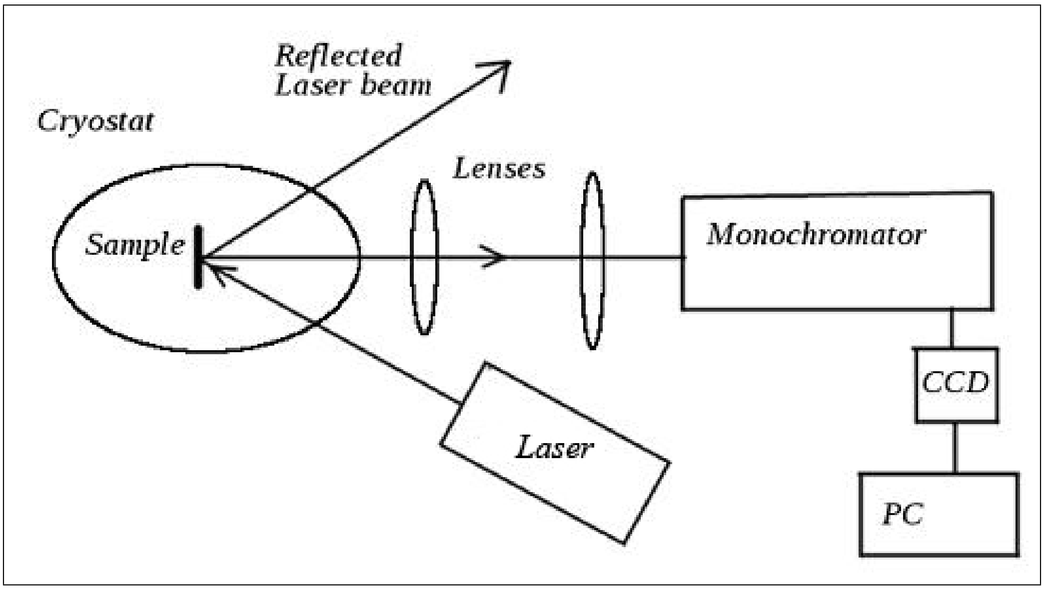

Figure 2.6: Typical schematic of photoluminescence measurement set-up.

2.3.3 Structural characterization

The structural quality of the ZnO thin films were determined using high-resolution X-ray diffraction measurements [124]. The $\omega - 2\theta$ scan and ω-rocking curves provide important information about the crystalline quality of the ZnO thin films. Moreover Williamson-Hall plot have been used to distinguish the different components causing the broadening of the XRD peaks. The surface morphology of the films was studied using atomic force microscope. A brief discussion about the basic principles of these measurements follows.

(a) High resolution X-Ray Diffraction (HRXRD) - HRXRD is one of the most widely used techniques to investigate the crystalline structure of thin films. When X-rays interact with a crystalline substance, a diffraction pattern is formed. Each crystalline solid has its characteristic X-ray diffraction pattern, which may be used as a "fingerprint" for its identification [124]. Depending on the experimental setup, XRD can be used to per-

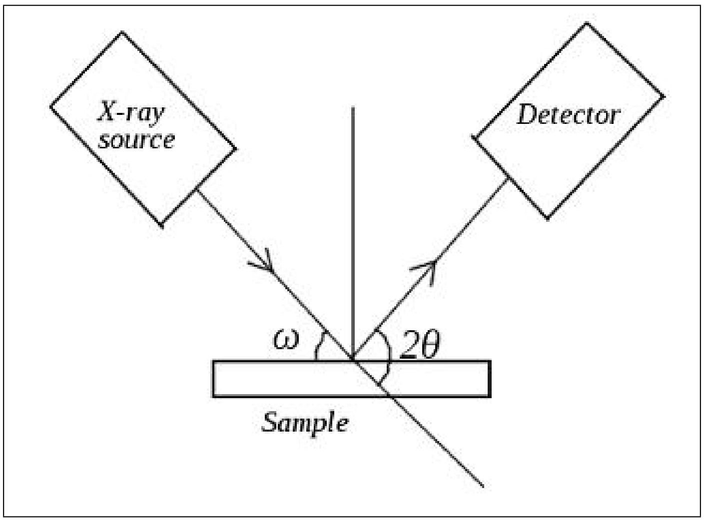

Figure 2.7: Typical geometry of X-ray diffraction with angle of incidence ω and diffraction angle 2θ.

form different tasks such as determination of crystal structure, lattice parameters, grain size, phase composition, residual and micro strain, epitaxial quality, and orientation relationships. X-ray diffraction pattern is formed when the well known Bragg condition is satisfied for a set of crystal planes and incident x-ray i.e.,

$$2d \sin\theta = n\lambda \tag{2.17}$$

where d is the lattice spacing and λ is the wavelength of incident X-ray, θ is the diffraction angle as shown in figure 2.7. n is the order of diffraction. For epitaxial thin films the most widely used HRXRD methods are $\omega - 2\theta$ scan, ω-rocking curve, ϕ-scan and Williamson-Hall plot, where ω and 2θ are angles of incidence and diffraction respectively (figure 2.7).

In $\omega - 2\theta$ scan both ω and 2θ are varied. This is achieved by rotating the sample as well as the detector about an axis perpendicular to the page (refer to figure 2.7) but the incident beam direction is kept unchanged [124]. The detector is rotated by an angle twice that of the sample rotation. When the Bragg condition is satisfied, a diffraction peak is obtained. This method is used to identify the planes. If there is uniform strain or change in lattice parameter then the position of the peak shifts from the original value. Moreover the broadening of the $\omega - 2\theta$ is caused by microstrain and finite vertical coherence length. Therefore, from the peak position in the $\omega - 2\theta$ scan, the crystalline structure and macro strain or lattice parameter can be calculated. On the other hand the peak width or broadening can provide information about the microstrain or vertical coherence length.

In ω-scan, the positions of the detector as well as incident beam is fixed and the sample is rotated or "rocked" by a very small angle around the ω-axis. This is ω scanning and it is done to find out if there is any mismatch between the adjacent unit cells or grain boundaries. For a perfect crystal the width of the ω-rocking curve is infinitesimal. However due to finite lateral size of the grains and their orientation mismatch, the ω-rocking curve is broadened. Therefore, from the width of the rocking curve, the lateral coherence length or lateral grain size and tilt between the grains with respect to each other can be calculated [125].

Williamson-Hall plot [126] can be used to identify the contributions of each of vertical coherence length and microstrain in the width of $\omega - 2\theta$ peak. As per the Debye -Scherrer law the vertical coherence length is related to the peak width (FWHM) in $\omega - 2\theta$ scan by the relation [124],

$$\beta_S = \frac{0.9\lambda}{\delta \cos\theta} \tag{2.18}$$

where δ is the vertical coherence length. Again the broadening (FWHM) due to microstrain (ϵ) is given by,

$$\beta_M = 4\epsilon \tan\theta \tag{2.19}$$

Combining these two equations total broadening,

$$\beta = \beta_S + \beta_M \rightarrow \frac{\beta \cos\theta}{\lambda} = \frac{0.9}{\delta} + \frac{4\epsilon \sin\theta}{\lambda} \tag{2.20}$$

Therefor from a plot of $(\beta \cos\theta/\lambda)$ vs. $(\sin\theta/\lambda)$, the contributions of microstrain and vertical coherence length to the overall $\omega - 2\theta$ peak broadening can be separated. This plot is called the Williamson-Hall plot [126]. The slope of the plot will give a measure of microstrain whereas the y-axis intercept will give the vertical coherence length. From a similar kind of analysis of the ω-rocking curve, the contributions of lateral coherence length and tilt to the broadening of ω-rocking curve can also be differentiated [127].

ϕ-scan is performed by rotating the sample about an axis perpendicular to the thin film surface [127]. It is used to find epitaxial relationship between the substrate and the thin film. Typically in XRD measurements Cu - K_α X-ray radiation (1.54 Å) is used which is further monochromatized using Ge crystals.

(b) Atomic force microscopy - Atomic force microscopy (AFM) is a very high-resolution scanning probe microscopy, with resolution on the order of fractions of a nanometer, more than 1000 times better than the optical diffraction limit [128]. Atomic Force Microscope (AFM) utilizes a sharp probe (tip) moving over the surface of a sample in a raster scan. The probe is a tip at the end of a cantilever made of silicon or silicon nitride, which bends in response to the force between the tip and the sample [129]. The radius of curvature of the tip is of the order of nanometers. Typically, the deflection of the tip is measured using a laser spot reflected from the top surface of the cantilever into an array of photodiodes (figure 2.8). To prevent damage to the tip due to collision with the surface being probed, a feedback mechanism is often employed to adjust the tip-to-sample distance to maintain a constant force between the tip and the sample. Generally the AFM probe or the sample is mounted on a stage containing three piezo crystals, with each responsible for scanning in the x, y and z directions [130]. The AFM can be operated in a number of modes, depending on the application. The possible imaging modes in general, can be divided into static or contact modes and a variety of dynamic (non-contact and tapping) modes where the cantilever is made to oscillate [128, 130]. In contact mode, the tip is dragged across the surface of the sample and the contours of the surface are measured either directly using the deflection of the cantilever or using the feedback signal required to keep the cantilever at a constant position with respect to the surface [128]. In non-contact mode, probe does not contact the sample surface. The cantilever is instead made to oscillate at or

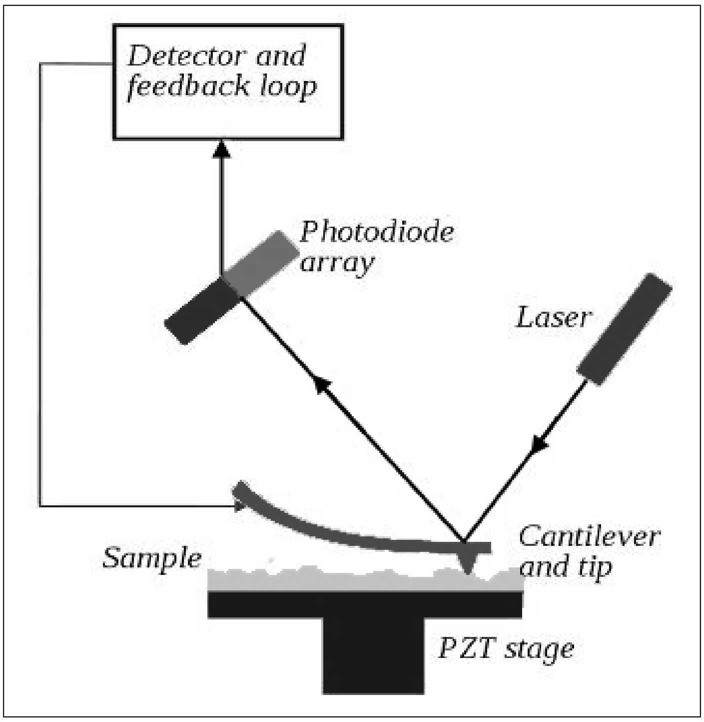

Figure 2.8: Schematic of AFM set-up.

near its resonant frequency where the amplitude of oscillation is typically less than a few nanometers. The van der Waals forces or any other long-range force that extends above the surface decreases the resonance frequency of the cantilever. The feedback loop system of the AFM using this decrease in resonant frequency as the input, maintains a constant oscillation amplitude or frequency by adjusting the average tip-to-sample distance. The scanning software constructs a topographic image of the sample surface by measuring the tip-to-sample distance at each (x, y) data point [131]. In tapping mode as well, the cantilever is made to oscillate up and down at or near its resonance frequency similar to non-contact mode. However, the amplitude of this oscillation is greater than that in non-contact mode (typically 100 to 200 nm). The interaction of forces acting on the cantilever when the tip comes close to the surface cause the amplitude of this oscillation to decrease as the tip gets closer to the sample. The feedback loop maintains the oscillation amplitude by adjusting the height of the tip over the sample surface. From this height variation topographical imaging of the surface can be obtained. Thus in tapping mode, the AFM image is produced by imaging the force of intermittent contacts of the tip with the sample surface [132].

2.3.4 Compositional analysis

It is essential to study the composition in case of doped ZnO thin films to find the concentration of dopant and thus to get an estimate of the degree of disorder present in the film. We have used secondary ion mass spectrometry, x-ray photoelectron spectroscopy and energy dispersive x-ray analysis for compositional characterization of the doped ZnO thin films grown by PLD. The basic principles of these methods are discussed here in brief.

(a) Secondary ion mass spectrometry (SIMS) - It is a mass spectrometry technique that is used to analyze the composition of solid surfaces and thin films by sputtering the specimen surface with a focused primary ion beam and collecting and analyzing ejected secondary ions [133, 134]. The charge to mass ratios (e/m) of these secondary ions are measured with a mass spectrometer to determine the elemental composition of the surface to a depth of about 1 to 2 nm. SIMS is the most sensitive surface analysis technique, with elemental detection limits as low as parts per million to parts per billion. Although SIMS is generally considered to be a qualitative technique, quantification is possible with the use of standard samples. A typical SIMS consists of a primary ion gun which generates the primary ion beam, a primary ion column to focus the primary ions onto the sample surface, secondary ion extraction lenses, a mass analyzer and an ion detection unit. All these are contained in a high vacuum chamber. The primary ions may be generated by ionizing the noble gases, oxygen, SF_5, C_{60}, Cs etc [133]. The mass analyzer can be of three different types - sector, quadrupole and time of flight. A sector type mass spectrometer uses a combination of an electrostatic and a magnetic analyzer to separate the secondary ions by their charge to mass ratio. In quadrupole mass analyzer the secondary ions are separated by resonant electric fields, which allow only the selected masses to pass through. The time of flight (TOF) mass analyzer separates the secondary ions in a field-free drift path according to their drift velocity. Since all the ions possess same kinetic energy, their velocity and hence their time of flight in the field free drift path varies according to their mass. It can be stressed here that it is the only mass analyzer type able to detect all generated secondary ions simultaneously, and is the standard analyzer for SIMS instruments. The ion detector is typically a Faraday cup or an electron multiplier. Depth profiling of elemental composition can also be done using SIMS by the use of an additional etching gun. We have used TOF-SIMS in all our SIMS measurements [133, 134].

(b) X-ray photoelectron spectroscopy (XPES) - It is a surface sensitive and quantitative electron spectroscopic method that measures the elemental composition, empirical formula and chemical and electronic state of the elements that exist within a few nanometers of the surface of a given specimen. XPES spectra are obtained by irradiating a material surface with a beam of X-rays while simultaneously measuring the kinetic energy and number of the photoelectrons that escape from the top 0 to 10 nm of the material [52]. The typical elemental detection limit of XPES is about parts per thousand. The binding energy (E_B) of the photoelectron in XPES is determined from the following formula,

$$E_B = h\nu - (E_k + \phi) \tag{2.21}$$

where $h\nu$ is the energy of the incident X-ray photons, E_k is the kinetic energy of the detected photoelectrons and ϕ is work function of the spectrometer. In XPES spectra the number of photoelectrons is plotted against the binding energy. Peaks are obtained in the XPES spectra at binding energies corresponding to the different atomic energy levels of the elements present in the material. Typically Al-K_α line at 1486.7 eV or Mg- K_α line at 1253 eV are used as the X-ray source. Other primary components of an XPES system are electron focusing lenses, an electron energy analyzer (hemispherical analyzer), an electron detection system etc. All of these components are enclosed in a high vacuum chamber [135, 136]. In case of ZnO thin films XPES could provide with valuable information regarding not only the chemical compositions but also about oxygen vacancies and interstitials present in the films.

(c) Energy dispersive X-ray analysis (EDX) - It is a technique used for the elemental or compositional analysis of a specimen. EDX is based on the emission of characteristic X-rays when the specimen is irradiated with a high energy electron beam. The incident high energy electron can eject an inner shell electron from an atom, thereby creating a hole. This hole can be subsequently filled by an outer shell electron of the same atom along with the emission of characteristic X-rays. Since the photon energies of the characteristics X-rays are unique for each element, elemental analysis is possible by detecting the emitted characteristic X-ray photons. Typical EDX system consists of an electron gun with accelerating and focusing lenses, X-ray detector, pulse processor and the analyzer [137].

2.4 Error analysis

Error analysis is very important in any experiment. The experimental data is quite meaningless without specified error. In scientific context error refers to unavoidable imprecision in measurements. Since it is not always possible to measure things with arbitrarily high precision, it is important to quantify the imprecision of the results in the form of error. Errors can be classified into two main categories - random error and systematic error. Random errors are errors, which fluctuate randomly from one measurement to the next. They yield results distributed about some mean value. Random errors can be reliably estimated by repeating measurements. Standard deviation is used as a measure to quantify random error. On the other hand systematic errors are errors, which tend to shift all measurements in a systematic way so their mean value is displaced. Systematic errors are caused by a flaw in the equipment or in the design of the experiment. These may be such things as incorrect calibration of equipments, consistently improper use of equipments or failure to properly account for some effect. Large systematic errors must be eliminated in a good experiment. But small systematic errors are always present. For instance, no instrument can ever be calibrated perfectly. It is not possible to estimate systematic errors by repeating the experiment with the same equipment. In order to identify systematic errors, the nature of the experiment and the instruments involved have to be properly understood.

If the quantity to be calculated is the function of two or more variables independently measured, the error in the final result may be calculated as follows. For simplicity of typing, we consider the quantity of interest z to be a function of two variables x and y which are independently measure, *i.e.* $z = f(x, y)$. The absolute error in z, Δz is given by,

$$\Delta z = \sqrt{\left(\frac{\partial f}{\partial x}\right)^2 (\Delta x)^2 + \left(\frac{\partial f}{\partial y}\right)^2 (\Delta y)^2} \tag{2.22}$$

where Δx and Δy are respective absolute errors in x and y.

In case of doped ZnO thin films grown by pulsed laser deposition, the growth process itself is a major source of variation in the obtained electrical and optical properties of the films. Even if the growth conditions like substrate temperature, laser fluence, target to substrate distance are strictly monitored, a slight change in position of the substrate on the surface of the heater or the condition of the target and substrate surfaces or small fluctuations in the laser fluence during the ablation (which are difficult to control) can change the films properties significantly. Moreover in case of electrical measurements the size of the contacts used is yet another source of error. The bigger the contact sizes, larger will be the proportion of error. For temperature dependent electrical measurements the samples are often mounted in a CCR cryostat, the vibration from which can also add random noise to the experimental data. In case of optical measurements, the improper wavelength calibration and inaccurate measurement of response function of the spectrograph can add errors to the measured photoluminescence and photoabsorption spectra. Besides all these factors, the instrumental limitations will always be a source of finite error in the experimental results.

Chapter 3

Effects of disorder on electrical and optical properties of Si doped ZnO thin films at ambient temperature

ZnO is doped by different impurities to tailor its electrical and optical properties for specific applications [2,91]. Being a wide bandgap semiconductor with transparency in the visible spectral region and inherent n-type conductivity, ZnO is considered to be a very good material for transparent conducting electrode applications [91,138] in display panels, solar cells, transparent non-volatile memories etc. It's suitability is further enhanced by the fact that ZnO can be easily doped with various n-type dopants such as Al, Ga, In etc. [4,54,55,139–141] which increase the carrier concentration and hence the conductivity of ZnO film. The rugged wurtzite structure of ZnO ensures that even after doping, the crystalline quality of the ZnO thin films is reasonably good so that relatively high electron mobility and low resistivity can be obtained [4–6]. For example, in case of Ga doped ZnO, the minimum resistivity has been found to be $\approx 8.12 \times 10^{-5}$ ohm-cm with a carrier concentration of $\approx 10^{22}$ cm^{-3} [54] at Ga concentration of ≈ 5 wt%. Others have also found minimum resistivity varying from $\approx 8.1 \times 10^{-5} - 1.69 \times 10^{-3}$ ohm-cm [4,139,140] in Ga doped ZnO films. In case of Al doped ZnO the resistivity was found to be about 1.3×10^{-4} ohm-cm [141]. Si, being in group IV, also acts as a donor and hence enhance the carrier concentration and conductivity of ZnO [142]. Silicon can be a very useful dopant in ZnO for TCE application due to its ease of availability, low cost, ease of doping and good quality of the ensuing films. During doping, the impurity atoms occupy positions in the ZnO lattice at random causing substantial disorder. As a result, apart form the desired property of enhanced electrical conductivity, the disorder caused by the introduction of these atoms in ZnO lattice brings about with it a hoard of other effects like bandgap narrowing and band tailing, photoluminescence peak broadening, weak localization and even strong localization of electrons [32, 35]. In this chapter we will present the results of our studies on the room temperature electrical and optical properties of Si doped ZnO thin films deposited by sequential pulsed laser deposition [38, 119]. We show that Si doping indeed causes semiconductor to metal transition, bandgap narrowing and PL peak broadening in the ensuing ZnO thin films.

3.1 Growth and characterization

All the films were grown on single crystal (0001) alumina substrates by sequential ablation of separate ZnO and Si targets using the 3rd harmonic of a Q-switched Nd:YAG laser (355 nm), operating at 10 Hz. Laser fluence was maintained at $\approx$ 1 J/cm^2. The sintered ZnO target was prepared in-house from high purity ZnO powder. Single crystal Si wafer was used as the other target. Concentration of Si in the films was controlled by varying the durations of ablation of ZnO and Si targets. The duration of ablation of Si target was fixed at 1 sec while that of the ZnO target was varied from 10 to 50 sec. These sequences were repeated number of times to get the desired film thicknesses of $\approx$ 150 nm in each case, which was measured using a DEKTAK surface profilometer. The alumina substrates were cleaned prior to deposition using traditional organic cleaning procedure and then rinsed thoroughly in deionized (DI) water and finally dried using dry nitrogen gas jet. The deposition chamber was initially evacuated to a base pressure of $\approx 1 \times 10^{-6}$ mbar using a turbo-molecular pump and during the deposition a pressure of $\approx 1 \times 10^{-4}$ mbar of flowing high purity oxygen gas (99.999%) was maintained. The substrate temperature was kept at $\approx 600^0$C with an accuracy of $\pm 1^0$C to facilitate homogenized doping of Si in ZnO. The composition of Si doped ZnO thin films were studied using energy dispersive x-ray (EDX) measurements. The crystalline characteristics of these films were studied using high resolution X-ray diffractometer with a resolution of $\approx$ 5 arcsec. The optical properties of these films were studied at room temperature using optical transmission and photoluminescence spectroscopy. A UV-Visible spectrophotometer was used to record the transmission spectra of these films at room temperature. For PL measurements a 20 mW HeCd laser operating at 325 nm was used as the excitation source and PL was collected and detected through a 0.5 m long spectrometer attached with a CCD detector. The Carrier concentration, mobility and resistivity of these films were measured by using Hall measurement in four probe van der Pauw configuration. For these measurements, Indium contacts were made on the films which were subsequently annealed in vacuum at $\approx 400^0$C for $\approx$ 2 minutes to allow proper mixing of the Indium with that of the ZnO films. The linearity of the I-V curves was checked to ensure ohmic nature of these contacts.

3.2 Structural and compositional characteristics

The incorporation of Si in ZnO matrix was confirmed by EDX measurement, which showed conspicuous peak of Si besides the characteristic peaks of Zn and O. The concentration of Si in the films was estimated using the respective EDX spectra and is shown in the figure 3.1. It can be seen that the Si concentration in these films increased monotonically with increasing Si to ZnO ablation duration ratio . The incorporation of Si in ZnO along the growth direction can be considered to be uniform due to the fact that the thickness of the grown ZnO layer in each sequence varies form 1 nm to 5 nm for different samples considering a growth rate of 0.1 nm per second. In an work by Skriniarova *et*

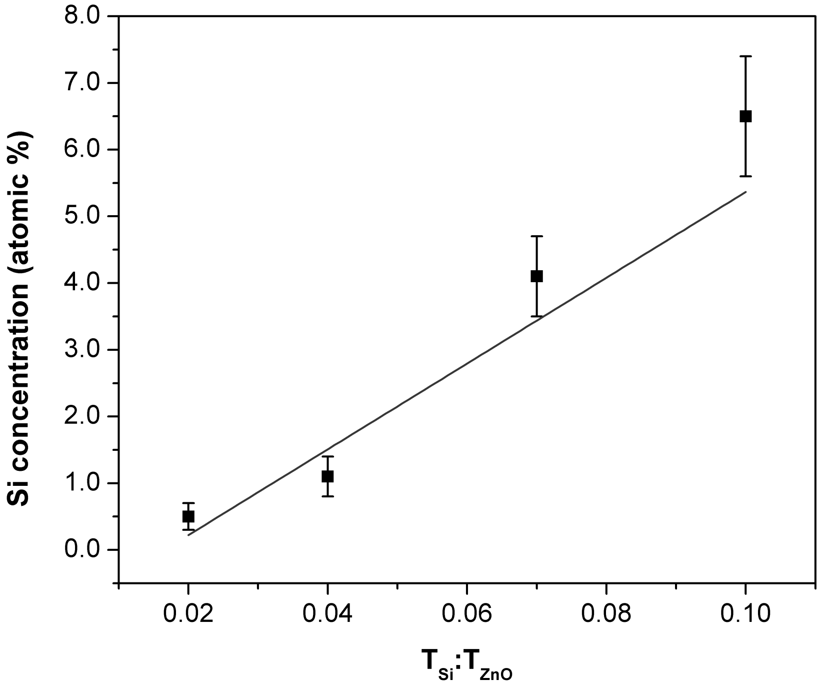

Figure 3.1: Dependence of Si concentration on T_{Si}/T_{ZnO} .

al. [143], the diffusion lengths of Si in ZnO in case of ZnO: Al films deposited on Si substrate by sputtering and subsequently annealed at 500^0C was reported to be about 8 and 14 nm respectively for the as grown and the annealed samples as measured by SIMS. In our case the thickness of ZnO layer was much less than the reported diffusion lengths of Si in ZnO and the deposition temperature was higher $\approx 600^0$C. Moreover the kinetic energy of impinging plume particles in case of PLD is very high compared to that in Sputtering. In addition in our films each ZnO layer is sandwiched between two Si layers. So it is expected that Si will diffuse into every ZnO layer both from top as well as bottom interface resulting nearly uniform distribution of Si in ZnO in the growth direction. The bandgap of Si doped ZnO films showed monotonic increase with increasing Si concentration, which is an indication of proper mixing of Si in ZnO along the growth direction. Earlier Misra et al [38] had also found using RBS in the case of ZnO-CdO sequential ablation that the mixing of ZnO and CdO in the growth direction was uniform.

Figure 3.2 shows normal $\theta - 2\theta$ x-ray diffraction (XRD) patterns of the Si doped ZnO films with Si concentration of $\approx 0.5\%$ and that of pure ZnO thin film grown under the same deposition conditions for comparison. The ω rocking curves of (0002) ZnO peak for both the films are shown in inset of the same figure. It can be seen that the ZnO thin films with and without Si doping are both c-axis oriented and in pure wurtzite phase having only (0002) reflection of ZnO. The full width at half maximum (FWHM) of ω rocking curve of (0002) Si:ZnO peak was found to be $\approx 0.55^0$ compared to $\approx 0.25^0$ for the undoped ZnO thin films, indicating deterioration in the crystalline quality due to enhancement in the strain and other crystalline defects on doping with Si.

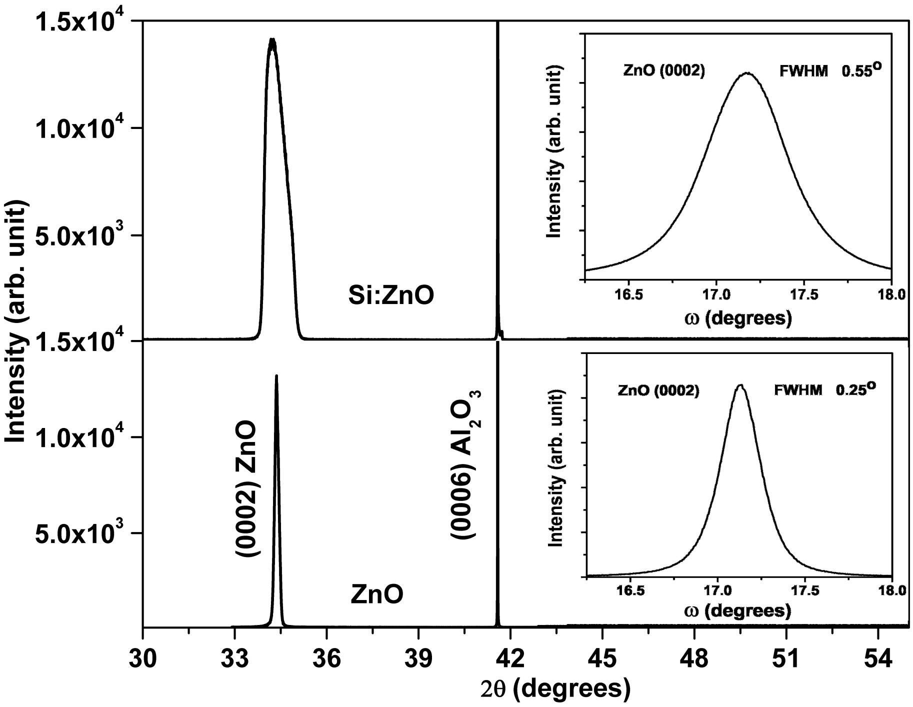

Figure 3.2: Normal $\theta - 2\theta$ XRD pattern of pure ZnO and ≈ 0.5 atomic % Si doped ZnO films. Insets show corresponding ω rocking curves.

However the resulting broadening of the (0002) ZnO peak with increasing Si concentration is found to be within the limits of suitability for its application as transparent conducting electrode. One may notice here that the normal XRD pattern of Si:ZnO appears to be slightly asymmetric and broadened around the central peak. The broadening of the XRD peak in the $\theta-2\theta$ scan arises either due to limited vertical coherence length or micro-strain. In our case since the thickness of the film is about 150 nm it does not contribute significantly to broadening. On the other hand the micro-strain which is related to the density of point defects and other structural defects arising due to Si doping seems to be mainly responsible for observed unusual broadening of peak. Inhomogeneous in-plane distribution of these point defects throughout the film may give rise to a broad distribution of lattice parameters and hence unusually and asymmetrically broadened peak in $\theta - 2\theta$ scan [144] as observed in our case. Therefore the broad and asymmetric XRD peaks are an indication of the presence of disorder in the Si doped ZnO thin films which are to be expected due to random distribution of Si atoms. Moreover the lattice disturbance created by Si incorporation also brings with it other kinds of defects like Zinc vacancy, oxygen interstitials and SiO_x particulates as discussed later in this section.

3.3 Electrical properties

Variation of electrical resistivity of the films as a function of Si concentration is shown in figure 3.3. Resistivity of the undoped ZnO films was found to be about 3.0×10^{-2} ohm-cm. As can be seen from this figure, the resistivity first decreased rapidly and reached a minimum value of 6.2×10^{-4} ohm-cm and then increased slightly with increase in the Si concentration in the films. Si being a group-IV element can act both as donor as well as acceptor. If Si occupies the Zn lattice sites or the interstitial sites it will act as donor and if it goes to the O lattice site, it will act as acceptor. However the Hall measurement of the films confirmed that all the films were n-type, indicating that Si was indeed acting as a donor dopant in ZnO, occupying Zn sites and donating free electrons to the ZnO lattice.

The variation of n-type carrier density and mobility with Si concentration is shown in figure 3.4. On increasing Si concentrations up to 6.5 atomic % in the ZnO films, the carrier density increased to $\approx 3.25 \times 10^{20}$ cm^{-3} which is higher than the Mott critical

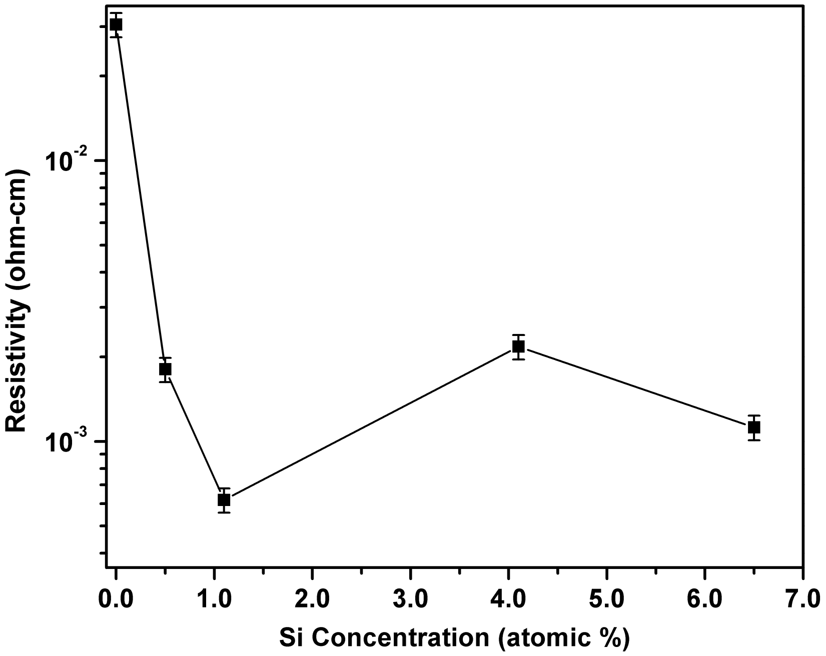

Figure 3.3: Variation of resistivity of Si:ZnO thin films with Si concentration.

density in ZnO. This indicated a semiconductor to metal transition caused by Si doping. Moreover, the observed carrier concentration in these films was found to be less than that of the concentration of added Si and as can be seen from figure 3.4, the carrier density initially increased rapidly with increasing Si concentration up to $\approx$ 1.1 atomic % and then steadily, showing a tendency of saturation. To understand the observed behavior of Si doping in ZnO we have carried out XPS measurements on one of the representative sample (with Si concentration 4.1 atomic %). The XPS spectrum of the Si $2s$ core level is shown in the figure 3.5.

This $2s$ peak could be deconvoluted using standard Gaussian peak fitting algorithms into four Gaussian peaks at peak energies 154.2 eV, 153.1 eV, 152.4 eV and 151.1 eV as shown by dashed curves in the same inset. These four peaks imply that Si actually exists in four different oxidation states in ZnO films, namely, Si^{+4}, Si^{+3}, Si^{+2}, Si^{+1} [145]. The Si in Si^{+4} state in ZnO means either the presence of SiO_2 kind of bonds or that Si goes to Zn

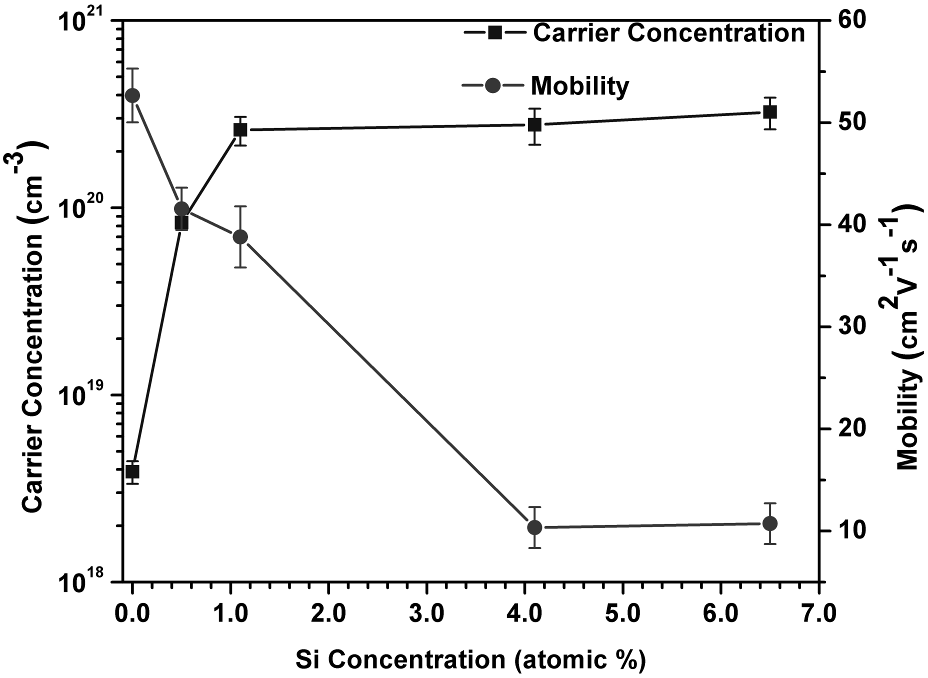

Figure 3.4: Variation of carrier concentration (n) and mobility (μ) in Si doped ZnO thin films with different Si concentrations.

lattice sites and donate two electrons. But the probability of the latter is energetically much lower after the donation of first electron due to the build up of positive charge at the Si ion. Two other peaks namely, Si^{+2} and Si^{+1} are possibly due to the formation of Si_2O_2 or Si_2O kind of bonds. Si in Si^{+3} state implies that either Si is going to the Zn sites and donating one electron to the lattice or formation of Si_2O_3 kind of bonds in ZnO lattice. Among these four possible valence states the dominating contribution is from Si^{+3} as can be seen in figure 3.5. Si can donate significant free electrons in Si^{+3} state substituting Zn in ZnO lattice. The reason for observed lower free electron concentration compared to Si doping concentration in the samples may be understood considering the nature of Si oxide formation in ZnO lattice during the growth. It is anticipated that, initially when the Si doping concentration is low, the Si is predominantly substituting Zn in ZnO lattice in Si^{+3} state thereby donating one electron for each Si dopant and enhancing the carrier concentration rapidly. However with increasing Si concentration in ZnO, the probability

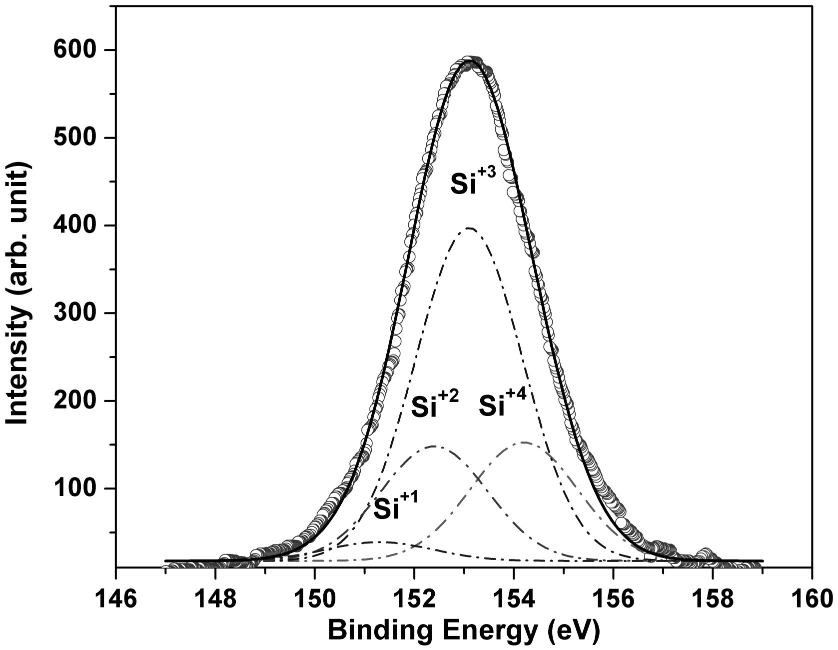

Figure 3.5: XPS spectrum of the Si $2s$-core level and its deconvolution into four peaks in the film with Si concentration of 4.1 atomic %.

of formation of various SiO_x kinds of bonds and their segregation along grain boundaries increases. In these cases Si remains electrically inactive in ZnO lattice and does not donate free electrons. Therefore the carrier concentration shows a tendency of saturation. These defects do not usually contribute to the optical transmission studies and being in feeble concentration, they are also not visible in XRD patterns. This kind of variation of electron concentration with increasing doping concentration has also been reported in Ga doped ZnO films where at higher Ga concentrations Ga-O bond formation occurs at the grain boundaries [146] which does not contribute further to carrier concentration. Further acceptor kind of defects like Zn vacancy and O interstitials may arise in ZnO films at higher doping concentrations [86]. The SiO_x segregation along the grain boundaries is expected to increase the disorder in the films which will result in reduced electron mobility due to enhanced scattering. This can be seen in figure 3.4 which shows the variation of mobility with Si concentration. The mobility of the undoped ZnO films, which was ≈ 52 cm^2/V-s was found to decrease with increasing Si concentration and reached a minimum value of ≈ 10 cm^2/V-s for higher Si concentrations. The increased electron-electron, electron-impurity and grain boundary scatterings are also responsible for the reduced mobility. This also explains the observation stated earlier of slight increase in the resistivity beyond Si concentration of about 1.1 atomic % as shown in figure 3.3. The reduced mobility with increasing Si concentration in the ZnO films also implied that disorder in the films increased with increasing Si doping.

3.4 Optical properties

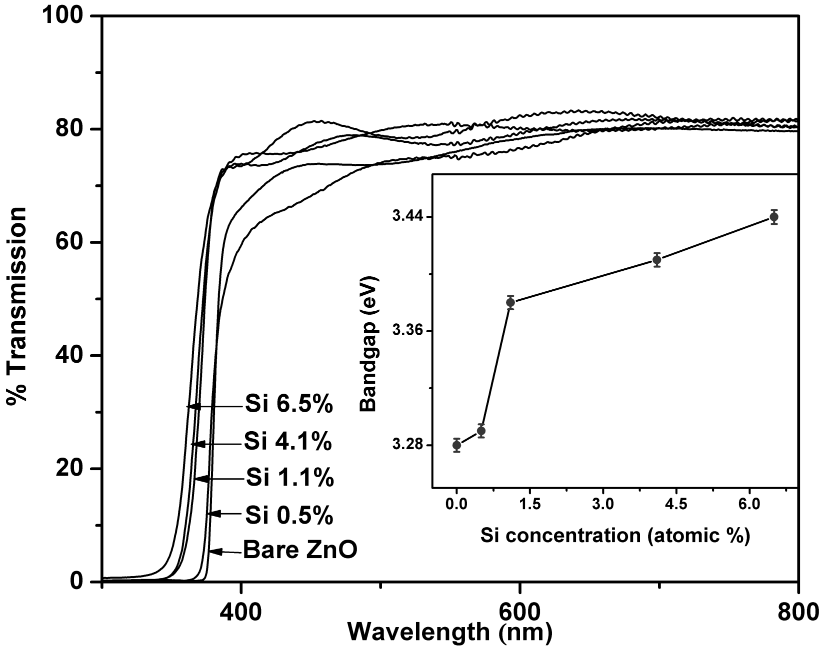

Figure 3.6: Transmission spectra of Si doped ZnO thin films with different Si concentrations. Inset shows variation of ZnO bandgap with different Si concentrations.

Transmission spectra of the films were recorded using a UV-visible spectrophotometer in the wavelength range from 250 to 800 nm, which are shown in figure 3.6. All the films were found to be highly transparent with an average transmission of $\approx 80\%$ in the visible spectral range. Using these transmission spectra the bandgap of these films were calculated from the α^2 vs $h\nu$ plot by extrapolating the linear portion of the curve to $h\nu = 0$. Variation of the ZnO bandgap with increasing Si doping concentration is shown in the inset of figure 3.6. It is clear that bandgap of the films monotonically increased from about 3.28 to 3.44 eV as the Si concentration was increased from 0 to 6.5 atomic %.

To explain the observed increase of the bandgap of ZnO thin films with increasing Si concentration we propose that this is due to the competing effects of heavy doping induced Burstein-Moss (BM) shift [147, 148] and the bandgap narrowing, reported earlier by Jain and Roulston [30]. The BM shift in the Si doped ZnO films is inevitable because of the observed increase in the electron density as shown in figure 3.4. To calculate the BM shift (ΔE_{BM}) and the resulting bandgap (E_{BM}) we used the standard expressions as follows [147, 148]:

$$\Delta E_{BM} = \frac{h^2}{8\pi^2}(3\pi^2 n)^{2/3}\left(\frac{1}{m_e^*} + \frac{1}{m_h^*}\right) \tag{3.1}$$

$$E_{BM} = E_0 + \Delta E_{BM} \tag{3.2}$$

In equation 3.1, while h and π are the usual constants, n is the electron density measured at different Si concentrations as shown in figure 3.4, the effective mass of electrons (m_e^*) was taken to be $0.28m_e$ and that of the holes (m_h^*), $0.59m_e$ in terms of the free electron mass (m_e) from the references [41, 55, 91]. In equation 3.2, E_0 is the bandgap of undoped stoichiometric ZnO taken to be ≈ 3.38 eV at room temperature [2, 91, 138]. Variation in the bandgap of ZnO films with increasing carrier concentration *i.e.* at increasing Si concentration, calculated form the above formula of the BM shift is shown in figure 3.7 by the blue dotted curve. The experimental values of the bandgap are shown by the filled squares in the same figure. As can be seen from the dotted curve and the experimental points, the bandgap obtained from the BM shift alone is higher and it increases much faster than that observed experimentally. Thus the BM shift alone can not explain the observed bandgap variation with the carrier concentration. In view of the above finding it is imperative to look for other possibilities, which result in the decrease of the bandgap with increasing carrier concentration to compensate for the values calculated from the BM shift alone. We applied the concept of bandgap narrowing developed for heavily doped semiconductors [91, 149–151], which was later treated extensively by Jain and Roulston to deduce an expression applicable to any heavily doped semiconductor [30]. The bandgap narrowing is known to result from many body interactions between the carriers and interactions between carriers and impurities [30, 91, 149–151]. In n-type semiconductors, beyond a certain doping concentration, semiconductor to metal transition occurs which is marked by the merging of the conduction band and the donor band [31, 55]. The corresponding carrier concentration is known as Mott critical density. For ZnO, the critical density has been experimentally found to vary between ≈ 5.4 - 8.4×10^{19} cm^{-3} [55]. At or above this critical density, which indeed is the scenario in the present case, many body interactions become effective.

To calculate the bandgap of Si doped ZnO as a function of carrier concentration due to bandgap narrowing we used the formulation reported by Jain and Roulston [30]. The same formulation has also been used earlier by Lu *et al.* for Al doped ZnO thin films [55]. According to this formalism, there are four effects causing the bandgap narrowing (i) shift of the conduction band edge due to exchange interaction amongst the electrons (ΔE_{ex}), (ii) shift of the valence band edge due to electron-hole interaction (ΔE_{eh}), (iii) shift of conduction band edge due to electron-impurity interaction (ΔE_{ei}) and (iii) shift of the valence band edge due to hole-impurity interaction (ΔE_{hi}). All the shifts are into the gap and the total energy shift (ΔE_{BGN}) i.e. bandgap narrowing is given by,

$$\Delta E_{BGN} = \Delta E_{ex} + \Delta E_{eh} + \Delta E_{ei} + \Delta E_{hi} \tag{3.3}$$

As calculated by Jain and Roulston [30] this expression simplifies to the following formula under the assumption that electron concentration is equal to the donor concentration,

$$\Delta E_{BGN} = 1.83\frac{\Lambda R}{N_b^{1/3} r_s} + \frac{0.95R}{r_s^{3/4}} + \left[1 + \frac{m_{min}}{m_{maj}}\right]\frac{1.57R}{N_b r_s^{3/2}} \tag{3.4}$$

Here Λ is the correction factor due to anisotropy in the conduction band. It usually is in the range from 0.75 to 1 [151–153]. In our calculations the effect of band anisotropy was ignored by assuming $\Lambda = 1$ in accordance with available literatures [55, 152, 153]. N_b is the number of equivalent valleys in the conduction band for n-type semiconductors and its value can be taken to be 1 [55]. R is given by,

$$R = \frac{13.6m_r}{\epsilon_r^2}\text{eV} \tag{3.5}$$

where m_r is the ratio of the effective mass of electrons in the conduction band and the free electron mass. The value of m_r has been taken to be 0.28 [1, 41, 55]. ϵ_r is the dielectric constant of Si doped ZnO. Since its value is unavailable, we have assumed it to be equal to the dielectric constant of pure ZnO films. This assumption is valid because the doping concentration is rather small. The value of ϵ_r for pure ZnO is 8.65 [55]. r_s is given by,

$$r_s = \frac{r_a}{a} \tag{3.6}$$

where r_a is half the average distance between the donor atoms and a is the effective Bohr radius of the donors. The values of r_a and a are calculated using the formulation from [30], which are:

$$r_a = \left(\frac{3}{4\pi N}\right)^{1/3} \tag{3.7}$$

$$a = \frac{0.53\epsilon_r}{m_r} \times 10^{-8}\text{cm} \tag{3.8}$$

Here N is the donor concentration. As discussed earlier, each Si donor gives one electron to the ZnO lattice. Moreover other donors such as Zn interstitials (Zn_i) and oxygen vacancies (V_O) are also primarily singly ionized so that N is equal to the electron concentration.

m_{maj} and m_{min} are majority carrier (electrons) and minority carrier (holes) effective masses respectively. We have used equation 3.4 for calculating the bandgap narrowing under the aforesaid assumptions. The bandgap of Si doped ZnO thin films considering only bandgap narrowing is given by,

$$E_{BGN} = E_0 - \Delta E_{BGN} \tag{3.9}$$

The variation of E_{BGN} with carrier concentration is shown by the red dashed curve in figure 3.7. The total bandgap (E_g) considering both the BM shift as well as bandgap narrowing is given by,

$$E_g = E_0 + \Delta E_{BM} - \Delta E_{BGN} \tag{3.10}$$

The solid line curve in figure 3.7 shows the variation of the theoretical bandgap as calculated from 3.10 with carrier concentration. As mentioned earlier, the bandgap of the films measured from the transmission spectra are shown by filled squares. Now it can be seen that the experimentally observed bandgap variation of Si doped ZnO thin films matches quite well with those calculated from the theory.

Room temperature photoluminescence was studied for all the films, essentially to see the bandgap and other luminescence characteristics. The PL spectra of these films are shown in figure 3.8. As can be seen, the intensity of the PL peak was found to decrease with increasing Si concentration in the films. This was due to deterioration in the crystalline quality of the films and enhanced electron-electron scattering with increase in carrier density observed with increasing Si concentration. This is in line with the observation made by HRXRD studies which indicated deterioration in the crystalline quality of ZnO with increasing Si doping. The FWHM of the PL peak was found to increase from $\approx$ 144 to 198 meV. This increase in the FWHM of PL peak can be attributed to the increasing disorder and the resulting potential fluctuation due to random distribution of the impurity ions [62, 154] *i.e.*, Si in ZnO. All the films also showed Stokes shift of the bandgap measured from PL as compared to the absorption data. The Stokes shift was found to increase from $\approx$ 27 to 187 meV with increasing Si doping. The reason of this Stokes shift in Si

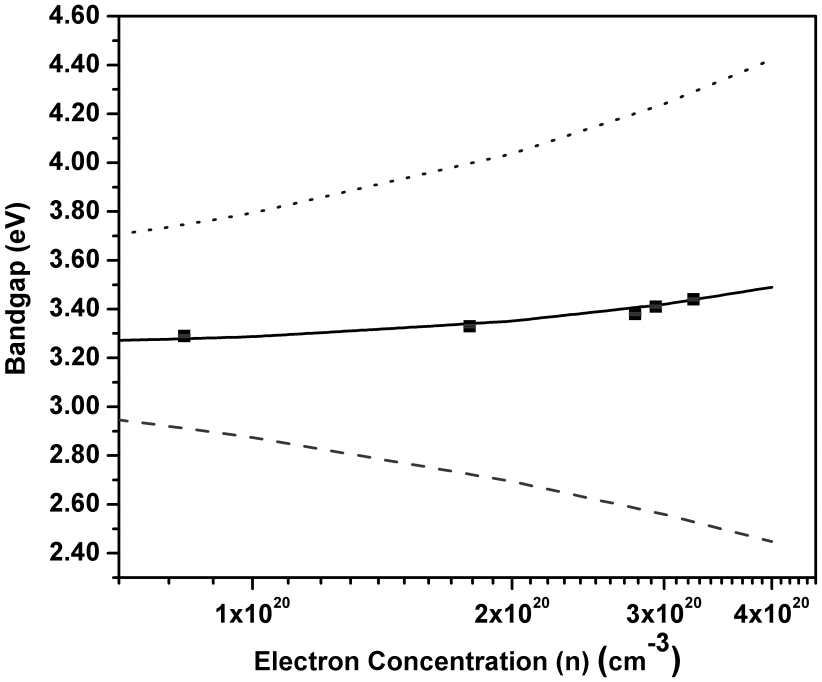

Figure 3.7: Variation of ZnO bandgap with carrier concentration. Filled squares are the experimental data points measured from the transmission spectra. The upper dotted curve is theoretical bandgap calculated considering only BM shift, whereas thelower dashed red curve is bandgap calculated using only bandgap narrowing effect. The continuous line curve in the figure is the bandgap calculated considering collective effect of both.

doped ZnO is not very well understood; however in literature for heavily doped n-type ZnO, it has been attributed to the different natures of absorptive and emissive optical transitions. In n-type ZnO the absorptive optical transition is from valance band to Fermi level whereas the emissive transition is from the donor band to the valence band. Because of this difference the luminescence peak is red shifted i.e. Stokes shifted as compared to the absorption edge [62]. The values of the Stokes shifts in our samples compare quite well with those found in Ga doped ZnO films (22 meV to 396 meV) as reported by Makino *et al.* [62] for the corresponding electron concentrations up to $\approx 3 \times 10^{20}$ cm^{-3}.

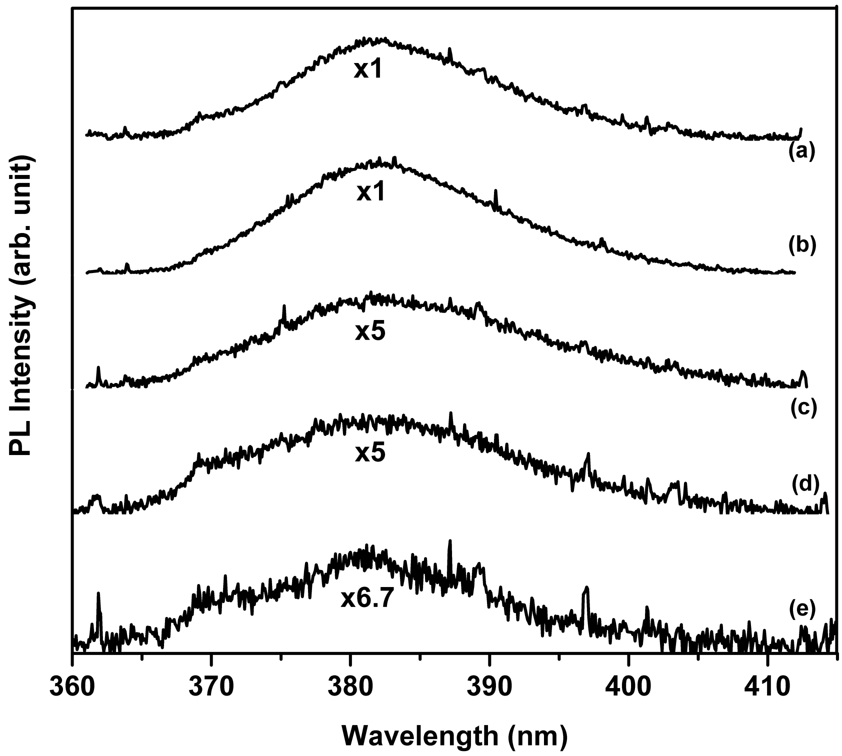

Figure 3.8: Room temperature photoluminescence spectra of (a) ZnO and Si doped ZnO thin films with different Si concentrations of (b) 0.5%, (c) 1.1%, (d) 4.1% and (e) 6.5%.

3.5 Conclusion

In conclusion, highly transparent and c-axis oriented Si doped ZnO films have been grown by sequential pulsed laser deposition on alumina substrates. Resistivity of these films was found to decrease rapidly to a minimum and then increase slightly with increasing Si doping. This decrease of resistivity was due to enhancement in the carrier density and associated semiconductor to metal transition due to Si doping. Blue shift in the ZnO bandgap due to Si doping was explained collectively considering the BM blue shift due to Fermi level being pushed into the conduction band and the bandgap narrowing caused by disorder. The optical transmission spectra also showed that with increasing Si concentration the steepness of band edges decreased due to band tailing caused by heavy doping induced disorder. Further, room temperature near band edge photoluminescence was observed in all the films, the FWHM of which increased with increasing Si doping due to disorder induced potential fluctuations. Thus in this chapter we have shown that the disorder caused by Si doping brings about significant changes in the electrical and optical properties of ZnO thin films. These changes include semiconductor to metal transition, bandgap narrowing, PL peak broadening and band tailing.

Chapter 4

Effects of disorder on transport properties of Si doped ZnO thin films at low temperatures

One prominent feature of disorder in degenerate or metal like semiconductor thin films is quantum corrections to conductivity, which can be observed in the low temperature transport properties of such films [31, 32, 35]. Multiple elastic scattering of the charge carriers from the defects reduces the transport mean free path to such an extent that it becomes comparable to the Fermi wavelength. In such cases the wave nature of the carriers become important and the interference of the electron waves change the transport properties at low temperature [57, 58]. This is known as the quantum corrections to conductivity as has been discussed in chapter 1 [31,32]. If the strength of disorder is further enhanced, the carriers may get strongly localized leading to a metal to insulator transition [155–157]. As has been discussed in chapter 3, the Si doped ZnO (SZO) thin films are metal like or degenerate due to the fact that the Si atoms acts as shallow donor in ZnO. The Fermi level lies in the conduction band. It has been also shown that Si atoms create substantial disorder in the films, which scatters the conduction band electrons randomly. Therefore, it would be interesting to study the low temperature transport properties of such degenerate Si doped ZnO thin films to probe the signature of quantum effects in the transport properties that may be brought about by disorder.

In this chapter we present the results of our studies on the low temperature transport properties of Si doped degenerate ZnO thin films. In the section 4.1 we present the details of our studies on SZO thin films with same thickness but varying Si concentration. And in section 4.2 we present the results of our studies on SZO thin films with fixed Si concentration but varying thickness. Interestingly the results in the two cases are different.

4.1 Quantum corrections to conductivity in Si doped ZnO thin films with varying Si concentration

The temperature dependent transport properties of ZnO thin films doped with Si in the concentration range from 0.5 to 5.8 % has been studied in the temperature range from 4.2 to 300 K. Although the films were degenerately doped with electron concentration greater than the Mott's critical density in ZnO [55], it was found that quantum corrections to conductivity produced a negative temperature coefficient of resistivity (TCR). Detailed description of the experimental methods and the obtained results are discussed in this section.

4.1.1 Experimental methods

The Si doped ZnO films with thickness of $\approx$ 230 nm were grown on c-axis alumina substrates by sequential pulsed laser deposition (PLD) using two separate targets of Si and ZnO [38, 119]. By adjusting the ablation durations of Si and ZnO, the Si composition in the films were varied in the range from 0.5 to 5.8%. The growth was done at 400^0C using a KrF excimer laser having 20 ns pulse duration at 10 Hz repetition rate. Laser fluence was maintained at ≈ 1.0 J-cm^{-2}. The PLD chamber was evacuated to achieve a base pressure of 5×10^{-6} mbar and then it was filled with oxygen up to a pressure of 1×10^{-4} mbar prior to deposition. Indium contacts were made on the films to make Ohmic contacts for electrical measurements. Temperature dependent electrical measurements of the SZO films were carried out in four-probe van der Pauw geometry using lock-in amplifier in the temperature range from 4.2 to 300 K. The magnetic field of ≈ 0.5 T was used for Hall as well as magnetoresistance measurements. The concentration of Si in the films, including the depth profile, were measured by using a commercial time of flight secondary ion mass spectrometer (TOF-SIMS), with the analysis beam of Bi$^+$ and sputtering beam of O.

4.1.2 Compositional characteristics

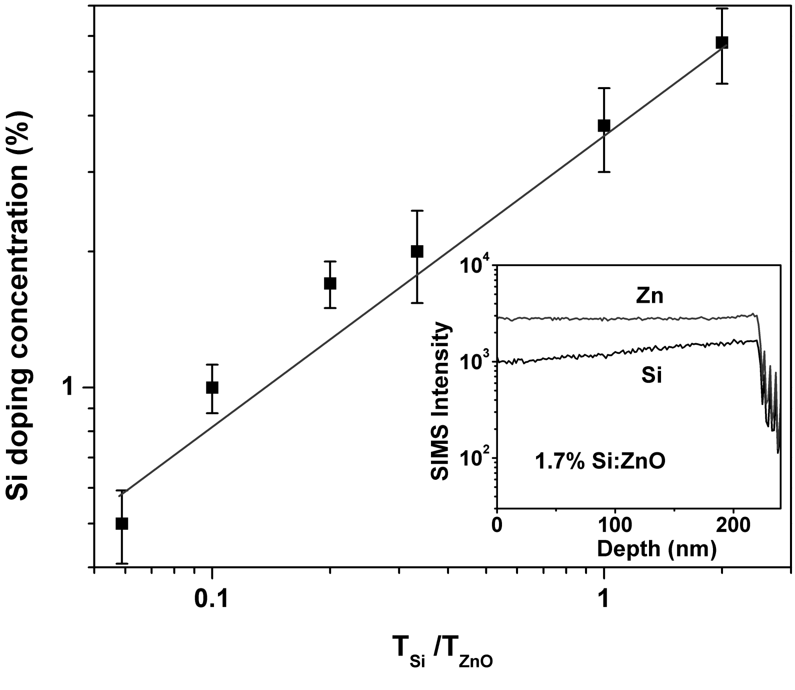

Figure 4.1: Si doping concentration as a function of ratio of ablation duration of Si and ZnO targets (T_{Si}/T_{ZnO}) as measured by TOF-SIMS. Inset shows typical SIMS depth profiles for ≈ 1.7% Si doped ZnO film.

From TOF-SIMS measurements, it was found that Si concentration in the $Si_xZn_{1-x}O$ films increased with increase in the ratio of ablation durations of Si and ZnO targets (T_{Si}/T_{ZnO}) as shown in figure 4.1. This proves the usefulness of sequential pulsed laser deposition for the growth of doped ZnO films. The inset shows the SIMS depth profiles of the $\approx$ 1.7% Si doped ZnO film. It is evident that although the concentration of Zn is almost constant throughout the film thickness, the Si concentration slightly varies with depth. This may be due to non-uniform ablation of the single crystalline Si target with time. At the start of the deposition the ablation rate was higher, however as time progressed the ablation rate of Si target decreased due to deterioration of the target surface.

4.1.3 Electrical characteristics and quantum corrections to conductivity

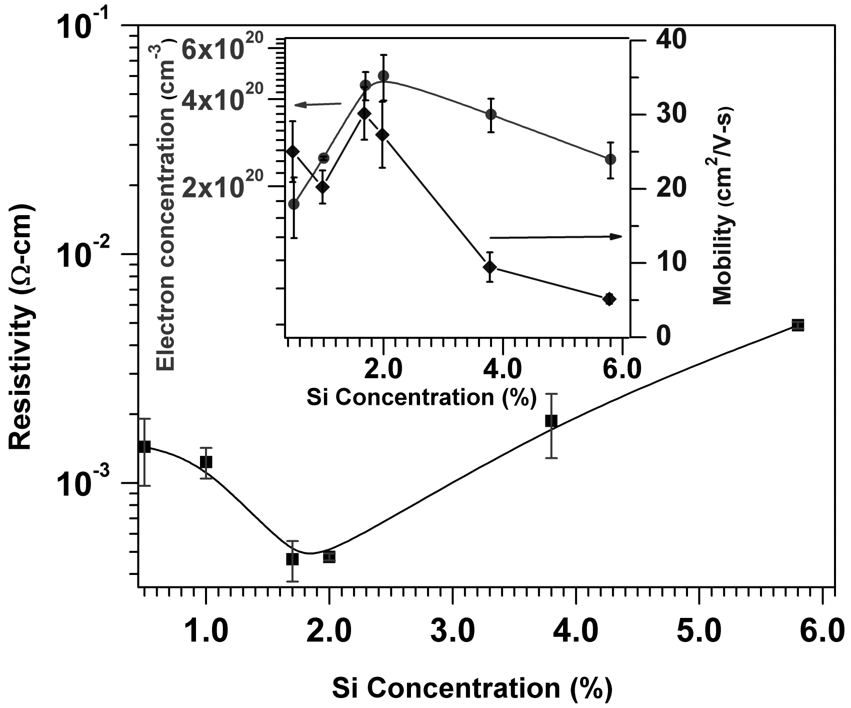

Figure 4.2: Variation of resistivity of Si doped ZnO films grown by sequential PLD as a function of Si doping concentrations. Inset shows corresponding variation of electron concentration and mobility.

Figure 4.2 shows the resistivity of the Si doped ZnO thin films as a function of Si concentration. The resistivity was found to first decrease from $\approx 1.4 \times 10^{-3}$ to $\approx 4.6 \times 10^{-4}$ ohm-cm as the Si concentration was increased from 0.5 to 1.7% and then it increased to $\approx 5.0 \times 10^{-3}$ ohm-cm with further increase in Si doping concentrations. This observation was similar to what we discussed in the last chapter. The inset of figure 4.2 shows the variation of electron concentration (n) and mobility (μ) as a function of Si concentration. With increasing Si concentration from $\approx$ 0.5 to 2.0%, the electron density initially increased from $\approx 1.7 \times 10^{20}$ to $\approx 4.8 \times 10^{20}$ cm^{-3}. As discussed in chapter 3, the increase in electron concentration is because of the fact that Si acts as a donor in ZnO [6, 142]. However on further increasing the Si doping to $\approx$ 5.8 %, the electron concentration gradually decreased to $\approx 2.5 \times 10^{20}$ cm^{-3}. The reason for the decrease in electron concentration at higher Si concentration may be trapping of electrons in acceptor type defects created due to heavy Si doping [86]. The point to be noted here is that the electron concentration in all the films was more than the Mott's critical density for ZnO [55], implying that all the films should be metallic in nature. The mobility on the other hand decreased from $\approx$ 30 to $\approx$ 5 cm^2/V-s on increasing the Si concentration from $\approx$ 0.5 to 5.8%, as a result of deteriorating crystalline quality of the films and enhanced carrier scattering [119]. This results are similar to the results presented for Si doped ZnO thin films in chapter 3.

The results of temperature dependent resistivity measurements of the films in the temperature range from 4.2 to 300 K are shown in figure 4.3. Whereas the 0.5% doped film showed negative TCR in the entire measurement temperature range, the 1.0, 1.7 and 2.0 % doped films showed transition from negative to positive TCR with increasing temperature. The two films with 3.8 and 5.8 % Si concentration, on the other hand, showed negative TCR in the entire temperature range. The reasons for some of the films showing transition in the TCR and others showing only negative TCR are discussed later. Further as seen in figure 4.3 the ratios of resistivity at 4.2 K to that at room temperature in all the films were not more than 1.2. This small increase in resistivity with decreasing temperature implied the absence of carrier activation or hopping phenomena [32]. Therefore as

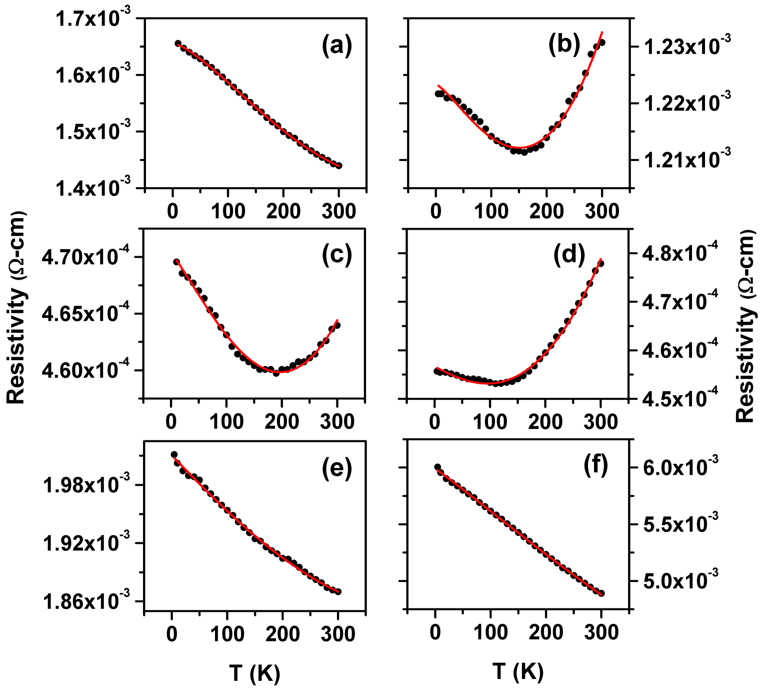

Figure 4.3: Temperature dependent resistivity (filled circles) of Si doped ZnO films with Si doping concentrations of (a) 0.5, (b) 1.0, (c) 1.7, (d) 2.0, (e) 3.8, and (f) 5.8 %. Continuous curves show the corresponding fittings of the data according to equation 4.4.

previously mentioned, the films are thought to be essentially metallic in nature. The direct evidence of absence of carrier activation came from the results of temperature dependent hall measurements. As shown in figure 4.4, the electron concentration for all the films was found to be temperature independent in the entire measurement temperature range from 4.2 to 300 K. This was expected as the films were degenerate with the Fermi level inside the conduction band [55, 119].

The negative TCR in metallic films could be seen when the Fermi wavelength λ_F given by $[2\pi/(3\pi^2 n)^{1/3}]$ becomes comparable to the electronic mean free path l $(h/\rho n e^2 \lambda_F)$ because of multiple scatterings, as pointed out by Ioffe and Regel [57, 158]. In such cases, the Boltzmann transport equation is no longer applicable and the interference of electron waves significantly alters the transport properties of metallic samples. It is known as the quantum correction to conductivity [32]. The values of l and λ_F for our samples are

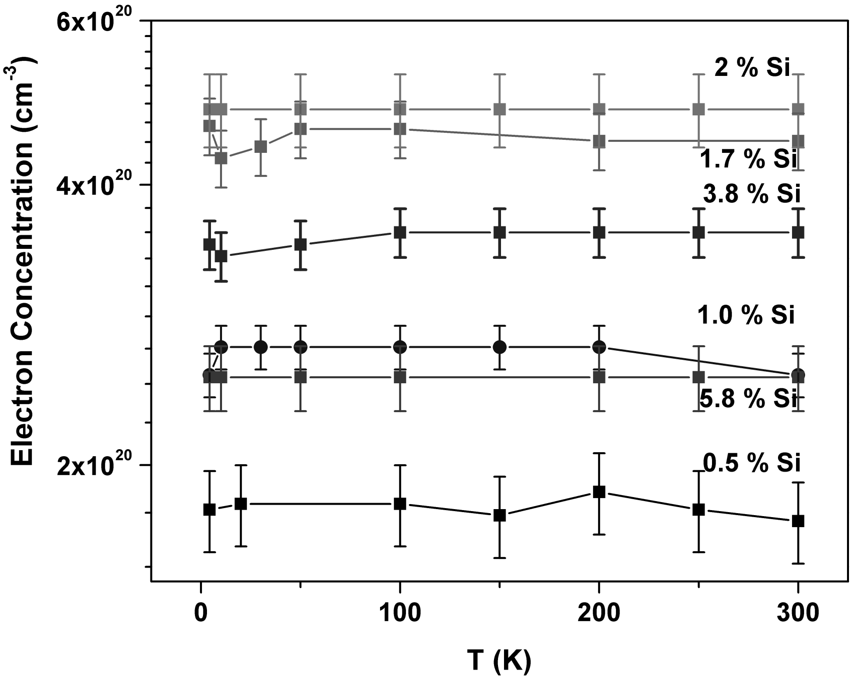

Figure 4.4: Variation of electron concentration (n) of Si doped ZnO films as a function of measurement temperatures.

shown in table 4.1. It can be seen that in all of them the mean free path is of the order of λ_F. Therefore we have to include quantum corrections to Boltzmann conductivity in our analysis of the temperature dependent transport properties of the films [89, 158]. The two main components responsible for quantum correction are the disorder induced weak localization and renormalized electron-electron interaction (REEI) effects [32, 33, 89]. The Si dopant atoms occupy lattice sites randomly in ZnO, thereby giving rise to disorder in the ZnO lattice. The electron waves get scattered coherently from these statistically distributed impurities along a closed path and interfere to give rise to the phenomenon of weak localization due to which the conductivity decreases. However, the phase breaking inelastic scatterings like electron-electron and electron-phonon scattering suppresses the effect of weak localization. The temperature dependence of resistivity due to weak localization comes into existence because of the temperature dependence of these phase-breaking inelastic scattering mechanisms [32]. On the other hand, the correction due to

Table 4.1: Values of mean free path and Fermi wavelength for Si doped ZnO films.

Si concentration (%)	λ_F (nm)	l (nm)
0.5	3.6	2.8
1.0	3.2	2.6
1.7	2.6	4.7
2.0	2.6	4.3
3.8	2.9	1.4
5.8	3.2	0.7

REEI arises because of Coulomb electron-electron interaction renormalized by electron interference effects [32, 33, 89]. The overall resistivity considering quantum corrections is written as [33],

$$\rho = \frac{1}{\sigma_0 + aT^{p/2} + bT^{1/2}} + cT^2 \tag{4.1}$$

Where σ_0 is residual conductivity, $aT^{p/2}$ describes the effect of weak localization where the parameter p is governed by the nature of inelastic collision and system dimensionality. It is 2 for electron-electron collision and 3 for electron-phonon interactions in three dimensions [33]. The term $bT^{1/2}$ gives the effect of REEI. The last term cT^2 is included to take into account the effects of high temperature scatterings [33].

It is known that a uniform magnetic field breaks the time-reversal symmetry and thereby destroys the phase coherence of the scattered electronic waves in a closed loop [32]. Therefore in presence of magnetic field the weak localization is suppressed and as a result the sample would show negative magnetoresistance [32, 158]. On the contrary the renormalized Coulomb electron-electron interaction is supposed to be relatively indifferent towards the presence of magnetic field [32, 58]. Figure 4.5 shows the magnetoresistance measured at a perpendicular magnetic field of ≈0.5 T as a function of temperature for three of the representative samples with Si concentrations of 0.5, 2.0 and 5.8 %. It can be seen that all of these samples showed negative magnetoresistance at low temperature, the magnitude of which decreased with increasing temperature, implying weak localization as the dominant contributing factor towards quantum correction. Further, in presence of REEI, the Hall coefficient or the electron concentration is expected to be temperature dependent according to the following formula [159],

$$\frac{\Delta R_H}{R_H} = -\frac{\Delta n}{n} = -2\frac{\Delta\sigma}{\sigma} \tag{4.2}$$

where R_H is the Hall coefficient, σ is the conductivity and Δ represents change in the corresponding quantity. However as shown in figure 4.4, the electron density (n) was practically constant with temperature for all the films. This implied the insignificance of REEI in the low temperature transport properties of Si doped ZnO thin films. Consequently in our calculations, the value of b was assumed to be 0.

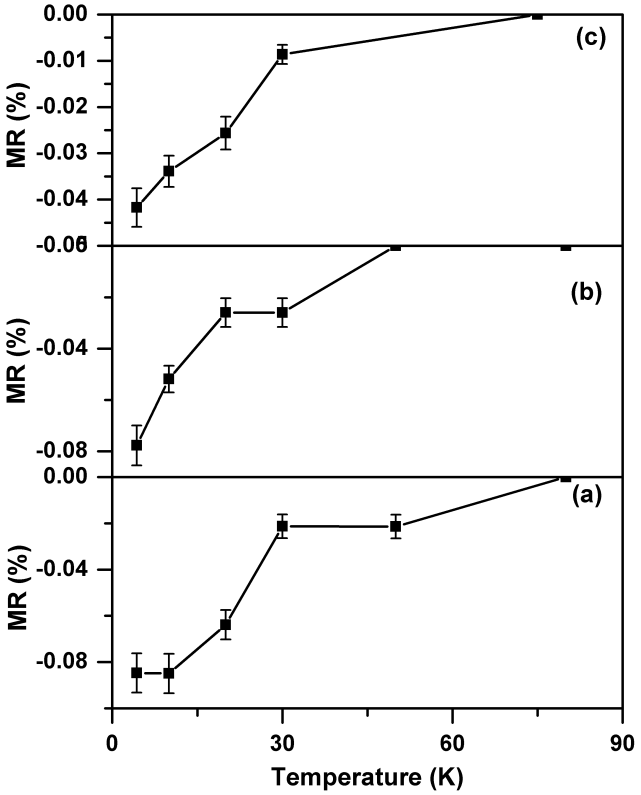

Figure 4.5: Variation of magnetoresistance (MR) of Si doped ZnO films with Si concentrations of (a) 0.5, (b) 2.0 and (c) 5.8 % at a field of 0.5T as a function of measurement temperature.

The correction term due to weak localization requires further attention. As can be seen from figure 4.3, the effect of quantum correction is prevalent in the SZO films even at fairly high temperature. Therefore both the electron-electron and electron-phonon dephasing mechanisms could be expected to be active in the films simultaneously and we have to consider their combined effects in the expression for corrections due to weak localization. The two dephasing mechanisms can be coupled using Matthiessen's rule [160],

$$\frac{1}{\tau_i} = \frac{1}{\tau_{e-e}} + \frac{1}{\tau_{e-ph}} \tag{4.3}$$

where τ_i is the effective inelastic scattering time and τ_{e-e} and τ_{e-ph} are the electron-electron and electron-phonon dephasing times respectively. Combing equation 4.3 with equation 4.1, taking into consideration the already mentioned dependencies of τ_{e-e} and τ_{e-ph} on temperature and using the value of b equal to zero, the expression for resistivity as a function of temperature can be written as [160],

$$\rho = \frac{1}{\sigma_0 + \sqrt{a_1 T^2 + a_2 T^3}} + cT^2 \tag{4.4}$$

where a_1 and a_2 are two parameters that decide the relative strengths of electron-electron and electron-phonon dephasing mechanisms respectively. With these, the results of quantitative fitting of the experimental resistivity curves by equation 4.4 are shown in figure 4.3 in red curves. As can be seen, the equation fits the experimental data very well. The values of the fitting parameters are listed in table 4.2. The relative strength of the electron-phonon dephasing mechanism with respect to that of the electron-electron dephasing mechanism (a_2/a_1) was found to decrease with increasing Si concentration. This observation was in accordance with reported results [160, 161]. As discussed by Schmid [162], the electron-phonon inelastic collision time increases with increasing concentration of impurities in the system. This lead to the observed reduction in the strength of electron-phonon dephasing mechanism with respect to that of the electron-electron dephasing mechanism. Moreover, the model of quantum corrections to conductivity is applicable under the condition that the correction terms are small in magnitude as compared to the residual conductivity [32]. To look into this requirement, we calculated the ratios of $\Delta\sigma/\sigma_0$, where $\Delta\sigma$ is the quantum correction term given by $\Delta\sigma_0 = \sqrt{a_1 T^2 + a_2 T^3}$. The calculated values of $\Delta\sigma/\sigma_0$ at 140 K for different Si concentrations are shown in table 4.2. From this table it is clear that $\Delta\sigma/\sigma_0$ was less than ≈0.05 for the films with transition from negative to positive TCR. For other films where there were no transition in TCR, it was little larger than this value but still smaller than ≈ 0.09. As discussed earlier the negative TCR at low temperature is caused by the electron interference effects. With the increase of temperature, the inelastic mean free path decreases and when it becomes smaller than the mean separation between the Si atoms, the interference effect is subdued and the films show normal metal like behavior dominated by high temperature scattering terms [139]. To understand the plausible reasons for some of the films showing transition in the TCR and others showing only negative TCR at different concentrations of Si we need to look into the functional dependence of transition temperature on the diffusion coefficient and doping density [139]. In the $Si_xZn_{1-x}O$ films with Si concentration of 0.5, 3.8 and 5.8 % the disorder and doping density were such that perhaps the inelastic scattering length was always greater than the mean separation between the Si atoms. As a result the temperature dependent resistivity behavior was dominated by weak localization effect which gave rise to the negative TCR in these films in the entire range of temperature. In the other films however the weak localization is dominating at low temperatures while at high temperatures the corresponding scattering terms of equation 4.4 would dominate. From table 4.2 it is also evident that the values of residual conductivity increased with increasing doping till the Si concentration of ≈ 2.0% in the films. It was due to enhancement in the electron density. Beyond this concentration of Si, the residual conductivity decreased due to reduction in electron density and mobility as already discussed in connection with figure 4.2.

Table 4.2: Values of the fitting parameters of equation 4.4 obtained from the fitting of the resistivity curves. The values of $\Delta\sigma/\sigma_0$ has been given for 140 K.

Si (%)	σ_0 [(ohm-cm)$^{-1}$]	a_1	a_2	c	$\Delta\sigma/\sigma_0$
0.5	603.7	6.9×10^{-3}	101.0×10^{-5}	15.7×10^{-10}	0.09
1.0	817.5	4.8×10^{-3}	23.1×10^{-5}	13.0×10^{-10}	0.03
1.7	2126.1	79.9×10^{-3}	270.0×10^{-5}	5.5×10^{-10}	0.04
2.0	2190.0	68.7×10^{-3}	225.0×10^{-5}	8.1×10^{-10}	0.04
3.8	497.4	22.1×10^{-3}	6.9×10^{-5}	9.2×10^{-10}	0.05
5.8	166.9	10.2×10^{-3}	3.0×10^{-5}	9.0×10^{-10}	0.09

4.2 Metal-insulator transition and dimensional crossover for weak localization in 2% Si doped ZnO thin films with varying thickness

In this section we present the results of our studies on the temperature dependent transport properties of $Si_{0.02}Zn_{0.98}O$ films with thickness varying in the range from 15 to 40 nm. In literature it has been reported that as the thicknesses of the metallic films are reduced, their sheet resistance increases and there is a possibility of metal to insulator transition with decreasing thickness if the electron mean free path eventually becomes smaller than the Fermi wavelength [57, 158]. From our studies we found that whereas the SZO film with thickness of $\approx$ 40 nm showed typical metallic behavior in temperature dependent resistivity measurements, the SZO film with thickness of $\approx$ 15 nm showed strongly localized behavior where the transport was dominated by hopping conduction. Therefore with decreasing thickness there was indeed a metal to insulator transition. In the intermediate thickness regime, negative temperature coefficient of resistivity was observed at low temperatures as a result of quantum corrections to Boltzmann conductivity. The detailed discussion about the experimental methods and results are presented in this section.

4.2.1 Experimental methods

$Si_{0.02}Zn_{0.98}O$ films were grown by pulsed laser deposition on (0001) alumina substrates at a temperature of 400^0C using a KrF excimer laser with 20 ns pulse duration and 10 Hz repetition rate. The laser fluence was maintained at $\approx$ 1.0 J-cm^{-2} and the oxygen partial pressure during the deposition was kept at 10^{-4} mbar. The thickness of the films were varied in the range from 15 to 40 nm, which were estimated from known growth rate of ZnO thin films under same condition as well as using thickness profiler. For electrical measurement indium contacts were made on the films, the linearity of which was confirmed from I-V measurements. Temperature dependent electrical measurements were carried out in the range from 4.2 to 300 K in four probe van der Pauw configuration. A magnetic field of $\approx$ 0.5 T was used for Hall as well as magnetoresistance measurements.

4.2.2 Thickness dependent metal to insulator transition

Figure 4.6 shows the results of temperature dependent sheet resistance measurements of the SZO films of different thickness. The sheet resistance increased continuously with decreasing thickness of the SZO films. For the film with thickness of about 40 nm, the room temperature sheet resistance was $\approx$ 0.14 kΩ and the films showed metallic behavior in the entire measurement temperature range. The room temperature electron concentration in this film was $\approx 2.4 \times 10^{20}$ cm^{-3}. The values of room temperature sheet resistance in the films with thickness of 30 and 20 nm were $\approx$ 1.0 and 6.3 kΩ respectively. Whereas the sheet resistance of the 30 nm film was almost temperature independent, the 20 nm thick film showed a negative temperature coefficient of resistivity (TCR). From Hall measurements it was found that the room temperature electron concentrations of the 30 and 20 nm films were respectively $\approx 1.6 \times 10^{20}$ and 8.7×10^{19} cm^{-3}. For the 20 nm film, the ratio of sheet resistances at 4.2 K to that at 300 K was $\approx$ 2. The negative TCR and small increase in resistivity with decreasing temperature in this film implied the presence of quantum corrections to conductivity [32, 158] as described later in detail. Finally in the film with thickness of about 15 nm, the room temperature sheet resistance was ≈ 240 kΩ which increased to ≈ 17.3 MΩ at 4.2 K, showing the possibility of strong localization of electrons [58, 158]. The electron concentration in this film could not be determined by Hall measurement. From the sheet resistance data presented in figure 4.6, it can be seen that the increase in sheet resistance of the films was much faster than the decrease in thickness of the film. This may imply the onset of a metal to insulator transition which is discussed in detail in the following paragraphs. The dashed horizontal line in figure 4.6 represents the quantum of resistance $h/e^2 = 25.8$ kΩ. It can be noted here that thickness dependent metal to insulator transition and superconducting to insulator transitions have been reported in literature for metallic thin films [163–165].

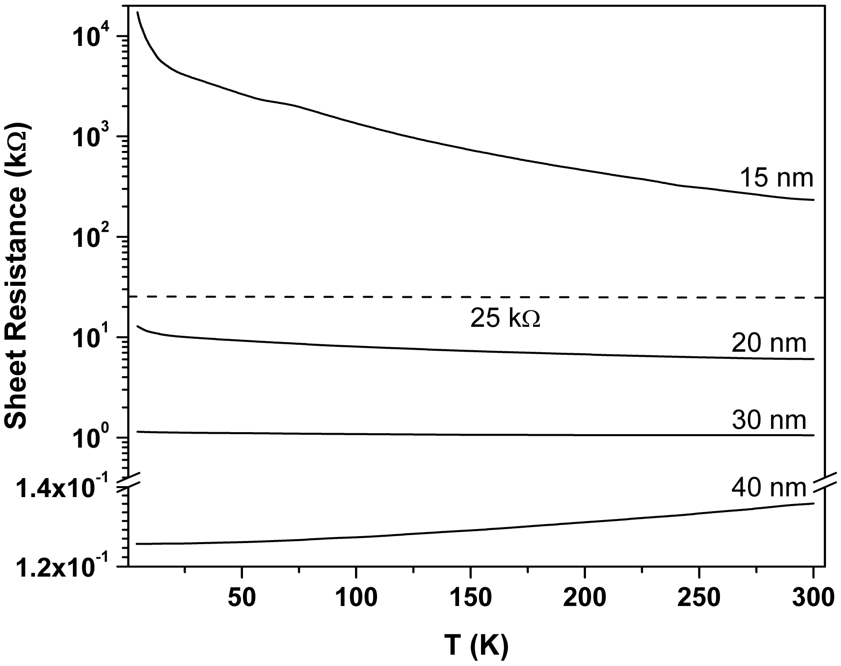

Figure 4.6: Sheet resistance as a function of temperature for Si doped ZnO films with different thickness.

As pointed out by Ioffe and Regel [57], when the Fermi wavelength (λ_F) becomes longer than the mean free path (l), the Drude model for the conductivity of metallic system breaks down and a metal to insulator transition is expected if $k_F l$ is close to unity, where k_F is the Fermi momentum. It is generally observed that for $k_F l >> 1$, the system shows normal metallic behavior and for $k_F l << 1$, the system is insulating *i.e.* strongly localized [158, 166]. Moreover as already discusses in the last section, when the Fermi wavelength becomes comparable to the mean free path, quantum effects due to interference of electron waves also become important [32]. It is known as quantum corrections to conductivity. This effect is most pronounced for intermediate values of $k_F l$ and the corresponding region is called the weakly localized region. Therefore on the basis of the value of $k_F l$, the films can be loosely classified into three categories - metallic, weakly localized, and insulating (or strongly localized) corresponding to high, intermediate or low values of $k_F l$ [32, 57, 158, 166]. The values of $k_F l$ can be deduced from the known values of sheet resistance and electron density, but for that it has to be ascertained whether the system is 2D or 3D. For a 2D system [32, 158],

$$k_F l = \frac{h/e^2}{R_s} \tag{4.5}$$

where R_s is the sheet resistance. On the contrary for a 3D system [1],

$$k_F l = \frac{3}{4}\frac{h/e^2}{R_s}\frac{\lambda_F}{t}. \tag{4.6}$$

Fermi wavelength $\lambda_F = 2(\pi/3n)^{1/3}$ where n is the electron concentration and t is the film thickness. These two formulas cross-over for $t = (3/4)\lambda_F$.

As shown in figure 4.7, the TCR for the film with thickness of ≈ 40 nm in the entire measurement temperature range was positive implying it's metallic state. The resistivity (ρ) of the film only decreased about ≈ 1.1 times from its room temperature value to a residual resistivity of $\approx 5.0 \times 10^{-4}$ ohm-cm, limited primarily by ionized impurity and grain boundary scatterings [167, 168]. At higher temperature the resistivity increased almost linearly with temperature. Below 100 K, however, it showed a typical quadratic dependence on temperature (shown in the inset of figure 4.7). These behaviors are consistent with reported results for degenerately doped bulk or 3D transparent conducting

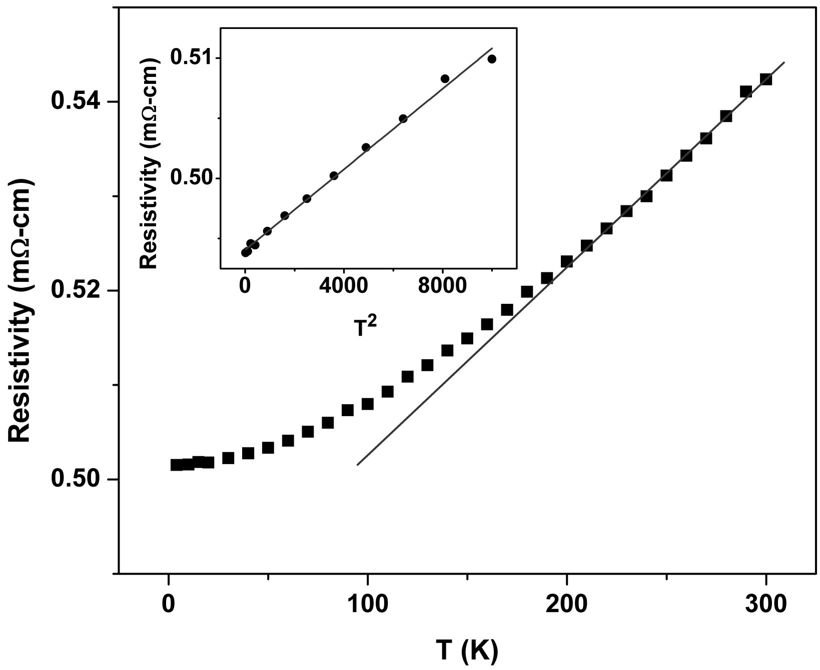

Figure 4.7: Resistivity as a function of temperature for Si doped ZnO film with thickness of 40 nm. Inset shows resistivity as a function of square of temperature.

oxide (TCO) films [167, 168]. As mentioned earlier, the electron density in the film was $\approx 2.4\times10^{20}$ cm^{-3}. Therefore the values of λ_F and $k_F l$ calculated as per equation 4.6 would be $\approx$ 3.2 nm and $\approx$11 respectively, which are consistent with 3D metallic film.

For the film with thickness of $\approx$ 15 nm, electron concentration could not be determined by Hall measurement plausibly due to very low electron mobility. As the room temperature sheet resistance of this film increased by more than $\approx$1700 times as compared to the film with thickness of $\approx$ 40 nm (i.e. decrease of thickness by only $\approx$ 3 times), the crystalline quality of the film must have deteriorated drastically that would result in lower mean free path and mobility. If it is assumed that the electron density in this film was same as that in the film with thickness of $\approx$ 20 nm, the value of Fermi wavelength comes out to be $\approx$ 4.6 nm which is much smaller than the film thickness. Therefore this film was also 3D in nature and using equation 4.6, the value of $k_F l$ could be calculated to be $\approx$ 0.02 and

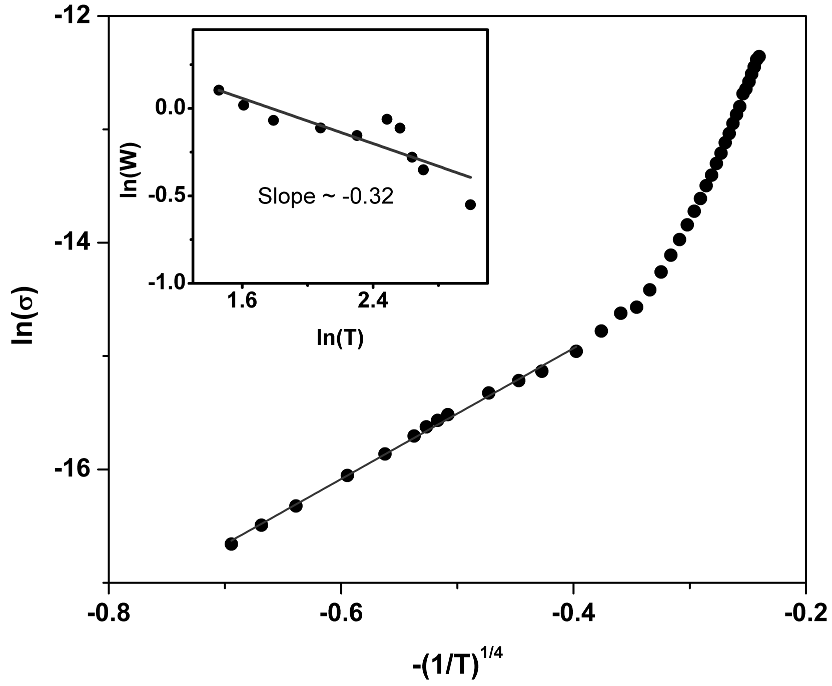

Figure 4.8: Logarithm of sheet conductance (σ) as a function of $(1/T)^{1/4}$ for the film with thickness of $\approx$ 15 nm. Inset shows corresponding log-log plot of reduced activation energy (W) as a function of temperature (T).

0.003 respectively at 300 and 4.2 K. As a consequence this film could be expected to show insulating or strongly localized behavior. Inset of figure 4.7 shows the logarithmic plot of reduced activation energy ($W = \frac{\partial \ln \sigma}{\partial \ln T}$) with temperature (T) for this film, following the scheme of Zabrodsky *et. al.* [29]. Here σ represents sheet conductance. As is evident, at low temperature the slope is negative with a magnitude of $\approx$ 0.32, implying that the electrons are strongly localized and the conduction mechanism is variable range hopping (VRH) [166, 169]. In VRH mechanism, the sheet conductance (σ) is related to temperature by the following formula [32],

$$\sigma = C \exp[-(T_0/T)^{\alpha}] \tag{4.7}$$

Here T_0 and C are material dependent constants. For noninteracting d-dimensional system, the hopping exponent is given by $\alpha = \frac{1}{d+1}$ (Mott VRH) [1]. On the other hand if the electrons are interacting with each other the exponent happens to be $1/2$ (Efros-Shhklovskii VRH) [32]. The plot of $\ln(\sigma)$ as a function of $1/T^{1/4}$ is shown in figure 4.8. The linear fit of the data below 50 K implied good agreement with a 3D VRH mechanism. However, it can be stressed here that due to limited range of temperature of the fitted data it was difficult to precisely determine the hopping exponent. Comparable fit of the data below 50 K could also be obtained with $\alpha = 1/3$ and $\alpha = 1/2$. Since from earlier discussion it was found that the sample was indeed 3D, it would be appropriate to rule out $\alpha = 1/3$. At higher temperatures the value of $k_F l$ increased and the behavior of the $\ln(\sigma)$ vs. $1/T^{1/4}$ plot deviated from linear fit. It may be due to transition from a strongly localized regime to a weakly localized regime with increasing temperature [32]. The fact that the conductance at low temperature for this film was consistent with 3D VRH, implied a thickness driven metal to insulator transition from a 3D metallic state (for $\approx$ 40 nm SZO) to a 3D insulating state.

4.2.3 Dimensional crossover for weak localization

Now we turn our attention to the films in the intermediate thickness regime. These are the films with thicknesses of $\approx$ 20 and 30 nm for which the values of $k_F l$ at room temperature as calculated from equation 4.6 were 0.3 and 2.3 respectively. Among these, the sheet resistance was almost temperature independent (figure 4.6) for the 30 nm film. It might be due to the fact that the classical and quantum contributions to conductivity compensated each other completely as their TCR have opposite signs [32]. For the films with thickness lower than this, the TCR changed sign (it was negative for the film with higher thickness) and it is said that the intermediate or critical region is attained [32] where the quantum corrections due to electron interference effects become important in the low temperature transport properties. As already mentioned in section 4.1, there are two main components of quantum corrections. One is the result of self interference of electron waves along a closed loop. It is known as weak localization. The other is the result of inter electron interference renormalized by coulomb interaction [32, 58, 158]. While the former is expected to give rise to negative magnetoresistance, the later would be rather insensitive to the presence of a magnetic field [32, 58]. Moreover in case of inter electron interference the Hall coefficient is supposed to change with temperature [159, 160]. In this sample, however, the Hall coefficient was found to be practically temperature independent. The magnetoresistance (MR) of the 20 nm sample is shown as a function of temperature in the inset of figure 4.9. It is evident that the MR was negative and its magnitude decreased with increasing temperature. These two facts, namely - the temperature independent nature of the Hall coefficient and negative magnetoresistance imply that weak localization was the dominant contributing factor towards quantum correction in this film. The weak localization is considered to be 2D or 3D in nature depending on whether the inelastic scattering length (L_{in}) is longer or shorter than the film thickness respectively. In the 2D case, considering the quantum corrections due to weak localization, the expression for the conductivity (σ) can be written as [58, 158],

$$\sigma = \sigma_0 + p\frac{e^2}{\pi h}\ln(T/T'_0) \tag{4.8}$$

where σ_0 is the Drude conductivity, T is temperature and p is a parameter that depends on the nature of inelastic dephasing mechanism and system dimensionality. In 2D for electron-electron collision it is 1 and for electron-phonon collision it is 3 [158]. The constant T'_0 is related to the mean free path for elastic collision. Figure 4.9 depicts the sheet conductance as a function of $\ln(T)$ for the film with thickness of $\approx$ 20 nm in the temperature range from 4.2 to 40 K. As can be seen, the linear fitting of the data yielded a slope of about 1.2×10^{-5} S which is equal to the constant $e^2/\pi h$, implying that the value of p is 1 [158]. Therefore the electron-electron interaction was the dominant dephasing mechanism, at least at low temperature. At temperatures higher than 50 K, the conductivity did not vary linearly with $\ln(T)$. One possible reason for that might be the crossover

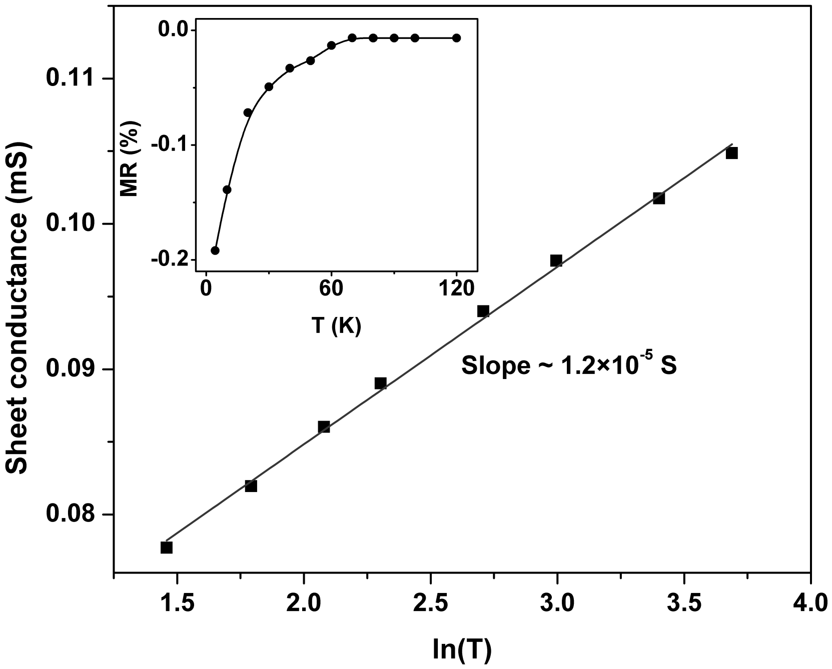

Figure 4.9: Sheet conductance as a function of logarithmic temperature for the 20 nm film. Inset shows variation of magnetoresistance as a function of temperature for the same film.

from 2D to 3D weak localization regime with increasing temperature [170]. Since the inelastic scattering length (L_{in}) decreases with increasing temperature, it is possible that at higher temperatures the value of L_{in} becomes less than the film thickness, causing this dimensional crossover from 2D to 3D weak localization [170]. For a 3D system, considering the quantum corrections due to weak localization, the expression for conductivity is [58, 159],

$$\sigma = \sigma_0 - \frac{e^2}{\pi^3 h}\left(\frac{1}{l} - \frac{1}{L_{in}}\right) \tag{4.9}$$

Here l is the mean free path for elastic collisions. Since the inelastic scattering length L_{in} is given by $L_{in} = AT^{-m/2}$, the expression for conductivity can be simplified as [159],

$$\sigma = C + \frac{e^2}{\pi^3 h}\frac{1}{A}T^{m/2} \tag{4.10}$$

where A and C are a constants. The exponent m depends on the nature of the dephasing mechanism. For electron-electron collisions in the dirty limit in 3D the value of m is 1.5 [171]. The plot of conductivity (σ) as a function of $T^{m/2}$ (with $m = 1.5$) is shown in figure 4.10. As can be seen the conductivity varied linearly with $T^{m/2}$ in the temperature range from ≈ 50 to 210 K implying the presence of 3D weak localization in the film in this temperature range. From the slope of the linear fit, an estimate of the inelastic collision length could be obtained using the fact that $L_{in} = AT^{-m/2}$. The values of L_{in} for various temperatures calculated using this 3D weak localization model is shown in the inset of figure 4.10. As can be seen at high temperature, the value of L_{in} was much smaller than the films thickness, justifying the 3D nature of the variation of conductivity with temperature. With decreasing temperature, the value of L_{in} gradually increased. If the data is extrapolated to 4.2 K, a value of ≈ 46 nm is obtained for L_{in}, which is more than the films thickness (≈ 20 nm). This fact when combined with the logarithmic temperature depen-

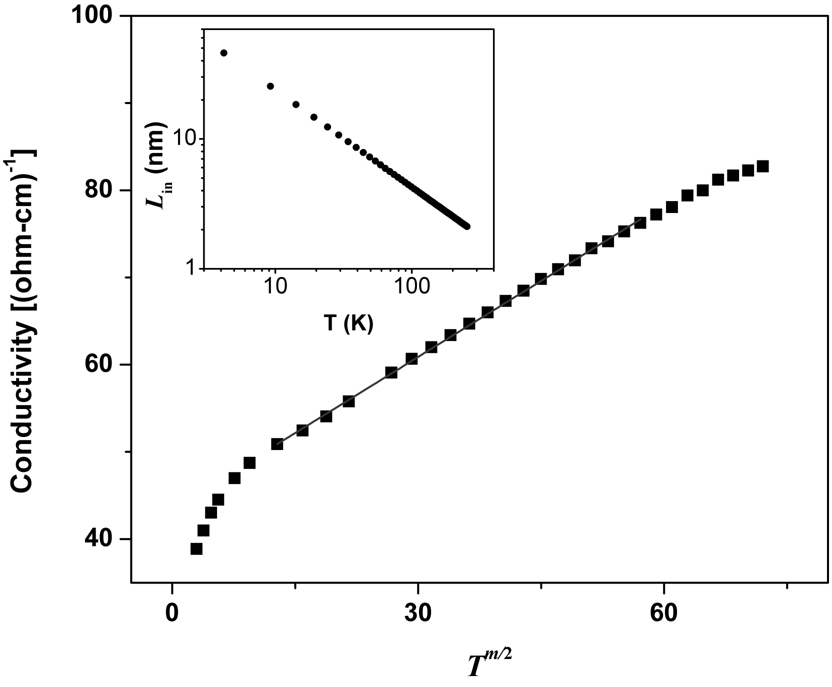

Figure 4.10: Conductivity as a function of $T^{m/2}$ with $m = 1.5$ for the film with thickness of ≈ 20 nm. Inset shows variation of inelastic scattering length (L_{in}) with temperature.

dence of sheet conductance at low temperatures implied that with decreasing temperature there was indeed a dimensional crossover for weak localization from 3D to 2D in the SZO film with thickness of $\approx$ 20 nm [170].

4.3 Conclusion

In conclusion, two sets of studies were carried out to study the effects of disorder on the low temperature transport properties of Si doped ZnO thin films. In the first set we have deposited Si doped ZnO thin films with Si concentration in the range from 0.5 to 5.8% using sequential pulsed laser deposition. The lowest resistivity obtained was $\approx 4.6 \times 10^{-4}$ ohm-cm at a Si concentration of $\approx 1.7\%$. Although the electron concentration in the films were higher than the Mott critical density, the temperature dependent resistivity measurements in the range from 300 to 4.2 K revealed negative TCR for the 0.5, 3.8 and 5.8% Si doped ZnO films in the entire measurement temperature range. The 1.0, 1.7 and 2.0% Si doped films showed a transition from negative to positive TCR with increasing temperature. The temperature independent nature of electron concentration together with the negative low field magnetoresistance found in the films at low temperatures pointed to weak localization as the dominant contributor towards negative TCR. A phenomenological fit of the temperature dependent resistivity data for all the films could be obtained by considering the quantum corrections to conductivity arising due to disorder induced weak localization effect, wherein both the influences of electron-electron and electron-phonon inelastic dephasing processes were included using Matthiessen's rule.

In case of the $Si_{0.02}Zn_{0.98}O$ films with fixed Si concentration of $\approx 2\%$ and thickness varying in the range from $\approx$ 15 to 40 nm grown by PLD on c-alumina substrates, the film with thickness of $\approx$ 40 nm showed typical metallic behavior in the temperature dependent sheet resistance measurements. On the other hand the film with thickness $\approx$15 nm showed a strongly localized behavior where the dominant mechanism of conduction at low temperature was 3D VRH. This implied a thickness driven metal to insulator transition in SZO films. The sheet resistance of the film with thickness of $\approx$ 30 nm was almost temperature independent implying it to be in the critical region. Finally the film with thickness of $\approx$ 20 nm showed a temperature dependent dimensional crossover from 3D to 2D weak localization with decreasing temperature due to decrease of inelastic scattering length with increasing temperature. The results of this chapter clearly demonstrate that the disorder caused by excessive Si doping dramatically changes the low temperature transport properties of Si doped ZnO thin films. It could also be seen that the effects of disorder on the transport properties of the SZO films depend not only on the Si concentration but on the film thickness as well. At lower thickness possibly the crystalline quality deteriorates drastically resulting in metal to insulator transition. From this study it therefore also emerged that there is a lower limit to the thickness of Si doped ZnO film for its application as transparent conducting electrode. These findings generated deeper insights about the effects of disorder on the low temperature transport properties of $Si_xZn_{1-x}O$ films.

Chapter 5

Effects of disorder on optical and electrical properties of MgZnO/ZnO heterostructures

Mg is a very important element for bandgap engineering of ZnO. If ZnO is alloyed with MgO, which has higher bandgap than ZnO, the bandgap of the resultant MgZnO alloy increases as per the Vegas law [172]. Since MgZnO alloy has lattice structure same as that of ZnO and higher bandgap, it is suitable for being used as the barrier material in ZnO quantum wells. Moreover, MgZnO and ZnO both crystallize in hexagonal wurtzite structure and have spontaneous polarization direction along the c-axis. If MgZnO/ZnO heterostructures are grown along the polar c-axis direction, accumulation of a large quantity of electrons occurs at the heterointerface due to strong built-in potential arising out of macroscopic polarization mismatch between the two layers of the heterostructures [173, 174]. This results in the formation of a 2DEG at the ZnO side of the heterointerface. MgZnO, therefore, has been extensively used as the barrier layer in MgZnO/ZnO heterostructures for the confinement of carriers in various applications like quantum well lasers, resonant-tunneling diodes, high electron mobility transistors, quantum Hall effect structures etc. [66, 175–177].

The solubility limit of MgO in MgO-ZnO binary system is reported to be only $\approx$ 4 mol% under thermal equilibrium condition [178]. However, much higher concentrations of Mg up to $\approx$ 40% are required for most practical applications which essentially lead to the formation of a metastable phase in MgZnO [178]. Moreover MgZnO/ZnO heterostructures are grown using various methodologies wherein for the good crystalline quality of MgZnO, growth temperatures are kept in the range of $\approx$ 600 to 800^0C [66, 177, 178]. A high growth temperature and the metastable nature of MgZnO alloys are known to cause significant diffusion of Mg across the interface from MgZnO to ZnO layer [178, 179]. Diffusion of Mg across the interface increases the band gap on the ZnO side of the interface resulting in the modification of optical properties. It also creates disorder on the ZnO layer which scatter 2DEG (electrons) randomly reducing their mean free path. If the mean free path under such conditions becomes smaller than or comparable to the Fermi wavelength, quantum interference effects would alter the low temperature transport properties of the 2DEG significantly [160]. In short the diffusion of Mg across the interface is expected to change the optical and electrical properties of the MgZnO/ZnO heterostructures.

To understand these effects we have carried out two sets of studies. In the first set, the photoluminescence (PL) properties of MgZnO/ZnO bilayer system with Mg composition of $\approx$ 30% were studied under different conditions of annealing to ascertain the effects of Mg diffusion on the PL properties of the heterostructures. In the second set, studies on electrical properties of the MgZnO/ZnO heterostructures were carried out to ascertain the effects of disorder on the transport properties of 2DEG confined at the ZnO side of the interface. Results from these experiments and numerical simulations are presented in this chapter.

5.1 Effects of Mg diffusion on optical properties of MgZnO/ZnO heterostructures

In this case the MgZnO/ZnO bilayers with Mg concentration of $\approx 30\%$ were annealed in the temperature range from 600 to 900^0C to allow diffusion of Mg from the MgZnO into ZnO layer. As a result of Mg diffusion the optical band gap on the ZnO side increased and that on the MgZnO side decreased till the annealing temperature of 800^0C. At the annealing temperature of 900^0C the two layers merged together to form a single layer with a uniform Mg composition. A theoretical model has also been developed and numerical simulations were carried out to correlate the PL spectra with the diffusion of Mg across the interface. Detailed description of the experimental methods and the obtained results are discussed in this section.

5.1.1 Experimental

$Mg_{0.3}Zn_{0.7}O$/ZnO bilayer films were grown on c-axis (0001) alumina substrates using pulsed laser deposition (PLD) with a KrF excimer laser. The bottom ZnO film ($\approx$ 80 nm thick) was grown at a substrate temperature of $\approx 750^0$C and then the top $Mg_{0.3}Zn_{0.7}O$ layer ($\approx$ 80 nm thick) was grown at 400^0C. Oxygen partial pressure in the PLD chamber was maintained at $\approx 10^{-5}$ mbar during the growth. The laser fluence was maintained at about 1 J/cm^2. The bilayers were subsequently annealed at different temperatures in the range of 600 to 900^0C for three hours under oxygen ambient. Diffusion of the constituent elements across $Mg_{0.3}Zn_{0.7}O$/ZnO interface was studied using secondary ion mass spectrometry (SIMS) depth profiling technique. A separate set of MgZnO films of thickness of $\approx$ 150 nm with Mg concentration in the range from 0 to $\approx 40\%$ were also grown using ceramic targets made by mixing ZnO and MgO powder in appropriate concentrations to study the variation of bandgap of MgZnO films as a function of Mg concentration which was required for the simulation performed on the photoluminescence spectra of the bilayers.

These films were grown at 400^0C and at 1×10^{-5} mbar partial pressure of oxygen on (0001) alumina substrates using same PLD. Optical properties of the as grown and annealed samples were studied at room temperature using optical absorption measurements using a standard UV-visible spectrophotometer and PL measurements with an excitation laser at 266 nm and a half meter long spectrometer coupled to a CCD.

5.1.2 Optical Properties of annealed MgZnO/ZnO heterostructures

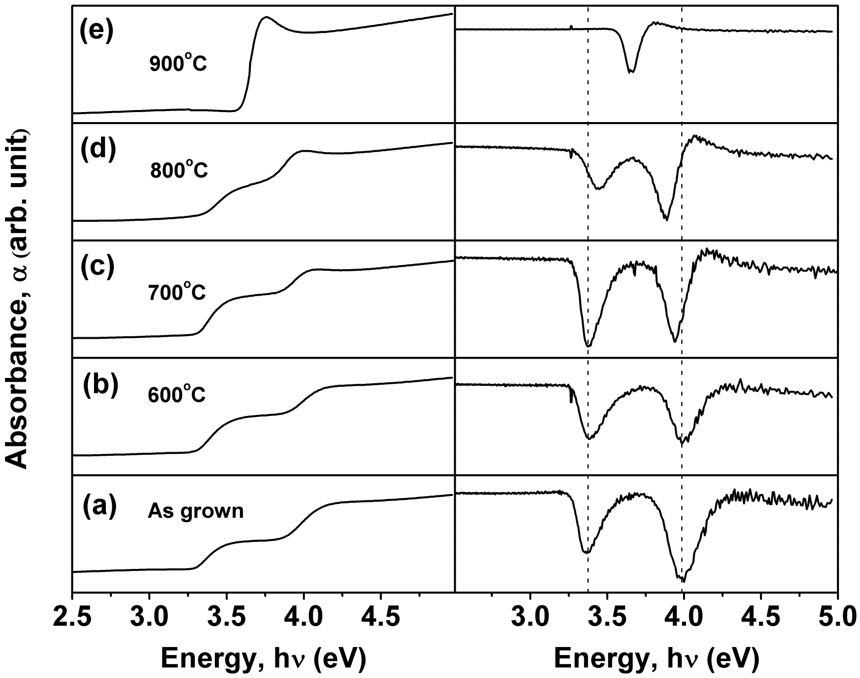

Figure 5.1: Absorption spectra (left) and its derivative (right) of (a) as grown and annealed $Mg_{0.3}Zn_{0.7}O$/ZnO bilayers at (b) 600^0C, (c) 700^0C, (d) 800^0C and (e) 900^0C.

The left panels of figure 5.1 show the absorption spectra of the as grown and annealed MgZnO/ZnO bilayers. Corresponding derivative absorption spectra are shown in the right panels of figure 5.1. The absorption spectrum of the as grown bilayer shows sharp absorption edges for the ZnO and MgZnO layers at $\approx$ 3.36 and 3.98 eV respectively as shown in figure 5.1a confirming the growth of MgZnO/ZnO heterostructure with well defined interface. Spectral position and sharpness of the absorption edges can be evaluated more precisely from the derivate absorption spectra. One does not see a noticeable change in the absorption edge of ZnO layer up to the annealing temperature of 700^0C as shown in figures 5.1b and 5.1c, implying no significant Mg diffusion across the interface occurs till this temperature. However, at the annealing temperature of 800^0C, absorption edge of ZnO layer blue-shifts and that of the MgZnO layer red-shifts as a result of the diffusion of Mg to the bottom ZnO layer (figure 5.1d). As the annealing temperature was further raised to 900^0C, the two layers are mixed completely, thus forming an MgZnO alloy with Mg concentration much less than $\approx 30\%$ as is apparent from the red-shifted single absorption edge of MgZnO layer (figure 5.1e).

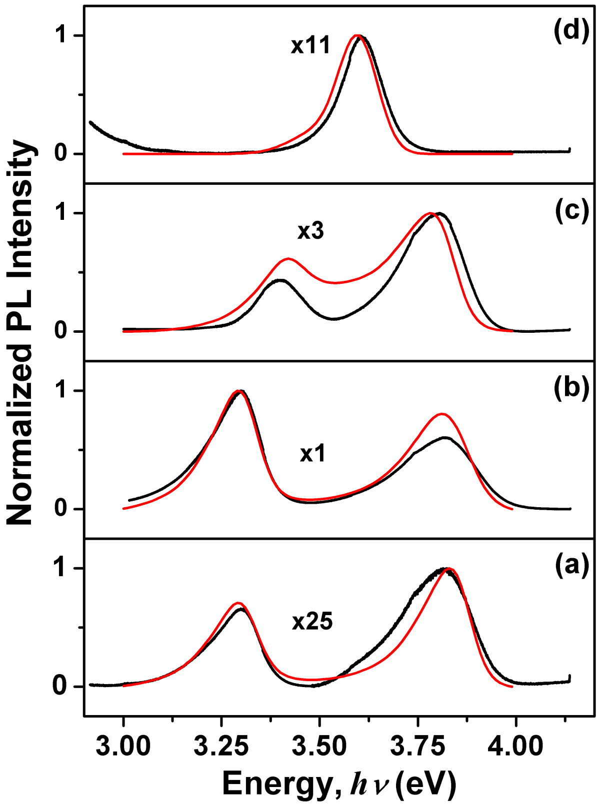

Figure 5.2: Experimental (black) and simulated (red) PL spectra of (a) as grown and annealed $Mg_{0.3}Zn_{0.7}O$/ZnO bilayers at (b) 700^0C, (c) 800^0C and (d) 900^0C.

PL spectra of the as grown and annealed MgZnO/ZnO bilayers are shown in figure 5.2.

The as grown bilayer shows two distinct peaks corresponding to the ZnO and MgZnO layers at ≈3.28 and ≈3.82 eV respectively (figure 5.2a). PL peak positions are maintained almost at the same energies at the annealing temperature of 700^0C (figure 5.2b). It is expected since there is no significant diffusion of Mg across the interface as shown by SIMS depth profile and absorption spectrum up to 700^0C. However, when the annealing temperature is raised to 800^0C, the PL peak corresponding to the ZnO layer blue-shifts to ≈ 3.40 eV while that of the MgZnO layer slightly red shifts to ≈ 3.80 eV due to Mg diffusion across the interface (figure 5.2c). For the heterostructure annealed at 900^0C, only a single PL peak is observed at ≈ 3.60 eV corresponding to a completely homogenized MgZnO layer as expected (figure 5.2d). Furthermore, the PL intensity of sample annealed at 700^0C is the maximum indicating an overall improvement in the layer quality due to annealing which is also ascertained by a more uniform depth profile in SIMS measurements (as shown in figure 5.3b) and the sharpness of derivative absorption spectrum (figure 5.1c).

5.1.3 SIMS depth profile of Mg distribution

More evidences about Mg inter-diffusion can be obtained from the SIMS depth profiles of the as grown and annealed bilayer samples that are shown in figure 5.3. For the as grown bilayer, the interface is sharp where Mg concentration decreases from ≈30% to less than 1% within a depth of < 20 nm at the interface as shown in figure 5.3a. The bilayer that was annealed at 700^0C also shows a similar Mg distribution with depth as depicted in figure 5.3b indicating no degradation of the interface. However, at the annealing temperature of 800^0C, significant Mg diffusion into the ZnO layer is apparent from figure 5.3c. Mg concentration decreases gradually from ≈ 25% to ≈ 4% over a depth of ≈ 100 nm, rendering a significant diffusion of Mg across the interface. Mg content in the top MgZnO layer is found to decrease from its initial value of ≈30% to 25% as a result of diffusion. Mg is present over the entire depth of the underlying ZnO layer thereby blue-shifting its

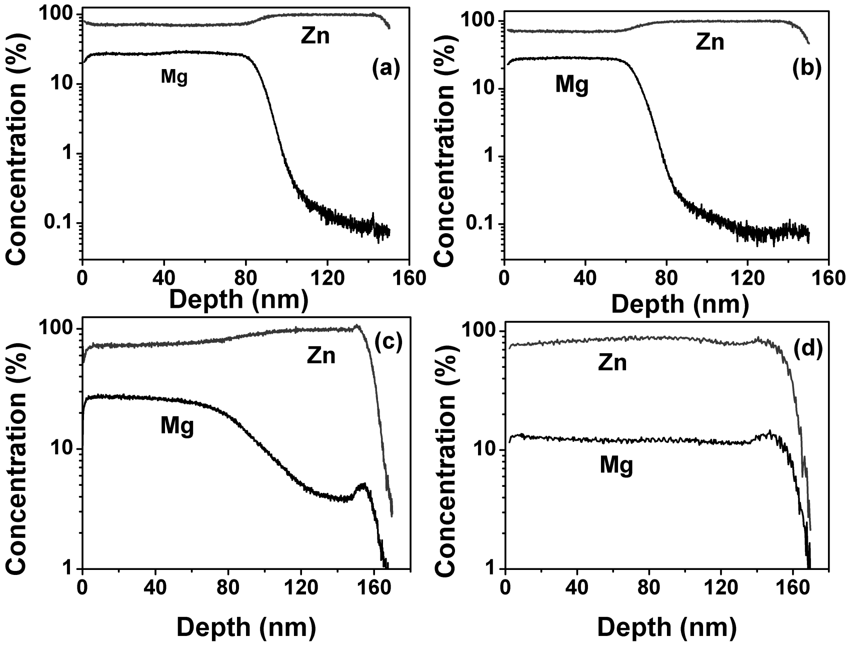

Figure 5.3: Variation of Mg and Zn concentration (measured by SIMS) as a function of depth for (a) as grown and annealed $Mg_{0.3}Zn_{0.7}O$/ZnO bilayers at (b) 700^0C, (c) 800^0C and (d) 900^0C. Thickness of the top MgZnO (as grown) layer in plot (b) was ≈ 60 nm due to unintentional variations in the growth rate.

band edge. When the annealing temperature was further raised to 900^0C, the bilayer gets homogenized to a single MgZnO layer with $\approx 13\%$ Mg distributed almost uniformly as shown in figure 5.3d. These results are in conformity with the absorption spectra of the samples.

5.1.4 Correlation of photoluminescence spectra with depth profile of Mg concentration

To theoretically correlate the PL spectra of the bilayers with the experimental Mg depth profiles as measured by SIMS, we proceeded as follows. First a relation describing the dependence of PL peak position on the Mg concentration (x) was needed. For that a set

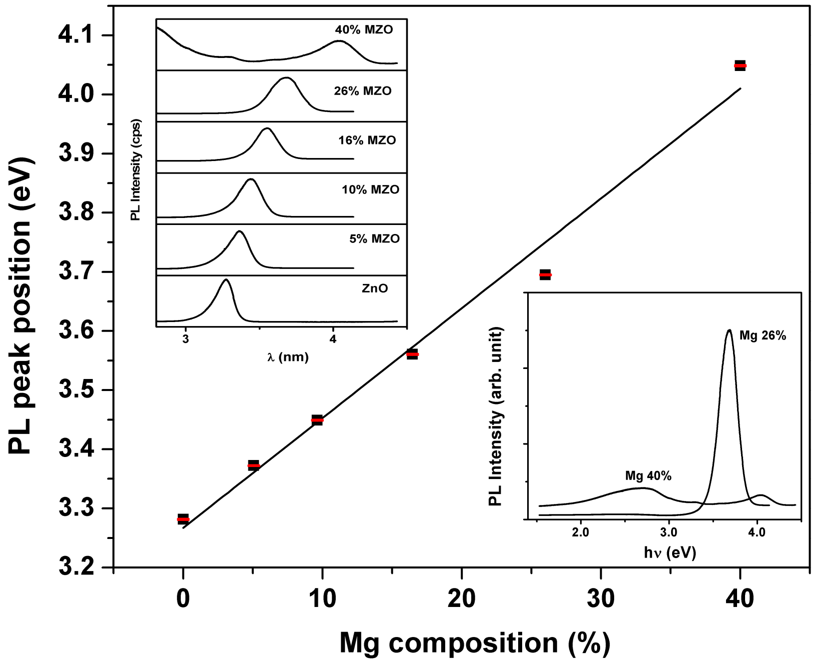

Figure 5.4: Variation of PL peak positions of $Mg_xZn_{1-x}O$ films as a function of x. Upper inset shows corresponding PL spectra of the films. Lower inset shows full range PL spectra for films with Mg concentrations of about 26 and 40 %.

of $Mg_xZn_{1-x}O$ films with varying x in the range from 0 to ≈ 0.4 were grown and their PL spectra were recorded. Figure 5.4 shows the PL peak positions of these $Mg_xZn_{1-x}O$ films as a function of Mg concentration (x), whereas the inset shows the corresponding PL spectra. PL peak position can be expressed as follows [172],

$$E_{PL}(x) = xE_{MgO} + (1 - x)E_{ZnO} - \delta x(1 - x) \tag{5.1}$$

where $E_{PL}(x)$ is the PL peak position of $Mg_xZn_{1-x}O$ film. E_{MgO} and E_{ZnO} are the bandgaps of MgO and ZnO which are taken respectively as 5.2 [180] and 3.28 eV in our calculations, and δ is known as the bowing parameter. The value of bowing parameter is found to be ≈ 0.18 eV by fitting the experimental PL peak positions using equation 5.1 (shown by black line in figure 5.4). It has been predicted by the density functional theory that the bandgap of $Mg_xZn_{1-x}O$ is a linear function of x with negligible bowing along with a slope of ≈ 2.5 [181]. In our case, the bowing parameter is small and the slope is ≈ 1.8 which is very close to the values reported by others [12, 181–183]. Moreover it can be mentioned here that with increasing Mg concentration from 0 to 40%, the FWHM of the PL peaks increased from 160 meV to $\approx$ 240 meV due to increasing inhomogeneity and the resulting random potential fluctuation in the films [184], which is a prominent signature of disorder. The lineshape of the PL spectra also changed with Mg concentrations. The suppression of longer wavelength tail at higher doping may be caused by the suppression of phonon replicas as the crystalline quality deteriorates with increasing Mg concentrations [184]. The emerging band at lower energies for the 40% Mg doped sample is attributed in literature to native defect related luminescence in MgZnO [185].

SIMS depth profiles give Mg concentration (x) in the film as a function of depth (y) from the film surface. We can divide the whole depth profile into many infinitesimally small elements dy at a distance y from the surface with constant Mg composition, each of which would give PL corresponding to its Mg concentration with peak positions given by equation 5.1. The contribution to the overall PL at the frequency ν due to this small element will be given by,

$$dI(\nu) = G(\nu, E_{PL})\, dy \tag{5.2}$$

where $G(\nu, E_{PL})$ is the PL line shape function for the element with PL peak position at E_{PL}. We approximate it, for our calculations, as the PL profile of pure ZnO thin films, found by fitting PL data of ZnO by three Gaussians and is given by,

$$G(\nu, E_{PL}) = \sum_{k=1,2,3} A_k \exp\left(-\frac{2(h\nu - E_{PL} + \Delta_k)^2}{\sigma_k^2}\right) \tag{5.3}$$

where $\sigma_1 = 0.074$ eV, $\sigma_2 = 0.12$ eV, $\sigma_3 = 0.21$ eV, $A_1 = 2.4$, $A_2 = 2.6$, $A_3 = 1.0$, $\Delta_1 = 0$, $\Delta_2 = 0.042$ eV and $\Delta_3 = 0.11$ eV. The line shape function $G(\nu, E_{PL})$ is a function of y via

E_{PL}. The overall PL profile of the heterostructures will then be given by,

$$I(\nu) = \int_0^t G(\nu, E_{PL})\, dy \tag{5.4}$$

where t is the total thickness of the sample. The integration was evaluated numerically using GNU scientific library [186] taking the SIMS depth profile data $x(y)$ as the input. The resultant PL spectra are plotted on figure 5.2 in red color. As can be seen, the agreement between the theory and experiment is reasonable with a slight discrepancy which is within experimental limitations. Further, the line shape function and luminescence efficiency depend on Mg concentration [187] and also on the annealing temperature, which has been ignored in these preliminary calculations.

5.2 Effects of disorder on electrical properties of 2DEG confined at MgZnO/ZnO interface

In this section we discuss the effects of electron interference on temperature dependent transport properties of two dimensional electron gas (2DEG) confined at the interface in polycrystalline MgZnO/ZnO heterostructures grown by pulsed laser deposition on c-alumina substrates. The Mg concentration in the MgZnO layer was varied from 16 to 40%. On increasing Mg concentration in the MgZnO layer, the sheet electron concentration was found to increase and the sheet resistance found to decrease. In addition the electron concentration and mobility were almost temperature independent in the range from 4.2 to 300 K, indicating the formation of 2DEG at the interface. The temperature dependent resistivity measurements showed a negative temperature coefficient of resistivity at low temperatures together with negative magnetoresistance. These were found to be caused by electron interference effects and the experimental data could be explained using the models of quantum corrections to conductivity. Detailed discussion of the experimental methods and the obtained results are given in this section.

5.2.1 Experimental

The $Mg_xZn_{1-x}O/ZnO$ heterostructures with Mg concentration (x) varying from 16 to 40% were grown on c-alumina substrates by pulsed laser deposition using a KrF Excimer laser operating at 10 Hz and appropriate ceramic targets. The fluence used was $\approx$ 1 J/cm^2 and oxygen partial pressure of 1×10^{-5} mbar maintained during the growth. First, about 80 nm thick film of ZnO was grown on alumina at a growth temperature of $\approx 750^0$C. Subsequent MgZnO layer of $\approx$ 50 nm thickness was grown at 400^0C. X-ray diffraction measurement was used to confirm c-axis oriented growth. Indium contacts were made on the films' surface for electrical measurements. To make sure the successful growth of the MgZnO/ZnO heterostructures we carried out photoabsorption measurements as well. The ohmic nature of the contacts was confirmed from the linearity of I-V curves. Resistivity and Hall measurements were carried out in the van der Pauw four-probe geometry. For doing temperature dependent resistivity measurements in the range from 4.4 to 300 K, the samples were mounted in a cryostat. Isothermal transverse magnetoresistance measurements were carried out in the magnetic field range of 0 to 8 T.

5.2.2 Structural and optical properties

Figure 5.5 shows the $\omega - 2\theta$ plot of the $Mg_xZn_{1-x}O/ZnO$ heterostructure with $x = 0.26$. It is evident from the figure that both the layers of the heterostructure are in c-axis oriented hexagonal wurtzite phase. The two peaks correspond to the ZnO and ZnMgO films respectively. The XRD peak corresponding to the ZnMgO layer is at slightly higher angle with respect to that of ZnO layer because of lower value of the lattice constant c.

The result of photoabsorption measurements on the $Mg_xZn_{1-x}O/ZnO$ samples is shown in figure 5.6. The blue, purple and the black curves respectively represent the photoabsorp-

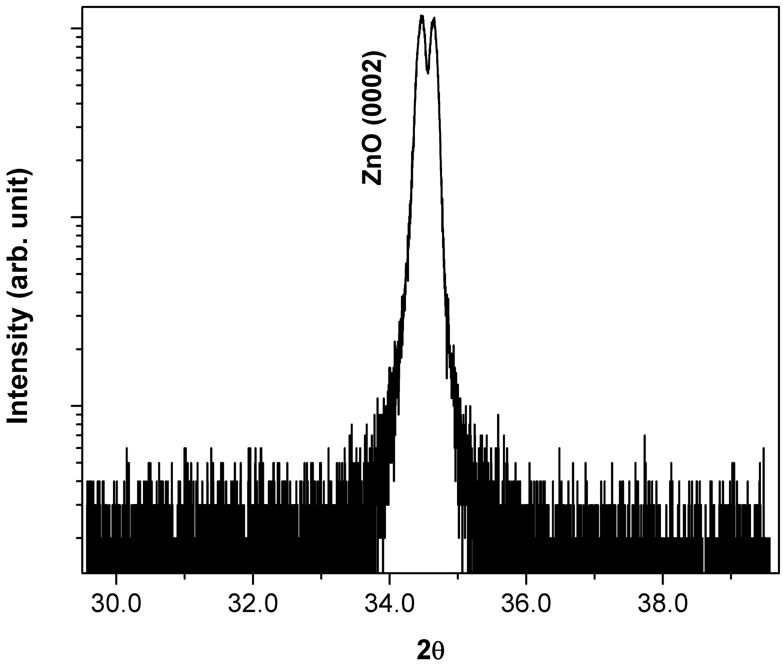

Figure 5.5: $\omega - 2\theta$ scan of $Mg_xZn_{1-x}O/ZnO$ heterostructure with $x = 0.26$.

tion data for $x = 0.16$, 0.26 and 0.40. For comparison we have also presented the result of photoabsorption measurements on bare ZnO film in the same figure by red curve. The results clearly show successful growth of MgZnO/ZnO heterostructures with quite well defined band edges. The band edge of ZnO was found to be at ≈ 3.3 eV, whereas the band edges of $Mg_xZn_{1-x}O$ were found to be at 3.79, 4.13 and 4.64 eV respectively for $x = 0.16$, 0.26 and 0.40. However the band edges somewhat flattens for higher values of x due to degradation of lattice structure and the associated band tailing.

5.2.3 Electrical properties and 2D weak localization effect

The results of room temperature sheet resistance measurements on the $Mg_xZn_{1-x}O/ZnO$ are shown in figure 5.7. The sheet resistance of bare ZnO thin film was ≈ 19 kΩ which drastically reduced to ≈ 1.8 kΩ as a result of introduction of a ≈ 50 nm thick $Mg_xZn_{1-x}O$

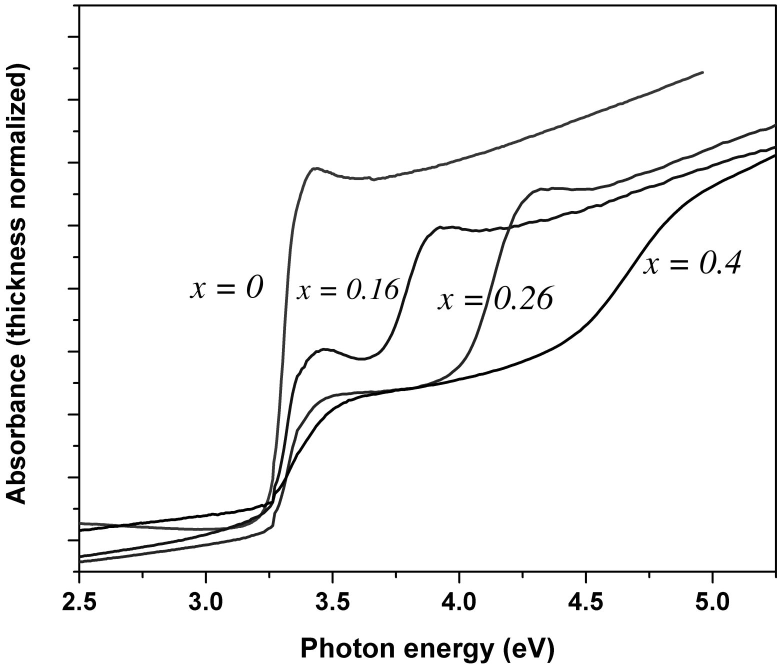

Figure 5.6: Photoabsorption spectra of $Mg_xZn_{1-x}O$/ZnO heterostructures with $x = 0$, $x = 0.16$, $x = 0.26$ and $x = 0.4$.

(with x=0.16) film on top. It can be noted here that $Mg_xZn_{1-x}O$ films when grown on alumina were insulating. On increasing the Mg concentration (x) in the MgZnO layer to $\approx$ 40%, the sheet resistance further reduced to $\approx$ 0.8 kΩ. In the figure 5.8, the results of room temperature Hall measurements are shown. As can be seen the electron concentration increased monotonically from $\approx 3\times10^{13}$ cm^{-2} for bare ZnO to $\approx 3\times10^{14}$ cm^{-2} for the $Mg_{0.4}Zn_{0.6}O$/ZnO. The increase in electron concentration and decrease in resistivity of $Mg_xZn_{1-x}O$/ZnO heterostructures are attributed in literature to the creation of a two dimensional electron gas (2DEG) at the heterointerface as a result of accumulation of a large quantity of electrons at the interface due to strong built-in potential arising out of macroscopic polarization mismatch between MgZnO and ZnO layers [173,174,188]. This accumulation of large number of carriers at the interface is expected to screen the ionized impurity and the grain boundary potential resulting in the increase in electron mobility [188–190]. The variation of electron mobility as a function of Mg concentration (figure

5.8) in $Mg_xZn_{1-x}O/ZnO$ heterostructures demonstrates this fact. As can be seen, the mobility increased from ≈ 11 cm^2/V-s for bare ZnO to ≈ 34 cm^2/V-s for the $Mg_xZn_{1-x}O/ZnO$ with $x = 0.26$. On further increase in the Mg concentration mobility slightly decreased to ≈ 27 cm^2/V-s possibly as a result of lattice structure degradation [188].

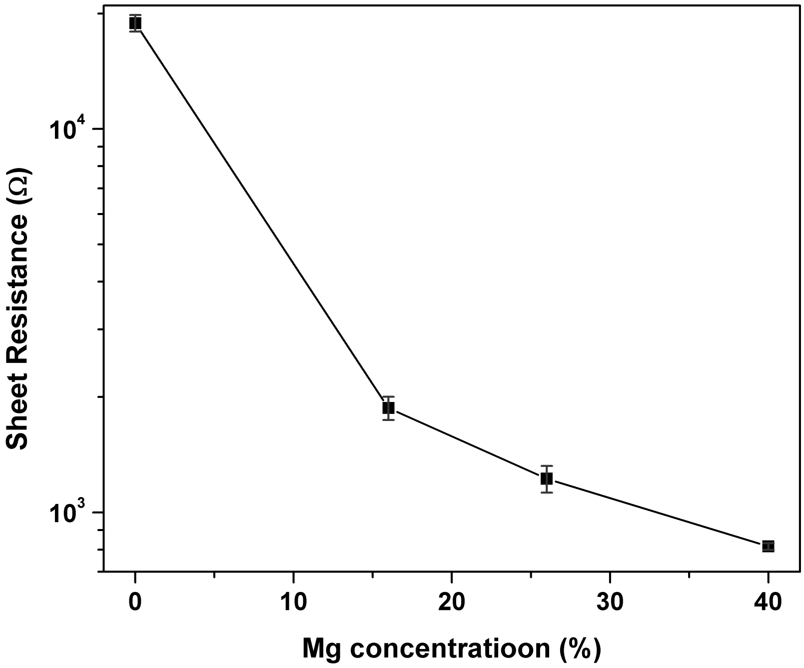

Figure 5.7: Variation of sheet resistance of $Mg_xZn_{1-x}O/ZnO$ heterostructures as a function of Mg concentration (x).

The results of temperature dependent electron concentration (n) measurements on the films are shown in figure 5.9. There was no significant variation of electron concentration with temperature in all the $Mg_xZn_{1-x}O/ZnO$ heterostructures as well as the ZnO film implying that the conducting electrons are not a result of thermal activation. Moreover, as previously mentioned, the sheet carrier density in the $Mg_xZn_{1-x}O/ZnO$ heterostructures is much higher than that in pure ZnO films. This supports that the reduction in resistivity and increase in the sheet electron concentration is due primarily to the formation of a 2DEG at the heterointerface. The slight decrease in n with lowering temperature

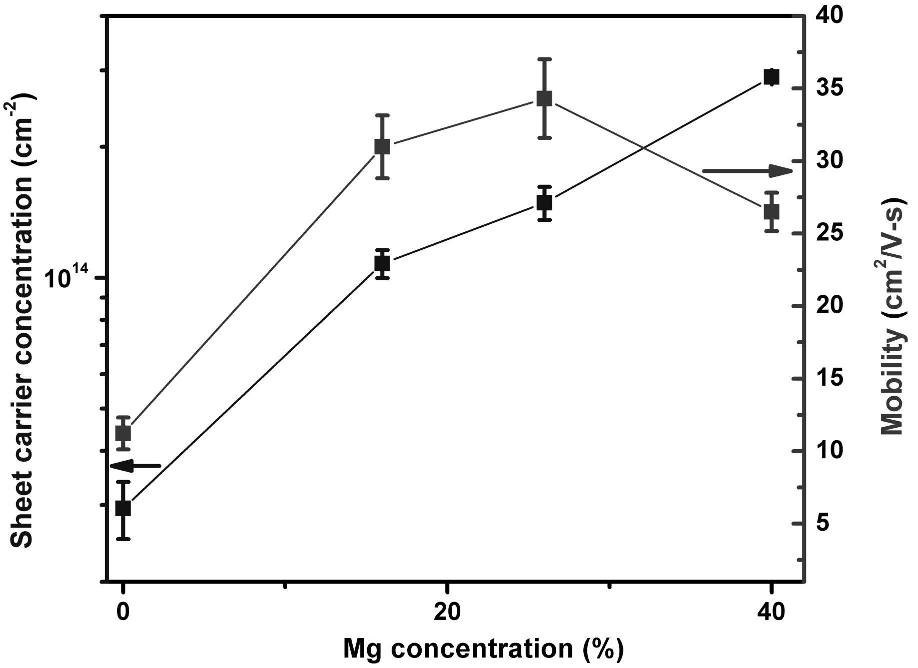

Figure 5.8: Variation of electron concentration and mobility as a function of Mg concentration (x).

seen for the heterostructures with $x = 0.16$ and 0.26 was plausibly caused by the presence of electron interference effects as discussed later [58, 160, 191]. Further support for the 2DEG can be seen from the temperature dependent electron mobility data shown in figure 5.10. It has been already mentioned that the electron mobility in the $Mg_xZn_{1-x}O$/ZnO heterostructures were almost 3 times higher than that in pure ZnO film. From figure 5.10 it can be further seen that the electron mobility was almost temperature independent in all the $Mg_xZn_{1-x}O$/ZnO heterostructures, especially at temperatures lower than 100 K. On the contrary the electron mobility in ZnO films gradually decreased as the temperature was lowered. It is a well known fact that the reduction in mobility in semiconductors with decreasing temperature occurs at low temperature region because of ionized impurity scatterings [188–190]. The absence of this effect implied that the high sheet carrier concentration of the 2DEG at the interface effectively screens the impurity potentials, thereby nullifying their scattering effects. In fact, the surface roughness scattering of the 2DEG

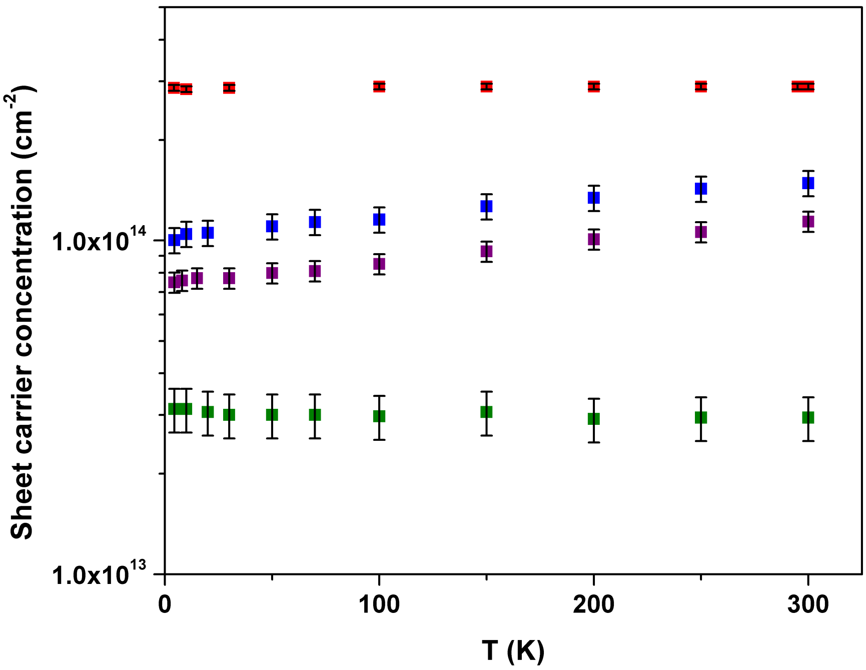

Figure 5.9: Variation of electron concentration as a function of temperature (T) for $Mg_xZn_{1-x}O$/ZnO heterostructures with x = 0 (green), x = 0.16 (purple), x = 0.26 (blue) and x = 0.4 (red).

at the MgZnO/ZnO interface would make the electron mobility at low temperature to be temperature independent [192]. Hence it can be concluded from the results of temperature dependent mobility and electron concentration measurements that a 2DEG is indeed formed at the MgZnO/ZnO interface.

Having established the formation of 2DEG at the interface, we now proceed to discuss the temperature dependent resistivity behavior of the MgZnO/ZnO heterostructures. The variation of sheet resistance of the structures as a function of temperature is shown in figure 5.11 in the temperature range from 100 to 4.2 K. It is clear that all the structures showed negative temperature coefficient of resistivity i.e. as the temperature was reduced the sheet resistance increased. The ratio of sheet resistance at 4.2 K to that at 300 K was about 1.1, 1.6 and 2.1 for the MgZnO/ZnO heterostructures with Mg concentration of 40, 26 and 16 % respectively. One possible reason for this rather small increase in resistivity

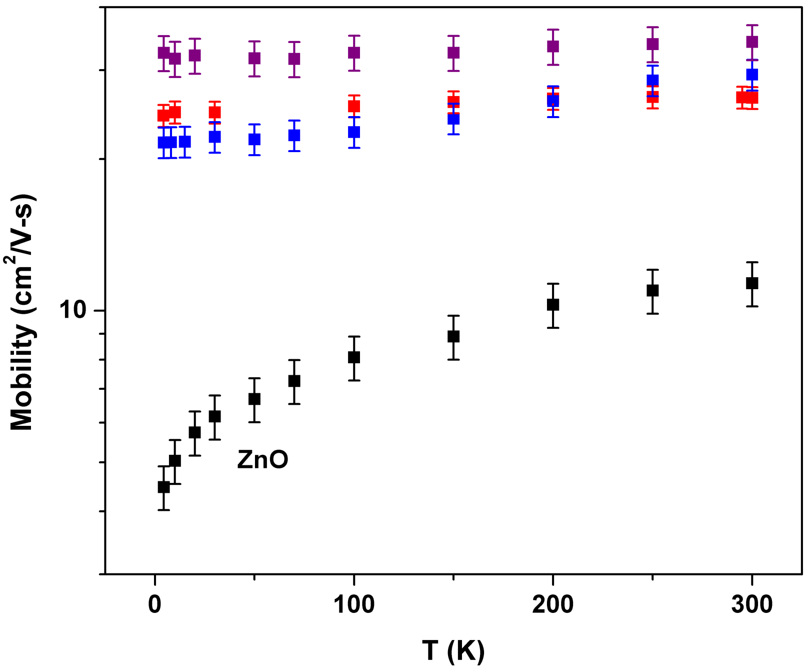

Figure 5.10: Variation of electron mobility as a function of temperature (T) for $Mg_xZn_{1-x}O/ZnO$ heterostructures with $x = 0$ (black), $x = 0.16$ (blue), $x = 0.26$ (purple) and $x = 0.4$ (red).

is the electron interference effect which arises if the mean free path (l) of the electrons becomes comparable to the Fermi wavelength (λ_F) [32, 57]. For a 2D system, the ratio of l to λ_F is given by [16, 18],

$$\frac{l}{\lambda_F} = \frac{h/e^2}{2\pi R_s} \tag{5.5}$$

The values of this ratio at 4.2 K for the three $Mg_xZn_{1-x}O/ZnO$ structures are 1.0, 2.1 and 4.4 for $x = 0.16$, 0.26 and 0.40 respectively. Therefore the electron interference effects should, in principle, be quite important to determine the low temperatures resistivity behaviors. As has been mentioned in chapters 1 and 4, there are two main components to the electron interference effects. One is called electron self interference or weak localization whereas the other is inter-electron interference effect which is more formally known as renormalized Coulomb electron-electron interaction (REEI) [32, 58]. Weak localization is caused by the enhancement of the probability of backscattering of electrons due to

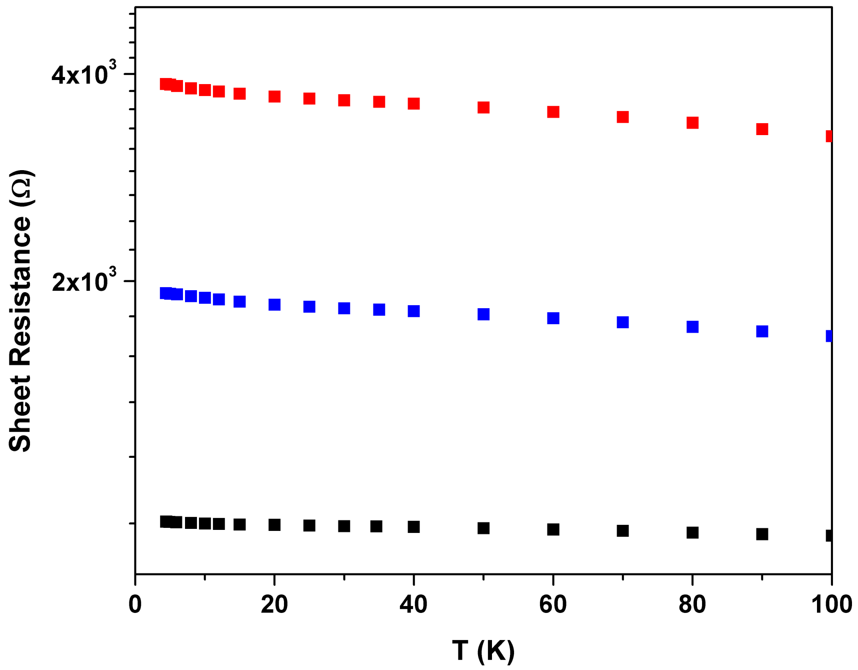

Figure 5.11: Variation of sheet resistance as a function of measurement temperature (T) $Mg_xZn_{1-x}O/ZnO$ heterostructures for $x = 0.16$ (red), $x = 0.26$ (blue), $x = 0.4$ (black).

constructive self-interference of electron waves around a closed path via multiple elastic scattering. Since a perpendicular magnetic field can destroy the phase coherence of electron waves, the backscattering probability diminishes in presence of magnetic field. As a result the presence of weak localization in a sample can give rise to negative transverse magnetoresistance [32, 58]. On the other hand, although REEI can give rise to positive transverse magnetoresistance, its magnitude is relatively small compared to that obtained for weak localization. Therefore in presence of weak localization, the transverse magnetoresistance is almost always found to be negative, except at very high fields where the effect of weak localization is minimized [58]. However, REEI is expected to give rise to a change in Hall coefficient proportional to change in conductivity as per equation 4.2. The small change in n seen in the heterostructures with $x = 0.16$ and 0.26 may be because of this small change in Hall coefficient as a result of inter-electron interference effects. But this effect was negligible in the heterostructure with $x = 0.40$ where there was practically no variation in Hall coefficient with temperature.

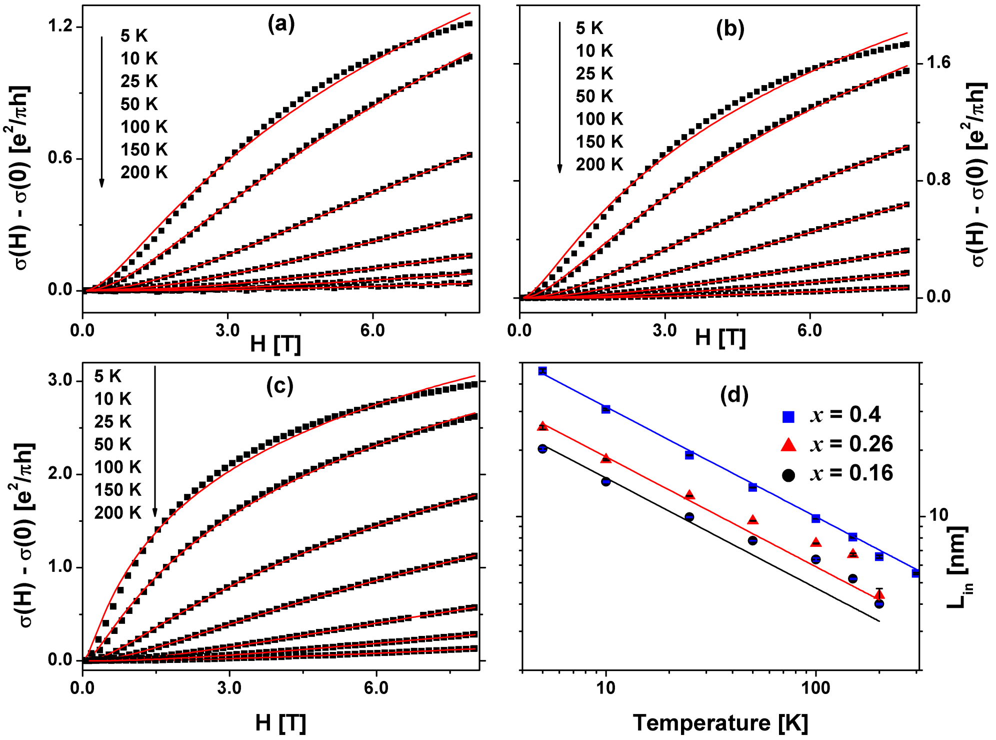

Figure 5.12: Magnetoconductance $[\sigma(H) - \sigma(H = 0)]$ in units of $e^2/\pi h$ as a function of magnetic field H at different temperatures for $Mg_xZn_{1-x}O/ZnO$ heterostructures with (a) $x = 0.16$, (b) $x = 0.26$ and (c) $x = 0.40$. Red curves show fit of the data as per equation 5.6. (d) Inelastic scattering length as a function of temperatures for the three heterostructures. Solid lines show fitting according to $L_{in} \propto T^{-1/2}$.

To study electron interference in detail, we measured magnetoresistance of the heterostructures as a function of magnetic field (H) and temperature. All the films showed negative transverse magnetoresistance (positive magnetoconductance), the magnitude of which decreased with increasing temperature, implying that the low temperature transport properties of the heterostructures were dominated by weak localization. Figure 5.12a-c show the magnetoconductance $[\sigma(H) - \sigma(H = 0)]$ of the MgZnO/ZnO heterostructures in units of $e^2/\pi h$ as a function of H at different temperatures. For weak localization in 2D, in absence of spin-flip scattering, the magneto conductance can be calculated by [58],

$$\sigma(H,T) - \sigma(H=0,T) = \frac{e^2}{\pi h}\left[\psi\left(\frac{1}{2}+\frac{1}{z}\right) + \ln z\right] \tag{5.6}$$

where ψ is the digamma function and $z = L_{in}^2 4eH/\hbar$, L_{in} is the inelastic scattering length. The magnetoconductance of the heterostructures were fitted using equation 5.6 as shown by the red curves in figure 5.12. The values of the fitting parameter L_{in} as a function of temperature are shown in figure 5.12d. The slope of the L_{in} vs. T graph in log-log plot was found to be close to -0.5, implying $L_{in} \propto T^{-1/2}$. This means that the dominant dephasing mechanism in the heterostructures was electron-electron scattering [58, 158]. It can be seen that with increasing Mg concentration in the heterostructures, the magnetoconductance and inelastic scattering length increased. This was due to increase in the electron concentration in the heterostructures, which enhanced the Fermi energy resulting in increase in the electron-electron inelastic scattering length [32]. We observed positive magnetoconductance even at 300 K for the sample with $x = 0.4$, which implied quantum effects at room temperature. This kind of behavior in ZnO is due to the fact that the electron dephasing length can be longer than the elastic scattering length even up to room temperature [191].

The temperature dependence of the weak localization and REEI arise because of the temperature dependence of the phase breaking inelastic scattering mechanisms [32]. Theoretically it has been found that in both the cases of the quantum interference effects the conductance of a 2D system varies logarithmically with the temperature and is given by [58],

$$\sigma = \sigma_0 + \frac{e^2}{\pi h}\left[p + \left(1 - \frac{3}{4}F_\sigma\right)\right]\ln(T/T_0) \tag{5.7}$$

where σ_0 is the Drude conductance, T is the temperature and T_0 is a constant. The first term in the bracket gives the contribution due to weak localization and the second term gives the effect of REEI. p is a parameter whose value depends on the nature of the dephasing mechanism active. For weak localization if the dominant dephasing mechanism is electron-electron collision, the value of p is 1 and if the dominant dephasing mechanism is electron-phonon collision, then $p = 3$ [58, 158]. F_σ is a parameter that takes into account the Hartree part of the REEI. The value of this parameter is difficult to determine accurately unless positive magnetoresistance is observed.

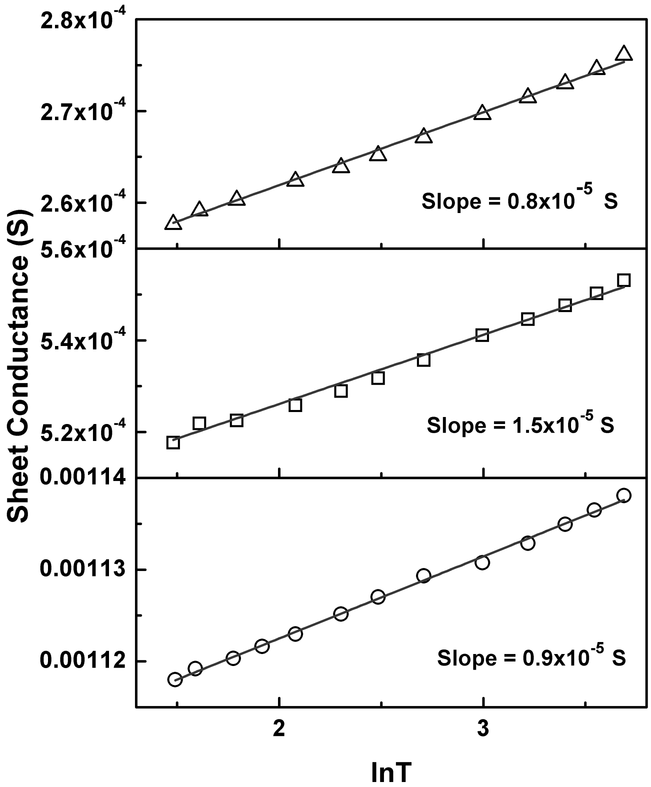

Figure 5.13: Sheet conductance as a function of ln(T) for $Mg_xZn_{1-x}O$/ZnO heterostructures for $x = 0.16$ (triangles), $x = 0.26$ (squares), $x = 0.4$ (circles).

Figure 5.13 shows the sheet conductance as a function of $\ln T$. The linearity of the graph in the temperature range from 40 to 4.2 K indeed proves the presence of 2D quantum interference effects. The values of slope obtained for the three heterostructures were 0.8×10^{-5}, 1.5×10^{-5} and 0.9×10^{-5} S for $x = 0.16$, 0.26 and 0.40 respectively, which are close to 1.2×10^{-5} S, the value of $e^2/\pi h$. Therefore the value of $[p + (1 - 3F_\sigma/4)]$ is close to 1, implying that the dominant interference phenomenon is weak localization (electron self interference) wherein the main dephasing mechanism is electron-electron collision [158], as was also found from fitting of magnetoconductance data. However, the role of REEI cannot be ruled out altogether from the data obtained, as the transverse magnetoresistance may be negative even if REEI is present [58]. The deviation of the value of $[p + (1 - 3F_\sigma/4)]$ from unity may indeed be caused by the presence of REEI. In fact the variation in slopes for the three samples may be due to different degree of REEI present. Nevertheless, the logarithmic variation of conductivity with temperature reveals that the quantum interference effects play a significant role in shaping up the low temperature transport properties of 2DEG formed at the polycrystalline MgZnO/ZnO interface.

5.3 Conclusion

In conclusion, two sets of studies were carried out to understand the effects of disorder on the electrical and optical properties of MgZnO/ZnO heterostructures. In the first set $Mg_{0.3}Zn_{0.7}O$/ZnO bilayers were successfully grown by PLD on alumina substrates. The bilayers were subsequently annealed at different temperatures from 600 to 900^0C to study the effect of Mg diffusion on the optical properties. The diffusion of Mg across the interface from MgZnO to ZnO layer could be directly seen from SIMS depth profile measurements. It was found that the diffusion of Mg significantly modified the optical properties of the ZnO layer of the heterostructure and as a result changed the overall PL spectra. Numerical simulations using the experimental Mg concentration profile as the input nicely reproduced the PL spectra of all the samples. The defects and disorder brought about by diffusion of Mg thus play a significant role in deciding the optical properties of the ZnO and MgZnO layers of MgZnO/ZnO heterostructure.

In the second set polycrystalline MgZnO/ZnO heterostructures were deposited by pulsed laser deposition on c-alumina substrates and the role of quantum interference effect on its low temperature transport properties was studied. It was found that on increasing Mg concentration in the MgZnO layer from 0 to 40%, the sheet electron concentration increased and the sheet resistance decreased. In addition the electron concentration and mobility were almost temperature independent, indicating the formation of 2DEG at the interface. The low temperature resistivity measurements showed a negative temperature coefficient of resistivity together with negative transverse magnetoresistance. These could be explained using the models of electron interference mediated quantum corrections to conductivity suitable for 2D system, implying the fact that electron interference phenomena is important in case of 2DEG formed at the MgZnO/ZnO interface. From these studies it could be concluded that the disorder related to the diffusion of Mg and other structural and point defects significantly alter the low temperature transport properties of the 2DEG confined at the ZnO side of the heterostructures.

Chapter 6

Conclusion and scope for future work

In conclusion we have studied the effects of disorder on the optical and electrical properties of doped ZnO thin films. ZnO films are doped with different impurities for different practical applications. It is understood that doping creates disorder as the dopant atoms are statistically distributed throughout the film. Moreover, the atomic sizes of dopant atoms are different from that of Zn and O, which creates additional structural and point defects. These defects and disorder were found to cause bandgap narrowing, band tailing, PL peak broadening, semiconductor to metal transition, quantum corrections to conductivity and strong localization of carriers in doped ZnO thin films.

To study the effects of defects and disorder on the optical and electrical properties of doped ZnO thin films, we first chose Si as a dopant in ZnO. Si is an n-type dopant, which is useful for the application of ZnO thin films as transparent conducting electrodes. Highly transparent and c-axis oriented Si doped ZnO thin films were grown by sequential pulsed laser deposition on c-alumina substrates. Resistivity of these films was found to decrease rapidly to a minimum of $\approx 6.2\times10^{-4}$ ohm-cm and then increase slightly with increasing Si doping. The decrease of resistivity was due to enhancement in the electron density and associated semiconductor to metal transition caused by Si doping. It was found that with increasing Si doping the optical bandgap increased. This blue shift of the bandgap was a collective effect of the Burstein-Moss blue shift due to the Fermi level being pushed up into the conduction band and the bandgap narrowing caused by disorder. The optical transmission spectra also showed that with increasing Si concentration the steepness of band edges decreased due to band tailing caused by heavy doping induced disorder. Further, room temperature near band edge photoluminescence was observed in all the films, the FWHM of which increased with increasing Si doping due to disorder induced potential fluctuations. Therefore it could be concluded that Si doping related disorder caused semiconductor to metal transition, bandgap narrowing, PL peak broadening and band tailing in Si doped ZnO films.

One important aspect of doping related disorder is quantum corrections to conductivity, which can be observed in the low temperature transport properties of doped ZnO thin films. To study quantum corrections to conductivity in Si doped ZnO thin films, two set of experiments were carried out. In one set, the film thickness was kept constant at $\approx$ 230 nm and the Si concentration was varied from 0.5 to 5.8%, while in the other set Si concentration was kept constant at $\approx$ 2% but the film thickness was varied from $\approx$ 15 to 40 nm. In the first case, although the electron concentration in the films were higher than the Mott critical density, all the films showed negative temperature coefficient of resistivity (TCR) at low temperatures. The temperature independent nature of electron concentration together with the negative low field magnetoresistance found in the films at low temperatures pointed to weak localization as the dominant contributor towards negative TCR. A phenomenological fit of the temperature dependent resistivity data for all the films could be obtained by considering the quantum corrections to conductivity arising due to disorder induced weak localization effect, wherein both the influences of electron-electron and electron-phonon inelastic dephasing processes were included using Matthiessen's rule. In case of the $Si_{0.02}Zn_{0.98}O$ films with fixed Si concentration of $\approx$ 2% and thickness varying in the range from $\approx$ 15 to 40 nm grown by PLD on alumina substrates, the film with thickness of $\approx$ 40 nm showed typical metallic behavior in the temperature dependent sheet resistance measurements. On the other hand the film with thickness ≈15 nm showed a strongly localized behavior where the dominant mechanism of conduction at low temperature was 3D VRH. This implied a thickness driven metal to insulator transition in Si doped ZnO films. The sheet resistance of the film with thickness of ≈ 30 nm was almost temperature independent, signifying that it was in the critical region. Finally the film with thickness of ≈ 20 nm showed a temperature dependent dimensional crossover from 3D to 2D weak localization with decreasing temperature. These results clearly demonstrated that the disorder caused by doping significantly alters the low temperature transport properties of Si doped ZnO thin films. It could also be seen that the effects of disorder on the transport properties of the Si doped ZnO films depends not only on the Si concentration but on the film thickness as well. These findings generated deeper insights into the effects of disorder on the low temperature transport properties of $Si_xZn_{1-x}O$ films.

Next we considered the MgZnO/ZnO heterostructures. These heterostructures are suitable for applications in High Electron Mobility Transistor (HEMT), quantum well lasers, quantum Hall effect, resonant-tunneling diodes etc. Due to macroscopic polarization mismatch between MgZnO and ZnO layers there can be accumulation of electrons at the interface quantum well on the ZnO side of the heterostructures. Since the MgZnO films are often grown in metastable state with much higher Mg composition than that is allowed by solubility limit, diffusion of Mg from the MgZnO into the ZnO layer during the growth process can hamper the sought after electrical and optical properties of the heterostructures. The diffused Mg will increase the bandgap on the ZnO side of the heterostructure. They will also act as scattering centers for electrons. We carried out two sets of studies to understand the effects of disorder on the electrical and optical properties of MgZnO/ZnO heterostructures. In the first set, $Mg_{0.3}Zn_{0.7}O$/ZnO bilayers were successfully grown by PLD on c-alumina substrates. These were subsequently annealed at different temperatures from 600 to 900^0C to study the effect of Mg diffusion on the optical properties. The diffusion of Mg across the interface from MgZnO to ZnO layer could be directly seen from SIMS depth profile measurements. It was found that the diffusion of Mg significantly blue-shifted the PL peak position of the ZnO layers and, as a consequence, altered the PL spectra of the heterostructures. Numerical simulations using the experimental Mg concentration profile as the input nicely reproduced the PL spectra of all the samples. The defects and disorder brought about by diffusion of Mg thus play a significant role in deciding the optical properties of the MgZnO/ZnO heterostructure. In the second set, polycrystalline MgZnO/ZnO heterostructures were deposited by pulsed laser deposition on c-alumina substrates and the role of quantum interference effect on their low temperature transport properties was studied. It was found that on increasing Mg concentration in the MgZnO layer from 0 to $\approx$ 40%, the sheet electron concentration increased by one order of magnitude from 3×10^{13} cm^{-2} to 3×10^{14}cm^{-2}. The sheet resistance was also found to decrease correspondingly. In addition the electron concentration and mobility were almost temperature independent, indicating the formation of 2DEG at the interface. The low temperature resistivity measurements of the heterostructures showed a negative temperature coefficient of resistivity together with negative magnetoresistance. These could be explained using the models of quantum corrections to conductivity suitable for 2D system, implying the fact that electron interference phenomena was important in case of 2DEG formed at the MgZnO/ZnO interfaces. The electron interference phenomena occur due to multiple elastic scattering of electrons from disorder caused by Mg diffusion and other related structural and point defects present at the interface. From these studies it could therefore be concluded that the disorder related to the diffusion of Mg significantly alters the low temperature transport properties of the 2DEG confined at the ZnO side of the MgZnO/ZnO heterostructures.

It emerged from our studies that Si can be used as a suitable dopant in ZnO for transparent conducting electrode (TCE) applications. However, it has also been found that there is a lower limit to the thickness of Si doped ZnO thin films for its practical application as transparent conducting electrodes. At lower thickness the quantum effects dominate the transport properties of Si doped ZnO films and the films can even undergo a metal to insulator transition. The cause of this thickness driven metal to insulator transition is not clearly understood. But one possible reason could be drastic changes in crystalline quality of the films at lower thickness. The porosity of the films may be yet another reason for the observed metal to insulator transition at low film thickness. This aspect of the ultra thin Si doped ZnO films can be further probed by using detailed x-ray reflectivity measurements, which is left in the present thesis as future scope of work. In case of the MgZnO/ZnO heterostructures, there was reduction of resistivity as a result of accumulation of electrons at the interface. As a result, these kind of heterostructures can also be a suitable candidate for 2DEG based transparent conducting electrode (TCE) applications. However this requires further optimization of the growth process of the heterostructures, which would be carried out in the future.

References

[1] C. Jagadish and S. Pearton(Editors), *Zinc Oxide Bulk, Thin Films and Nanostructures: Processing, Properties, and Applications*. Elsevier, Amsterdam, 2006.

[2] U. Ozgur, Y. I. Alivov, C. Liu, A. Teke, M. A. Reshchikov, S. Dogan, V. Avrutin, S.-J. Cho, and H. Morkoc *J. Appl. Phys.*, vol. 98, p. 041301, 2005.

[3] A. Janotti and C. G. V. de Walle *Rep. Prog. Phys.*, vol. 72, p. 126501, 2009.

[4] V. Bhosle, A. Tiwari, and J. Narayan *Appl. Phys. Lett.*, vol. 88, p. 032106, 2006.

[5] H. Agura, A. Suzuki, T. Matsushita, and M. O. T. Aoki *Thin Solid Films*, vol. 445, p. 263, 2003.

[6] T. Minami, H. Sato, H. Nanto, and S. Takata *J. J. Appl. Phys.*, vol. 25, p. L776, 1986.

[7] F. K. Shan, B. I. Kim, G. X. Liu, Z. F. Liu, J. Y. Sohn, W. J. Lee, B. C. Shin, and Y. S. Yu *J. Appl. Phys.*, vol. 95, p. 4772, 2004.

[8] S. Vijayalakshmi *et al. J. Phys. D: Appl. Phys.*, vol. 41,, p. 245403, 2008.

[9] C. Liu, F. Yun, and H. Morkoc *Journal of Materials Science: Materials in Electronics*, vol. 16, pp. 555–597, 2005.

[10] T. Minami, T. Yamamoto, and T. Miyata *Thin Solid Films*, vol. 366, pp. 63–68, 2000.

[11] P. T. Craddock *et al.*, *Zinc in India: 2000 years of zinc and brass*. British Museum, 1998.

[12] Y. Liu, C. R. Gorla, S. Liang, N. Emanetoglu, Y. Lu, H. Shen, and M. Wraback *Journal of Electronic Materials,*, vol. 29, pp. 69–74, 2000.

[13] Y.-Y. Lai, Y.-P. Lan, and T.-C. Lu *Light: Science & Applications*, vol. 2, p. e76, 2013.

[14] S. F. Yu, C. Yuen, S. P. Lau, and H. W. Lee *Appl. Phys. Lett.*, vol. 84, p. 3244, 2004.

[15] X. D. Liu, E. Y. Jiang, and Z. Q. Li *J. Appl. Phys.*, vol. 102, p. 073708, 2007.

[16] C. X. Xu, C. Yang, B. X. Gu, and S. J. Fang *Chinese Science Bulletin*, vol. 58, pp. 2563–2566, 2013.

[17] O. Lupan, G. Chai, and L. Chow *Microelectronic Engineering*, vol. 85, pp. 2220–2225, 2008.

[18] L. Znaidi *Materials Science and Engineering B*, vol. 174, p. 18, 2010.

[19] W. Gao and Z. Li *Ceramics International*, vol. 30, p. 1155, 2004.

[20] A. El-Shaer, A. C. Mofor, A. Bakin, and M. Kreye *A. Waag and Superlattices and Microstructures*, vol. 38, p. 265, 2005.

[21] N. M. Sbrockey and S. Ganesan *III-Vs Review*, vol. 17, p. 23, 2004.

[22] D. C. Agarwal, R. S. Chauhan, A. Kumar, D. Kabiraj, F. Singh, S. A. Khan, D. K. Avasthi, J. C. Pivin, M. Kumar, J. Ghatak, and P. V. Satyam *J. Appl. Phys.*, vol. 99, p. 123105, 2006.

[23] S. L. King, J. Gardeniers, and I. W. Boyd *Applied Surface Science*, vol. 96, p. 811, 1996.

[24] E. Guziewicz, M. Godlewski, T. Krajewski, . Wachnicki, A. Szczepanik, K. Kopalko, A. Wojcik-Glodowska, E. Przezdziecka, W. Paszkowicz, E. Lusakowska, P. Kruszewski, N. Huby, G. Tallarida, and S. Ferrari *J. Appl. Phys.*, vol. 105, p. 122413, 2009.

[25] A. Janotti and C. G. V. de Walle *Phys. Rev. B.*, vol. 76, p. 165202, 2007.

[26] J. Fan, K. Sreekanth, Z. X. d, S. Chang, and K. Rao *Progress in Materials Science*, vol. 58, pp. 874–985, 2013.

[27] A. Janotti and C. G. V. de Walle *Rep. Prog. Phys.*, vol. 72, p. 126501, 2009.

[28] H. P. Sun, X. Q. Pan, X. L. Du, Z. X. Mei, Z. Q. Zeng, and Q. K. Xue *Appl. Phys. Lett.*, vol. 85, p. 4385, 2004.

[29] J. I. Pankove, *Optical processes in semiconductors*. Dover Publishing Inc. New York, 1975.

[30] S. C. Jain and D. J. Roulston *Solid-State Electronics*, vol. 34, pp. 453–65, 1991.

[31] N. F. Mott *Philos. Mag.*, vol. 6, p. 287, 1961.

[32] V. F. Gantmakher, *Electrons and Disorder in Solids*. Oxford Science Publications, Oxford, 2005.

[33] M. Nistor, F. Gherendi, N. B. Mandache, C. Hebert, J. Perriere, and W. Seiler *J. Appl. Phys.*, vol. 106, p. 103710, 2009.

[34] X. D. Liu, E. Y. Jiang, and Z. Q. Li *J. Appl. Phys.*, vol. 102, p. 073708, 2007.

[35] C. Klingshirn, *Semiconductor Optics*. Springer, Berlin , 2005.

[36] M. Reshchikov, H. Morkoc, B. Nemeth, J. Nause, J. Xie, B. Hertog, and A. Osinsky *Physica B: Condensed Matter*, vol. 358, pp. 401–402, 2007.

[37] I. Ohkubo, Y. Matsumoto, A. Ohtomo, T. Ohnishi, A. Tsukazaki, M. Lippmaa, H. Koinuma, and M. Kawasaki *Applied Surface Science*, vol. 159-160 and, pp. 514–519, 2000.

[38] P. Misra, P. K. Sahoo, P. Tripathi, V. N. Kulkarni, R. V. Nandedkar, and L. M. Kukreja *Appl. Phys. A*, vol. 78, p. 37, 2004.

[39] E. M. Kaidashev, M. Lorenz, H. von Wenckstern, A. Rahm, H.-C. Semmelhack, K.-H. Han, G. Benndorf, C. Bundesmann, H. Hochmuth, and M. Grundmann *Appl. Phys. Lett.*, vol. 82, p. 3901, 2003.

[40] A. Ohtomo, K. Tamura, K. Saikusa, K. Takahashi, T. Makino, Y. Segawa, H. Koinuma, and M. Kawasaki *Appl. Phys. Lett.*, vol. 75, p. 2635, 1999.

[41] B. K. Meyer, H. Alves, D. M. Hofmann, W. Kriegseis, D. Forster, F. Bertram, J. Christen, A. Hoffmann, M. Strassburg, M. Dworzak, U. Haboeck, and A. V. Rodina *phys. stat. sol. b*, vol. 241, pp. 231– 260, 2004.

[42] K. Vanheusden, W. L. Warren, C. H. Seager, D. R. Trallant, and J. A. Voigt *J. Appl. Phys.*, vol. 79, p. 7983, 1996.

[43] K. C. Mishra, P. C. Schmidt, K. H. Johnson, B. G. DeBoer, J. K. Berkowitz, and E. A. Dale *Phys. Rev. B*, vol. 42, p. 1423, 1990.

[44] D. C. Reynolds, D. C. Look, B. Jogai, and H. Morkoc *Solid State Commun.*, vol. 101, p. 643, 1997.

[45] D. C. Reynolds, D. C. Look, B. Jogai, J. E. V. Nostrand, R. Jones, and J. Jenny *Solid State Commun.*, vol. 106, p. 701, 1998.

[46] A. F. Kohan, G. Ceder, D. Morgan, and C. G. V. de Walle *Phys. Rev. B*, vol. 61, p. 15019, 2000.

[47] T. Sekiguchi, N. Ohashi, and Y. Terada *Jpn. J. Appl. Phys.*, vol. 36, p. L289, 1997.

[48] L. Wang and L. C. Giles *J. Appl. Phys.*, vol. 94, p. 973, 2003.

[49] J. D. Albrecht, P. P. Ruden, S. Limpijumnong, W. R. Lambrecht, and K. F. Brennan *J. Appl. Phys.*, vol. 86, pp. 6864–6869, 1999.

[50] D. C. Look, D. C. Reynolds, J. R. Sizelove, R. L. Jones, C. W. Litton, G. Cantwell, and W. C. Harsch *Solid State Communications*, vol. 105, pp. 399–401, 1998.

[51] H. Kato, M. Sano, K. Miyamoto, and T. Yao *Jpn. J. Appl. Phys. Part 1*, vol. 42, p. 2241, 2003.

[52] K. Iwata, P. Fons, S. Niki, A. Yamada, K. Matsubara, K. Nakahara, and H. Takasu *Phys. Status Solidi a*, vol. 180, p. 287, 2000.

[53] A. Ohmoto and A. Tsukazaki *Semicond. Sci. Technol.*, vol. 20, p. S1, 2005.

[54] S. M. Park, T. I. kegami, and K. Ebihara *Thin Solid Films*, vol. 513, pp. 90–4, 2006.

[55] J. G. Lu *et al. J Appl. Phys.*, vol. 101, p. 083705, 2007.

[56] O. Bamiduro, H. Mustafa, R. Mundle, R. B. Konda, and A. K. Pradhan *Appl. Phys. Lett.*, vol. 90, p. 252108, 2007.

[57] A. F. Ioffe and A. R. Regel *Prog. Semicond.*, vol. 4, p. 237, 1960.

[58] P. A. Lee and T. V. Ramakrishnan *Rev. Mod. Phys.*, vol. 57, p. 287, 1985.

[59] A. Ishizumi and Y. Kanemitsu *Appl. Phys. Lett.*, vol. 86, p. 253106, 2005.

[60] F. Gu, S. F. Wang, M. K. Lu, G. J. Zhou, D. Xu, and D. R. Yuan *Langmuir*, vol. 20 9, pp. 3528–3531, 2004.

[61] S. Yang, C. C. Kuo, W.-R. Liu, B. H. Lin, H.-C. Hsu, C.-H. Hsu, and W. F. Hsieh *Appl. Phys. Lett.*, vol. 100, p. 101907, 2012.

[62] T. Makino, Y. Segawa, S. Yoshida, A. Tsukazaki, A. Ohtomo, and M. Kawasaki *Appl. Phys. Lett.*, vol. 85, pp. 759–61, 2004.

[63] D. Chrisey and G. Hubler, *Pulsed Laser Deposition of Thin Film.* John Wiley and Sons, New York, 1994.

[64] J. T. Cheung and T. Magee *J. Vac. Sci. Tech A*, vol. 1, p. 1604, 1983.

[65] P. Misra and L. Kukreja *Thin Solid Films*, vol. 485, pp. 42–46, 2005.

[66] P. Misra, T. K. Sharma, S. Porwal, and L. M. Kukreja *Appl. Phys. Lett.*, vol. 89, p. 161912, 2006.

[67] T. J. Smith *Appl. Phys. Lett.*, vol. 43, p. 1108, 1983.

[68] C. Kirchner, T. Gruber, F. Reuss, K. Thonke, A. Waag, C. Giessen, and M. Heuken *J. Cryst. Growth*, vol. 248, p. 20, 2003.

[69] J. Wang, G. Du, B. Zhao, X. Yang, Y. Zhang, Y. Ma, D. Liu, Y. Chang, H. Wang, H. Yang, and S. Yang *J. Cryst. Growth*, vol. 255, p. 293, 2003.

[70] Y. Miao, Z. Ye, W. Xu, F. Chen, X. Zhou, B. Zhao, L. Zhu, and J. Lu *Applied Surface Science*, vol. 252, pp. 7953–7956, 2006.

[71] W. I. Park, G. Yi, and H. M. Jang *Appl. Phys. Lett.*, vol. 79, p. 2022, 2001.

[72] T. Gruber, C. Kirchner, R. Kling, F. Reuss, A. Waag, F. Bertram, D. Forster, J. Christen, and M. Schreck *Appl. Phys. Lett.*, vol. 83, p. 3290, 2003.

[73] M. Ritala and M. Leskela *Nanotechnology*, vol. 10, p. 19, 1999.

[74] E. Guziewicz, I. A. Kowalik, M. Godlewski, K. Kopalko, V. Osinniy, A. Wojcik, S. Yatsunenko, E. Lusakowska, W. Paszkowicz, and M. Guziewicz *J. Appl. Phys.*, vol. 103, p. 033515, 2008.

[75] S. K. Kim, C. S. Hwang, S. H. K. Park, and S. J. Y. and *Thin Solid Films*, vol. 478, p. 103, 2005.

[76] M. A. Herman and H. Sitter, *Molecular beam epitaxy: fundamentals and current Status*. Springer, Berlin, 1998.

[77] Y. Chen, D. Bagnall, Z. Zhu, T. Sekiuchi, K. T. Park, K. Hiraga, T. Yao, S. Koyama, M. Shen, and T. Goto *J. Cryst. Growth*, vol. 181, p. 165, 1997.

[78] N. Izyumskaya, V. Avrutin, W. Schoch, W. A. El-Shaer, F. Reuss, T. Gruber, and A. Waag *J. Cryst. Growth*, vol. 269, p. 356, 2004.

[79] K. Sakurai, D. Iwata, S. Fujita, and S. Fujita *Jpn. J. Appl. Phys.*, vol. 38, p. 2606, 1999.

[80] M. A. L. Johnson, S. Fujita, W. H. R. Jr., W. C. H. Jr., J. W. Cook, and J. F. Schetzina *J. Electron. Mater.*, vol. 25, p. 855, 1996.

[81] M. Sano, K. Miyamoto, H. Kato, and T. Yao *Jpn. J. Appl. Phys.*, vol. 42, p. L1050, 2003.

[82] J. E. Mahan, *Physical Vapor Deposition of Thin Films*. Wiley-VCH, 2000.

[83] A. P. Roth, J. B. Webb, and D. F. Williams *Phys. Rev. B*, vol. 25, p. 7836, 1982.

[84] A. Roth, J. Webb, and D. Williams *Solid State Communication*, vol. 39, p. 1269, 1981.

[85] B. E. Sernelius, K.-F. Berggren, Z.-C. Zin, I. Hamberg, and C. G. Granqvist *Phys. Rev. B*, vol. 37, pp. 10244–8, 1988.

[86] J. D. Ye, S. L. Gu, S. M. Zhu, S. M. Liu, Y. D. Zheng, R. Zhang, and Y. Shi *Appl. Phys. Lett.*, vol. 86, p. 192111, 2005.

[87] K. J. Kim and Y. R. Park *Appl. Phys. Lett.*, vol. 78, p. 475, 2001.

[88] S. Studenikin, N. Golego, and M. Cocivera *J. Appl. Phys.*, vol. 84, p. 2287, 2005.

[89] X. D. Liu, E. Y. Jiang, and Z. Q. Li *J. Appl. Phys.*, vol. 102, p. 073708, 2007.

[90] R. S. Thompson, D. Li, C. M. Witte, and J. G. Lu *Nano Lett.*, vol. 9 12, pp. 3991–3995, 2009.

[91] P. Misra, R. Nandedkar, and L. M. Kukreja *Solid State Commun.*, vol. 127, pp. 463–467, 2003.

[92] Z. W. Liu, C. K. Ong, T. Yu, and Z. X. Shen *Appl. Phys. Lett.*, vol. 88, p. 053110, 2006.

[93] G. Baraldi, R. Caballero, and C. Kaufmann *Energy Procedia*, vol. 10, pp. 38–42, 2011.

[94] W. S. Roman, H. Riascos, J. C. Caicedo, R. Ospina, and L. Tirado-Mejia *J. Phys.: Conf. Ser.*, vol. 167, p. 012004, 2009.

[95] M. Gaillard, E. A.-Chalhoub, C. B.-Leborgne, A. Petit, E. Millon, and N. Semmar *AIP Conf. Proc.*, vol. 1464, p. 179, 2012.

[96] A. A. Voevodin, J. G. Jones, J. S. Zabinski, Z. Czigan, and L. Hultman *J. Appl. Phys.*, vol. 92, p. 4980, 2002.

[97] M. Yoshimoto, Y. Hishitani, H. Maruta, H. Koinuma, T. Tachibana, S. Nishio, and M. Kakihana *MRS Proceedings*, vol. 555, p. 383, 1998.

[98] K. P. Acharya, H. Khatri, S. Marsillac, B. Ullrich, P. Anzenbacher, and M. Zamkov *Appl. Phys. Lett.*, vol. 97, p. 201108, 2010.

[99] K. Wang, G. Tai, K. H. Wong, S. P. Lau, and W. Guo *AIP Advances*, vol. 1, p. 022141, 2011.

[100] H. M. Smith and A. F. Turner *Appl. Opt.*, vol. 4, p. 147, 1965.

[101] D. Dijkkamp, T. Venkatesan, X. D. Wu, S. A. Shareen, N. Jiswari, Y. H. Min-Lee, W. L. McLean, and M. Croft *Appl. Phys. Lett.*, vol. 51, p. 619, 1987.

[102] P. R. Willmott and J. R. Huber *Reviews of Modern Physics*, vol. 72, p. 0034, 2000.

[103] T. P. Hughes, *Plasmas and Laser Light.* Wiley, New York, 1975.

[104] R. E. Russo *Appl. Spectrosc.*, vol. 49, p. 14A, 1995.

[105] J. J. Chang and B. E. Warner *Appl. Phys. Lett.*, vol. 69, p. 473, 1996.

[106] D. B. Geohegan, "Laser ablation in materials process-ing: Fundamentals and applications," *MRS Symposia Proceedings,*, vol. 285, p. 27, 1993.

[107] I. Weaver *J. Appl. Phys.*, vol. 79, p. 7216, 1996.

[108] A. Gupta and B. W. Hussey *Appl. Phys. Lett.*, vol. 58, p. 1211, 1991.

[109] R. F. Wood, K. R. Chen, J. N. Leboeuf, A. A. Puretsky, and D. B. Geohegan *Phys. Rev. Lett.*, vol. 79, p. 1571, 1997.

[110] S. Fahler, K. Sturm, and H.-U. Krebs *Appl. Phys. Lett.*, vol. 75, p. 3766, 1999.

[111] B. Schey, T. Bollmeier, M. Kuhn, W. Biegel, and B. Stritzker *Rev. Sci. Instrum.*, vol. 69, p. 474, 1998.

[112] M. N. R. Ashfold and F. Claeyssens *Chem. Soc. Rev.*, vol. 33, pp. 23–31, 2004.

[113] B. Lewis and J. C. Anderson, *Nucleation and Growth of Thin Films* . Academic, London, 1978.

[114] S. Choopun, R. Vispute, W. Noch, A. Balsamo, R. Sharma, T. Venkatesan, A. Iliadis, and D. Look *Appl. Phys. Lett.*, vol. 75, p. 3947, 1999.

[115] A. Gupta, B. Hussey, T. Shaw, A. Guloy, M. Chern, R. Saraf, and B. Scott *Journal of Solid State Chemistry*, vol. 112, p. 113, 1994.

[116] J. Song and Y. Jeong *Solid State Communications*, vol. 125, p. 563, 2003.

[117] H. Galinski, T. Ryll, P. Reibisch, L. Schlagenhauf, I. Schenker, and L. J. Gaucklr *Acta Materialia*, vol. 61, p. 3297, 2013.

[118] H. Sankur and J. T. Cheung *J. Vac. Sci. Technol. A*, vol. 1, p. 1806, 1983.

[119] M. Yan, M. Lane, C. R. Kannewurf, and R. P. H. Chang *Appl. Phys. Lett.*, vol. 78, p. 2342, 2001.

[120] L. van der Pauw *Philips Research Reports*, vol. 13, p. 1, 1958.

[121] L. van der Pauw *Philips Technical Review*, vol. 20, p. 220, 1958.

[122] P. Blood and J. W. Orton, *The Electrical Characterization of Semiconductors: Majority Carriers and Electron States*. Academic Pr, 1992.

[123] F. Urbach *Phys. Rev.*, vol. 92, p. 1324, 1953.

[124] B. D. Cullity and S. R. Stock, *Elements of X-ray diffraction*. Prentice Hall , 2002.

[125] J.-R. Duclere, B. Doggett, M. O. Henry, E. McGlynn, R. T. R. Kumar, J.-P. Mosnier, A. Perrin, and M. Guilloux-Viry *J. Appl. Phys.*, vol. 101, p. 013509, 2007.

[126] G. Williamson and W. Hall *Acta Metall. Mater.*, vol. 1, p. 22, 1953.

[127] W.-R. Liu, W. F. Hsieh, C.-H. Hsu, K. S. Liang, and F. S.-S. . Chien *J. Appl. Cryst.*, vol. 40, p. 924, 2007.

[128] P. Eaton and P. West, *Atomic Force Microscopy*. Oxford University Press , 2010.

[129] B. Cappella and G. Dietler *Surface Science Reports*, vol. 34, p. 1, 1999.

[130] G. Binnig and C. F. Quate *Physical Review Letters*, vol. 56, p. 930, 1986.

[131] L. Gross, F. Mohn, N. Moll, P. Liljeroth, and G. Meyer *Science*, vol. 325, p. 1110, 2009.

[132] N. A. Geisse *Materials Today*, vol. 12, p. 40, 2009.

[133] J. C. Vickerman, A. A. Brown, and N. M. Reed, *Secondary ion mass spectrometry: principles and applications*. Clarendon Press, 1989.

[134] A. Benninghoven, F. G. Rudenauer, and H. W. Werner, *Secondary Ion Mass Spectrometry: Basic Concepts, Instrumental Aspects, Applications and Trends*. Wiley-Interscience, 1987.

[135] S. Hufner, *Photoelectron spectroscopy: principles and applications*. Springer Verlag, 1995.

[136] P. van der Heide, *X-ray Photoelectron Spectroscopy: An introduction to Principles and Practices*. Wiley, 2011.

[137] J. Goldstein, *Scanning Electron Microscopy and X-Ray Microanalysis*. Springer, 2003.

[138] U. Ozgur, D. Hofstetter, and H. Morkoc *Proceedings of the IEEE*, vol. 98, pp. 1255–1268, 2010.

[139] V. Bhosle, A. Tiwari, and J. Narayan *J. Appl. Phys.*, vol. 100, p. 033713, 2006.

[140] B.-T. Lee, T.-H. Kim, and S.-H. Jeong *J. Phys. D: Appl. Phys.*, vol. 39, pp. 957–61, 2006.

[141] S. M. Park, T. Ikegami, K. Ebihara, and P. K. Shin *Appl. Surf. Sci.*, vol. 253, pp. 1522–7, 2006.

[142] J. Clatot, G. Campet, A. Zeinert, C. Labrugere, M. Nistor, and A. Rougier *Solar Energy Materials and Solar Cells*, vol. 95, pp. 2357–2362, 2011.

[143] J. Skriniarova, J. Kovac, D. Hasko, A. Vincze, J. Jakabovic, L. Janos, M. Vesely, I. Novotny, and Bruncko *J. Phys.: Conf. Series*, vol. 100, p. 042031, 2008.

[144] S. Singh, R. Kumar, T. Ganguli, R. S. Srinivasa, and S. Major *Journal of Crystal Growth*, vol. 310, pp. 4640–6, 2008.

[145] T. Bekkay, E. Sacher, and A. Yelon *Surf. Science*, vol. 217, p. L377, 1989.

[146] Q.-B. Ma, Z.-Z. Ye, H.-P. He, S.-H. Hu, J.-R. Wang, L.-P. Zhu, Y.-Z. Zhang, and B.-H. Zhao *J. Cryst. Growth*, vol. 304, pp. 64–8, 2007.

[147] E. Burstein *Phys. Rev.*, vol. 93, pp. 632–3, 1954.

[148] T. S. Moss *Proc. Phys. Soc. sect. B London*, vol. 67, p. 775, 1954.

[149] G. D. Mahan *J. Appl. Phys.*, vol. 51, p. 2634, 1980.

[150] J. Serre and A. Ghazali *Phys. Rev. B*, vol. 28, pp. 4704–15, 1983.

[151] K. F. Berggren and B. E. Sernelius *Phys. Rev. B*, vol. 24, pp. 1971–86, 1981.

[152] S. C. Jain, J. M. Mcgregor, and D. J. Roulston *J. Appl. Phys.*, vol. 68, pp. 3747–9, 1990.

[153] C. M. Araujo *et al. Microelectron. J.*, vol. 33 and, p. 365, 2002.

[154] E. F. Schubert, I. D. Goepfert, W. Grieshaber, and J. M. Redwing *Appl Phys. Lett.*, vol. 71, pp. 921–3, 1997.

[155] P. W. Anderson *Phys. Rev.*, vol. 109, pp. 1492–1505, 1958.

[156] E. Abrahams, P. Anderson, D. Licciardello, and T. Ramakrishnan *Phys. Rev. Lett.*, vol. 42, pp. 673–676, 1979.

[157] F. Evers and A. D. Mirlin *Rev. Mod. Phys.*, vol. 80, p. 1355, 2008.

[158] R. Scherwitzl, S. Gariglio, M. Gabay, P. Zubko, M. Gibert, and J.-M. Triscone *Phys. Rev. Lett.*, vol. 106, p. 246403, 2011.

[159] B. Altshuler, D. Khmelnitzkii, A. Larkin, and P. Lee *Phys. Rev. B*, vol. 22, p. 5142, 1980.

[160] A. Goldenblum, V. Bogatu, T. Stoica, and A. Many *Phys. Rev. B*, vol. 60, p. 5832, 1999.

[161] A. B. Marian, M. Serbanescu, R. Manaila, E. Ivanov, O. Malis, and A. Devenyi *Thin Solid Films*, vol. 259, p. 105, 1995.

[162] A. Schmid *Z. Phys.*, vol. 259, p. 421, 1973.

[163] D. B. Haviland, Y. Liu, and A. M. Goldman *Phys. Rev. Lett.*, vol. 62, p. 2180, 1989.

[164] K. A. Parendo, K. H. Sarwa, B. Tan, A. Bhattacharya, M. Eblen-Zayas, N. Staley, and A. M. Goldman *Phys. Rev. Lett.*, vol. 94, p. 197004, 2005.

[165] A. M. Goldman *Int. J. Mod. Phys. B*, vol. 24, p. 4081, 2010.

[166] N. P. Stepina, E. S. Koptev, A. V. Dvurechenskii, and A. I. Nikiforov *Phys. Rev. B.*, vol. 80, p. 125308, 2009.

[167] S. Y. Myong, J. Steinhauser, R. Schluchter, S. Fay, E. Vallat-Sauvain, A. Shah, C. Ballif, and A. Rufenacht *Solar Energy Materials & Solar Cells*, vol. 91, p. 1269, 2007.

[168] D. H. Zhang and H. L. Ma *Appl. Phys. A*, vol. 62, pp. 487–492, 1996.

[169] A. G. Zabrodskii and K. N. Zinoveva *Sov. Phys. JETP*, vol. 59, p. 425, 1984.

[170] A. M. Gilbertson, A. K. M. Newaz, W.-J. Chang, R. Bashir, S. A. Solin, and L. F. Cohen *Appl. Phys. Lett.*, vol. 95, p. 012113, 2009.

[171] P. Dai, Y. Zhang, and M. P. Sarachik *Phys. Rev. B*, vol. 45, p. 3984, 1992.

[172] A. R. Denton and N. W. Ashcroft *Phys. Rev. A*, vol. 43, pp. 3161–3164, 1991.

[173] F. Bernardini, V. Fiorentini, and D. Vanderbilt *Phys. Rev. B*, vol. 56, p. R10024, 1997.

[174] O. Ambacher, J. Smart, J. R. Shealy, N. G. Weimann, K. Chum, M. Murphy, W. J. Schaff, L. F. Eastman, R. Dimitrov, L. Wittmer, M. Stutzmann, W. Rieger, and J. Hilsenbeck *J. Appl. Phys.*, vol. 85, p. 3222, 1999.

[175] S. Krishnamoorthy, A. A. Iliadis, A. Inumpudi, S. Choopun, R. D. Vispute, and T. Venkatesan *Solid-State Electronics*, vol. 46, p. 1633, 2002.

[176] K. Koike, I. Nakashima, K. Hashimoto, S. Sasa, M. Inoue, and M. Yano *Appl. Phys. Lett.*, vol. 87, p. 112106, 2005.

[177] A. Tsukazaki, A. Ohtomo, T. Kita, Y. Ohno, H. Ohno, and M. Kawasaki *Science*, vol. 305, p. 1388, 2007.

[178] A. Ohtomo, R. Shiroki, I. Ohkubo, H. Koinuma, and M. Kawasaki *Appl. Phys. Lett.*, vol. 75, p. 4088, 1999.

[179] L. Yang, Q. Zhao, G. Xing, D. Wang, T. Wu, M. Willander, I. Ivanov, and J. Yang *Applied Surface Science*, vol. 257, p. 8629, 2011.

[180] A. Ashrafi and Y. S. and *J. Appl. Phys.*, vol. 104, p. 123528, 2008.

[181] A. Boonchun and W. Lambrecht *J. Vac. Sci. Technol.*, vol. 27, p. 1717, 2009.

[182] Y. Ogawa and S. Fujihara *Phys. Status Solidi a*, vol. 202, p. 1825, 2005.

[183] A. K. Sharma, J. Narayan, J. F. Muth, C. W. Teng, C. Jin, A. Kvit, R. M. Kolbas, and O. W. Holland *Appl. Phys. Lett.*, vol. 75, p. 3327, 1999.

[184] A. Ohtomo, M. Kawasaki, T. Koida, K. Masubuchi, H. Koinuma, Y. Sakurai, Y. Yoshida, T. Yasuda, and Y. Segawa *Appl. Phys. Lett.*, vol. 72, p. 2466, 1998.

[185] S. Fujihara, Y. Ogawa, and A. K. and *Chem. Mater.*, vol. 16, p. 1965, 2004.

[186] M. Galassi *et al.*, "*GNU* scientific library reference manual 3rd ed., **isbn** 0954612078,"

[187] K. Huang, Z. Tang, L. Zhang, J. Yu, J. Lv, X. Liu, and F. Liu *Applied surface Science*, vol. 258, p. 3710, 2012.

[188] H.-A. Chin, I.-C. Cheng, C.-I. Huang, Y.-R. Wu, W.-S. Lu, W.-L. Lee, J. Z. Chen, K.-C. Chiu, and T.-S. Lin *J. Appl. Phys*, vol. 108, p. 054503, 2010.

[189] C.-I. Huang, H.-A. Chin, Y.-R. Wu, I.-C. Cheng, J. Z. Chen, K.-C. Chiu, and T.-S. Lin *IEEE Trans. Electron Devices*, vol. 57, p. 696, 2010.

[190] J. Singh, *Physics of Semiconductors and their Heterostructures*. McGraw-Hill, New York, 1993.

[191] B. Kramer and A. MacKinnon *Rep. Prog. Phys.*, vol. 56, p. 1470, 1993.

[192] R. Gottinger, A. Gold, G. Abstreiter, G. Weimann, and W. Schlapp *Eu-rophys. Lett.*, vol. 6, p. 183, 1988.